SUSTAINABLE ELECTRODES FOR THE NEXT GENERATION OF ENERGY STORAGE DEVICES

by

Dilara Köroğlu

B.S., Chemical Engineering, Boğaziçi University, 2015

M.S., Chemical Engineering, Boğaziçi University, 2017

Submitted to the Institute for Graduate Studies in
Science and Engineering in partial fulfillment of
the requirements for the degree of
Doctor of Philosophy

Graduate Program in Chemical Engineering

Boğaziçi University

2025

ACKNOWLEDGEMENTS

First and foremost, I'd like to thank my thesis supervisor, Assist. Prof. Betül Uralcan, for her patience, persistence, dedication and resilience throughout my studies. If I describe her with one sentence, it should be 'Impossible is Nothing'. I'm thankful to Assoc. Prof. Oktay Demircan and Assoc. Prof. Damla Eroğlu Pala for their invaluable feedback and contributions with their thought-provoking questioning.

I'm thankful to Prof. Erdem Günay and Dr. Elif Can Özcan for their valuable time and comments on my thesis. I'm very thankful to Prof. Dr. Ramazan Yıldırım for guiding me not only throughout academic life but also throughout social life for the last 10 years. I'm thankful to his valuable time and efforts on my studies.

I'm grateful to Ayşe Korkut and Duygu Kaya for sharing the last 5 years of my life. They help me not only for my academic growth but also enjoying this life. I'm thankful to all Soft Matter Laboratory members, Ayşe Hafsa Doğan, Yağız Efe Aksoy, Doğan Tarık Karabay, Hakan Sakallıoğlu, Kerem Kamitoğlu, Esin Aydemir for their kindness and friendship.

I'm thankful to all my professors at Boğaziçi University and Dilek Kırkoç, Yakup Bal and Fırat Aydın for their valuable contributions to my life.

I'm thankful to my dear husband, Yavuz Köroğlu. You have been through the most wonderful and the most difficult seasons of my life. You have been through it all, supporting, encouraging and uplifting. I feel happy to walk this journey together.

Finally, I'd like thank to my parents, two angels of my life. They are the most supportive and kindest to me no matter what during my whole life. I love you so much.

This work was supported by grants from The Scientific and Technological Research Council of Turkey (TUBITAK) under BIDEB 2232-A International Fellowship for Outstanding Researchers (Project Number T118C220) and Bogazici University Research Fund (Project Number 18982).

ABSTRACT

SUSTAINABLE ELECTRODES FOR THE NEXT GENERATION OF ENERGY STORAGE DEVICES

This dissertation explores the development and optimization of biomass-derived carbon electrodes for next-generation supercapacitors, with a focus on enhancing electrochemical performance through structural modifications and material integration. The study begins with data collection related to carbon-based supercapacitors, and the connection between descriptors (input variables) and capacitance values was established. The study includes the synthesis and characterization of activated carbon electrodes derived from biomass precursors. The porous structure, specific surface area, and electrochemical properties of these materials are systematically analyzed using techniques such as Brunauer–Emmett–Teller (BET) surface area measurements, Raman spectroscopy, X-ray photoelectron spectroscopy (XPS), and scanning electron microscopy (SEM). Electrochemical performance is evaluated through cyclic voltammetry (CV), galvanostatic charge-discharge (GCD), and electrochemical impedance spectroscopy (EIS). To further enhance performance, the dissertation investigates the incorporation of reduced graphene oxide and carbon quantum dots into biomass-derived activated carbon electrodes. The optimized composite electrodes exhibit significant improvements in capacitance retention and cycling stability.

The research also explores the integration of boron-doped reduced graphene oxide with activated carbon electrodes, giving better performance through tailored surface chemistry and improved charge transfer kinetics. Additionally, a novel carbon quantum dot-based gel electrolyte is developed to enhance ion mobility and stability, contributing to device performance. The findings of this dissertation highlight the potential of biomass-derived carbon materials as sustainable and high-performance electrode materials for supercapacitors.

ÖZET

GELECEK NESİL ENERJİ DEPOLAMA CİHAZLARI İÇİN SÜRDÜRÜLEBİLİR ELEKTROTLAR

Bu tez, biyokütle kaynaklı karbon elektrotlarının bir sonraki nesil süperkapasitörler için geliştirilmesi ve optimizasyonuna odaklanarak, yapı modifikasyonları ve malzeme entegrasyonu yoluyla elektro-kimyasal performansın artırılmasını incelemektedir. Çalışma, biyokütle öncüllerinden türetilen aktif karbon elektrotlarının sentezi ve karakterizasyonu ile başlamaktadır. Bu malzemelerin gözenekli yapısı, özgül yüzey alanı ve elektro-kimyasal özellikleri, Brunauer–Emmett–Teller (BET) yüzey alanı ölçümleri, Raman spektroskopisi, X-ışını fotoelektron spektroskopisi (XPS) ve taramalı elektron mikroskobu (SEM) gibi teknikler kullanılarak sistematik bir şekilde analiz edilmiştir. Elektro-kimyasal performans, döngüsel voltametri (CV), galvanostatik şarj-deşarj (GCD) ve elektro-kimyasal empedans spektroskopisi (EIS) yöntemleriyle değerlendirilmiştir. Performansı daha da artırmak amacıyla, tez, biyokütle kaynaklı aktif karbon elektrotlarına indirgenmiş grafen oksit ve karbon kuantum noktalarının entegrasyonunu incelemektedir. Optimizasyon sonucu elde edilen kompozit elektrotlar, kapasite tutma ve çevrim kararlılığında önemli iyileşmeler sergilemektedir.

Araştırma ayrıca, borlu doplanmış indirgenmiş grafen oksit ile aktif karbon elektrotlarının entegrasyonunu inceleyerek, özelleştirilmiş yüzey kimyası ve geliştirilmiş yük transfer kinetikleri sayesinde enerji depolama performansının arttığını göstermektedir. Ayrıca, iyon hareketliliğini ve elektrolit stabilitesini artırmak amacıyla, cihaz performansını daha da iyileştiren yeni bir karbon kuantum nokta bazlı jel elektrolit geliştirilmiştir. Bu tezin bulguları, biyokütle kaynaklı karbon malzemelerinin süperkapasitörler için sürdürülebilir ve yüksek performanslı elektrot malzemeleri olarak potansiyelini vurgulamaktadır.

TABLE OF CONTENTS

ACKNOWLEDGEMENTS iii
ABSTRACT v
ÖZET vi
LIST OF FIGURES ix
LIST OF TABLES xiv
LIST OF SYMBOLS xv
LIST OF ACRONYMS/ABBREVIATIONS xvi
1. INTRODUCTION 1
2. LITERATURE SURVEY 6
2.1. Working Principles of Supercapacitors 6
2.2. Components of EDLC Supercapacitors 10
2.2.1. Carbon Based Electrode Materials 10
2.2.2. Biowaste Derived Activated Carbon as Electrode Material . . . 13
2.2.3. Electrolyte Types 15
2.2.4. Current Collectors and Separator 17
2.3. Testing and Performance Evaluation of Supercapacitors 19
2.3.1. Cyclic Voltammetry 20
2.3.2. Galvanostatic Charge-Discharge 22
3. MATERIALS AND METHODS 24
3.1. Materials and Equipments 24
3.2. Activated Carbon Preparation Route 25
3.3. CQD Preparation 26
3.4. Preparation of Gel Electrolyte 27
3.5. Preparation of 3-Electrode Systems 27
3.6. Preparation of 2-Electrode Systems 28
3.7. Structural Characterizations 29
3.8. Electrochemical Characterizations 30
4. DESCRIPTIVE STATISTICAL ANALYSIS OF SUPERCAPACITORS WITH

EXPERIMENTAL VALIDATION 31
4.1. Descriptive Statistical Analysis of Supercapacitors 31
4.2. Experimental Validation 39
5. FLEXIBLE SOLID-STATE SUPERCAPACITORS BASED ON BIOWASTE-DERİVED ACTIVATED CARBON AND NANOMATERIALS FOR BETTER PERFORMANCE 44
5.1. Structural Characterization of Active Electrode Materials 44
5.1.1. Cabbage-derived Activated Carbon 44
5.1.2. Reduced Graphene Oxide 46
5.1.3. Carbon Quantum Dots 47
5.1.4. Composite Materials 48
5.1.5. The Gel Electrolytes 50
5.2. Electrochemical Characterization 52
6. ENHANCED FLEXIBLE SUPERCAPACITORS WITH B-DOPED RGO ELECTRODES AND CARBON QUANTUM DOT GEL ELECTROLYTES . . . 61
6.1. Structural Characterization of Active Electrode and Electrolyte Materials 62
6.1.1. Cabbage-derived Activated Carbon/Boron Doped Reduced Graphene Oxide 62
6.1.2. The Gel Electrolytes 67
6.2. Electrochemical Characterization 68
6.2.1. Performance of Cabbage-derived Activated Carbon/BRGO Composites 68
6.2.2. Performance of Symmetric Supercapacitors with CQD-incorporated Gel Electrolyte 71
7. CONCLUSION AND RECOMMENDATIONS 75
REFERENCES 78
APPENDIX A: Additional Structural Characterizations 106

LIST OF FIGURES

Figure 2.1. Structure of conventional capacitor vs. supercapacitor. a) Capacitor and b) Supercapacitor. 6

Figure 2.2. Models of EDLCs. a) Helmholtz, b) Gouy Chapman and c) Stern. 8

Figure 2.3. Electrode properties and supercapacitor. 11

Figure 2.4. Electrolyte properties and supercapacitor. 16

Figure 2.5. Fabrication of supercapacitors. a) 3-electrode set-up (half-cell) and b) 2-electrode set-up (device). 19

Figure 2.6. Illustrative current-potential properties of a) EDLC and b) Pseudocapacitor. 22

Figure 2.7. Illustrative potential-time properties of a) EDLC and b) Pseudocapacitor. 23

Figure 3.1. Activated carbon preparation route. 25

Figure 3.2. Schematic illustration for the preparation of CQD by bottom-up approach. 26

Figure 4.1. Performance of a. Electrode materials, b. Electrode material preparation methods and c. Electrolyte types. 32

Figure 4.2. Distribution of a. Current collector , b. Binder and c. Separator in literature. 34

Figure 4.3. Capacitance as a function of numerical input variables. 35

Figure 4.4. Comparison of real capacitance and predicted capacitance values from the ANN model. 39

Figure 4.5. AC a. N_2 ads/des isotherms, b. Pore size distribution, c. Raman spectra, fitting curves. Red line represents the Lorentzian fit to the D-peak and Blue line represents the BWF fit to the G-peak, d. The total XPS spectra, e. The XPS Deconvolution of C1s spectra and f. The XPS Deconvolution of O1s spectra. 40

Figure 4.6. a. AC CV of different scans with 1.5 M $[EMIM^+][BF_4^-]$, b. AC CV of different scans with 2.5 M $[EMIM^+][BF_4^-]$, c. Commercial AC CV of different scans with 1.5 M $[EMIM^+][BF_4^-]$ d. Commercial AC CV of different scans with 2.5 M $[EMIM^+][BF_4^-]$, Capacitance vs. scan rate e. for AC and f. for commercial AC. 41

Figure 4.7. a. Comparison of experimental capacitance and predicted capacitance obtained from the ANN model and b.Effect of electrolyte concentration and normalized scan rate on capacitance (F/g). . . 43

Figure 5.1. RGO a. N_2 ads/des isotherms, b. Pore size distribution, c. Raman spectra, fitting curves. Red line represents the Lorentzian fit to the D-peak and Blue line represents the BWF fit to the G-peak, d. The total XPS spectra, e. The XPS Deconvolution of C1s spectra and f. The XPS Deconvolution of O1s spectra. 47

Figure 5.2. CQD a. The total XPS spectra, b. The XPS Deconvolution of C1s spectra, c. The XPS Deconvolution of O1s spectra, d. The XPS Deconvolution of N1s spectra, e. UV-Vis spectroscopy, f. FTIR spectrum, g. Fluorescence excitation and emission spectra and h. Photos of CQD solution taken under daylight and UV light. 49

Figure 5.3. Structural characterizations of composite materials a. XRD spectrum, b.Raman spectra, fitting curves. Red line represents the Lorentzian fit to the D-peak and Blue line represents the BWF fit to the G-peak and c. FTIR spectrum. 51

Figure 5.4. Electrochemical characterizations of AC, AC-5CQD and AC-10CQD in 2-electrode set-up a. Cyclic voltammogram at 50 mV/s, b. Capacitance vs. scan rate, c. Capacitance retention at 150 mV/s over 1000 cycles under 0°. 53

Figure 5.5. Electrochemical characterizations of AC, AC-15RGO and AC-20RGO a. CV at 50 mV/s, b. Capacitance vs. scan rate, c. Capacitance retention over 1000 cycles of AC-15RGO under different bending angles and d. Capacitance retention over 1000 cycles of AC-20RGO under different bending angles. 55

Figure 5.6. Electrochemical characterizations of AC-15RGO-10CQD a. CV at different scan rates, b. Capacitance vs. scan rate, c. Capacitance retention over 1000 cycles, d. Maximum attainable capacitance during bending, e. GCD at different current densities and f. Capacitance retention at over 1000 cycles. 59

Figure 6.1. Pore structure analysis of AC and AC-10BRGO a. N_2 ads/des isotherms of AC, b. N_2 adsorption/desorption isotherms of AC-10BRGO, c. Pore size distribution of AC, and d. Pore size distribution of AC-10BRGO. 62

Figure 6.2. a.Raman spectroscopy of AC-10BRGO. Red line represents the Lorentzian fit to the D-peak and blue line represents the BWF fit to the G-peak, b.The total XPS spectra, c. Deconvoluted C1s XPS Spectra, d. Deconvoluted O1s XPS Spectra , e. Deconvoluted B1s XPS Spectra, and f. FTIR analysis. 65

Figure 6.3. Structural characterizations of solo gel-electrolytes a. TGA curves, b. FTIR spectrum and c. XRD spectrum. 67

Figure 6.4. Electrochemical characterizations of AC and AC-BRGOs a. CV of AC, b. CV of AC-5BRGO, c. CV of AC-10BRGO, d. CV of AC-15BRGO, e. Capacitance vs. scan rate and f. Energy densities of the electrode materials at 50 mV/s at 1.4 V potential window. . 70

Figure 6.5. Electrochemical characterizations of 0.5 wt.%, 1 wt.%, 1.5 wt.% CQD a. CV of 0.5CQD, b. GCD of 0.5CQD, c. CV of 1CQD, d. GCD of 1CQD, e. CV of 1.5CQD, f. GCD of 1.5CQD, g. Areal capacitance vs. scan rate, h. Capacitance vs. current density, i. Energy densities and j. Comparison of energy densities. 74

Figure A.1. Cross-section SEM image of PVA based gel film. 106

Figure A.2. Commercial AC structural characterizations a. Pore size distribution, b. Raman spectra, fitting curves. Red line represents the Lorentzian fit to the D-peak and Blue line represents the BWF fit to the G-peak, c. The XPS Deconvolution of C1s spectra and d. The XPS Deconvolution of O1s spectra. 106

Figure A.3. XRD spectrum of RGO. 107

Figure A.4. Structural characterization of composite materials. N_2 adsorption/desorption isotherms of a. AC-10CQD, b. AC-10CQD-15RGO, and c. Pore size distribution of the materials. 107

Figure A.5. Comparison with literature a. Ragone plots and b.Capacitance. . . 108

Figure A.6. Raman spectrum of BRGO. 108

Figure A.7. XRD spectrum of AC and AC-10BRGO. 108

Figure A.8. SEM images of a. AC and b. AC-10BRGO. 109

Figure A.9. Impedance spectroscopy of AC-10BRGO and AC-10BRGO/1CQD. 110

LIST OF TABLES

Table 2.1. Comparison of electrochemical storage devices 7

Table 2.2. CQDs incorporation to electrode and electrolyte materials in literature. 12

Table 2.3. Biomass based carbon materials and their performance. 14

Table 2.4. Supercapacitors using PVA-KOH based gel electrolyte. 17

Table 3.1. Materials used for the experimental studies. 24

Table 3.2. Equipments used for the experimental studies. 24

Table 3.3. Chemical reactions during chemical activation. 26

Table A.1. A comparison of carbon-based solid state supercapacitors. 109

Table A.2. A comparison of solid state supercapacitors with PVA-based electrolytes. 110

LIST OF SYMBOLS

ϵ	Permittivity of dielectric material
ϵ_0	Permittivity of empty space

LIST OF ACRONYMS/ABBREVIATIONS

A	Area of electrode
AC	Activated carbon
C	Capacitance
CNTs	Carbon nanotubes
CV	Cyclic voltammetry
d	Distance between electrodes
E	Potential
EDLCs	Electrical double layer capacitors
EIS	Electrochemical impedance spectroscopy
ESR	Equivalent series resistance
F	Faraday constant
GCD	Galvanostatic charge discharge
HCs	Hybrid Capacitors
MWCNTs	Multi walled carbon nanotubes
n	Number of electrons
PCs	Pseudocapacitors
Q	Electric charge
R	Ideal gas constant
T	Temperature
V	Potential difference
X	Fractional coverage of surface structure

1. INTRODUCTION

Due to growing population, there is increasing environmental pollution, global warming and diminishing supply of fossil fuels [1–5]. By the middle of the century, our world's energy needs are predicted to double, and by the year 2100, they are expected to quadruple [6, 7]. In today's society, the majority of energy usage depend on non-renewable energy sources. Therefore, recently, demand for renewable, sustainable, green and costless energy production and storage systems is accelerating. Renewable energy production from sun, wind and geothermal heat have been promoted [6, 8]. Intermittency of those renewable energies have led to the development of energy storage systems such as batteries, fuel cells and supercapacitors [9, 10]. Energy storage devices are technologies designed to capture and store energy for later use. They play a critical role in modern energy systems by enabling the efficient management of energy generation and consumption. These devices allow excess energy to be stored when it's available, such as during periods of low demand or when renewable sources like solar and wind produce surplus power. Then, this stored energy can be released when production from renewable sources drops. Energy storage devices come in various forms, each with unique properties that make them suitable for different applications. Lithium-ion batteries, known for their high energy density and efficiency, are commonly used in portable electronics and electric vehicles, but they come at a higher cost and have safety concerns related to overheating. Lead-acid batteries, while cheaper and reliable for backup power, offer lower energy density and shorter cycle life. Pumped hydro storage is a large-scale solution that provides high power density and long cycle life but requires significant infrastructure and has environmental concerns. Flow batteries offer excellent scalability, high cycle life, and lower environmental impact, making them ideal for large-scale grid storage, though they have moderate efficiency. Compressed air energy storage (CAES) is another large-scale solution that can store energy over long durations, but it's limited by geographic factors and has lower efficiency. Each device varies in terms of energy density, power density, cycle life, efficiency, cost, safety, and environmental impact, making them suitable for specific uses depending

on the need for fast response, large-scale storage, or long-term energy backup. While lithium ion batteries (LIBs) can attain high energy densities, they typically have a fairly sluggish power delivery and poor cycling stability [11]. Since supercapacitors, also known as electrochemical capacitors or ultracapacitors, have high power density, long cycle life, rapid charging and low maintenance, they have received attention from both scientists and engineers [12–14]. The Leyden jar as an early capacitor, created by Pieter von Musschenboek at the University of Leyden in Holland in the year of 1740, was consisting of a flat piece of glass coated by silver foil [15]. In 1900s, charge storage mechanisms were proposed for supercapacitors by Helmholtz, Gouy and Chapman, and Stern [16]. General Electric demonstrated and patented supercapacitors in 1957 for the first time [17]. The standard supercapacitor design utilized today was invented by Robert A. Rightmire, a scientist at the Standard Oil Company of Ohio (SOHIO) [18]. The supercapacitor developed in 1982 for military applications by the Pinnacle Research Institute (PRI) was named as PRI ultracapacitor [19]. In the year of 1990s, asymmetric and hybrid supercapacitors were developed [20]. In 2004, China developed world's first supercapacitor bus and fast charging station [21]. Since the early 2000s, there has been a significant rise in research on supercapacitors and they have been widely used in consumer electronics, industrial power, energy management, public transportation, and military services.

A supercapacitor is different from a regular capacitor in the sense that supercapacitors have higher capacitance and energy density; in other words, supercapacitors store more charges. A capacitor stores energy in an electrical field while supercapacitors store energy in chemical form. A capacitor consists of two parallel plates separated by an insulating material (dielectric). In a supercapacitor, there is an electrolytic solution (rather than dielectric) between two electrodes [19, 22, 23].

Supercapacitors can be divided into three categories based on charge storage mechanism; electrical double layer capacitors (EDLCs), pseudo-capacitors (PCs) and hybrid capacitors (HCs) [24]. In EDLCs, charge accumulate at the surface of electrode and electrolyte interface. EDLCs include two carbon based electrode materials

separated by an ion-permeable separator, which is used to prevent short circuits [25]. In PCs, charge storage is based on fast and reversible faradaic redox reactions using conductive polymers, transition metal oxides, chalcogenides and metal nitrides as electrodes [26]. PCs have higher energy densities as compared to EDLCs; however, PCs have restricted lifetime and power density due to the the fact that electrode materials undergo faradaic redox reactions [27, 28]. The storage mechanism of a hybrid supercapacitor is based on the combination of pseudo and double-layer capacitance.

The emergence of wearable electronics as well as demand for small, light-weight and space-efficient packaging has spurred the development of flexible solid state supercapacitors [29–32]. Stretchability is an indispensable property for wearable electronics [33]. Material design and device architecture are critical for fabrication of flexible supercapacitor devices [34]. Flexible solid-state supercapacitors are made generally of flexible electrodes, solid-state electrolyte (gel polymer electrolyte), a separator and a flexible packaging material [12]. Flexible solid state supercapacitors are different than conventional ones in the sense that electrode materials are required to possess certain flexibility and electrolyte materials ought to be solid state [35]. Most of the electrode structure is rigid, in other words, it is not malleable; as a result, electrode is easily deformed. Therefore, the studies have been geared towards the functionalization of electrode materials, modification in properties of electrode and electrolyte compounds [36].

Overall performance of supercapacitor depends on reasonable selection of electrodes, electrolyte materials and separators [37, 38]. Electrode materials are predominant compounds in supercapacitor devices. The best performing electrode materials have high electrical conductivity, high electrochemical surface area, hierarchical porous structure, good surface wettability, durability and low-cost [39]. Electrolyte materials are also crucial for a better performed supercapacitor. The system voltage depends on the stability of the electrolyte, the energy density is limited by the breakdown voltage of the electrolyte, and the power density relies on electrolyte conductivity [40, 41].

Separators ought to possess high physical strength, ion permeability and durability in addition to reasonably good performing electrode and electrolyte materials [42].

Two-electrode (device) or three-electrode (half-cell) set-ups can be used to assess the electrochemical performance of supercapacitors [43]. A three-electrode setup is frequently used for active material measurement in order to determine the optimal operating parameters for supercapacitors. Three- electrode system consists of a chosen electrolyte, a counter electrode and reference electrode, and the working electrode, which is often the synthesized electrode material [44]. The counter electrode produces a particular amount of current at the working electrode by altering the potential of the electrolyte [45]. On the other hand, the reference electrode functions as a reference point for measurements and potential control without permitting current to pass through it [46]. If satisfying results are obtained from three-electrode set-up, one can continue with the two-electrode (device) system. Two-electrode system can be symmetric (two same electrode materials) or asymmetric (two distinct electrode materials). Two-electrode system is made up of an anode and a cathode separated by a separator [47]. Additionally, spacer and spring can be used to tighten the materials in the supercapacitor case.

The electrochemical performances of supercapacitors can be evaluated via several methods, three of most commonly used ones are cyclic voltammetry (CV), galvanostatic charge discharge (GCD) and electrochemical impedance spectroscopy (EIS). CV is a widely-used electrochemical technique. CV yields basic information about a capacitive electrochemical cell including capacitance [48]. GCD is another common method to determine the performance of the device over time. EIS is a powerful tool to investigate properties of materials and electrode reactions [49].

In Chapter 2, a literature survey regarding supercapacitors, their working principles, components and testing techniques are given. In Chapter 3, materials and equipment used during experimental studies are given. Chapter 4 includes descriptive statistical analysis of supercapacitor literature with experimental validation.

Chapter 5 explores the performance of hybrid electrode material (AC-RGO-CQD) in the application of flexibles supercapacitors. Chapter 6 includes the effect of boron in activated carbon structure along with CQD incorporation into gel electrolyte for flexible supercapacitors. The main conclusions and recommendations are given in Chapter 7.

2. LITERATURE SURVEY

2.1. Working Principles of Supercapacitors

Supercapacitors and conventional capacitors operate on very similar principles. A typical capacitor consists of two electrodes, which are metallic plates, and a dielectric material in between them. One of the two electrodes experiences an accumulation of charges upon application of a potential [50, 51]. Instead of a dielectric material, the wedging substance in a supercapacitor is an electrolytic solution as shown in Figure 2.1. A capacitor linked in a circuit will function as a voltage source when two plates are

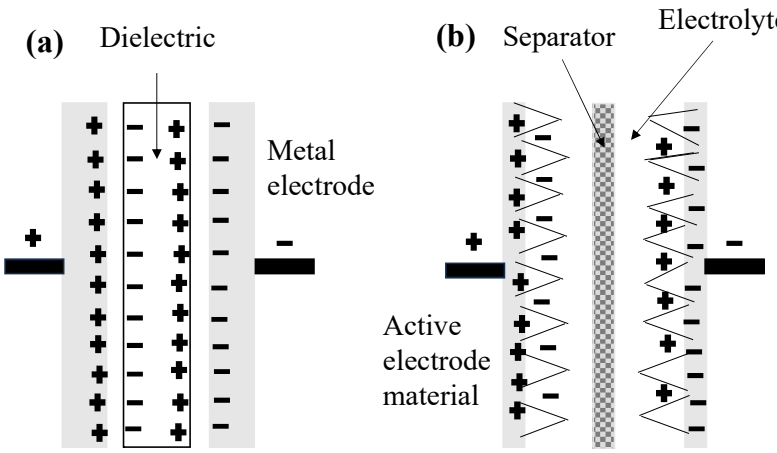

Figure 2.1. Structure of conventional capacitor vs. supercapacitor. a) Capacitor and b) Supercapacitor.

charged, and current will flow through it until total charge balance is reached. Hence, capacitance can be calculated as the ratio between electric charge (Q) and potential difference (V) [45] as in

$$C = \frac{Q}{V}. \tag{2.1}$$

Capacitance (C) for a conventional capacitor (Figure 2.1 (a)) is inversely related to the distance between the electrodes (d) and proportionate to the area of each electrode (A) and the permittivity of empty space (vacuum) (ϵ_0) [52] and it can be calculated as in

$$C = \epsilon_0 \frac{A}{d}. \tag{2.2}$$

If dielectric material is filled between two electrodes, Equation 2.2 should be replaced [53] by

$$C = \epsilon\epsilon_0 \frac{A}{d}, \tag{2.3}$$

where ϵ represents permittivity of dielectric material and it takes the value of 1, 2 and 3 for air, polypropylene and polyester, respectively [54].

Some of the features such as specific energy, discharge time and coulombic efficiency of electrochemical storage devices are compared in Table 2.1 and it shows that supercapacitors provide hundred to many thousand times higher power; however, they are not able to store the same amount of charge as compared to batteries. How to improve the energy density is still the research question and difficulty in the field of supercapacitors [55].

Table 2.1. Comparison of electrochemical storage devices [1].

Characteristics	**Capacitor**	**Supercapacitor**	**Battery**
Specific energy ($Whkg^{-1}$)	<0.1	1-10	10-100
Specific power (Wkg^{-1})	>10000	500-10000	<1000
Discharge time	10^{-6} to 10^{-3}	s to min	0.3-3 h
Charge time	10^{-6} to 10^{-3}	s to min	1-5 h
Coulombic efficiency (%)	About 100	85-98	70-85
Charge time	Almost infinite	>500000	About 1000

Based on charge storage mechanism, supercapacitors are divided into three groups, which are EDLCs, PCs and HCs. The original model for EDLCs was firstly proposed by Helmholtz in 1850s [17]. It states that positive and negative charge layers are oriented along the boundaries between the electrodes and the electrolytic solution when a voltage is applied to the device, causing both electrodes to produce electric double layers (Figure 2.1 (b)) [56]. Electrical charges are stored in these electric double layers. There are two layers of charge: one is found in the surface lattice structure of the electrode, and the other is caused by solvated and dissolved ions with opposing polarity in the electrolytic solution (Figure 2.2 (a)) [45, 52]. This concept by Helmholtz was revolutionary; however, there was inadequacy for ion diffusion and the relation between electrolyte's dipole moment and the active electrode material [57]. Afterwards, Gouy and Chapman postulated that ionic accumulation at the active material surface was the cause of a diffuse layer that exists within the electrolyte (Figure 2.2 (b)). Further, by taking into consideration the hydrodynamic mobility of the ionic species in the diffuse layer and the ion build-up near the electrode surface, the Stern model combined the ideas of the Helmholtz and Gouy Chapman models [58]. In Stern model (Figure 2.2 (c)), there are two regions: Stern layer (inner region) and the diffuse layer (outside region). The electrode strongly adsorbs ions, which are frequently hydrated, in the Stern layer. The area around an electrode where electrolyte ions are continuously distributed due to thermal mobility in the electrolyte solution is known as the diffuse layer [58].

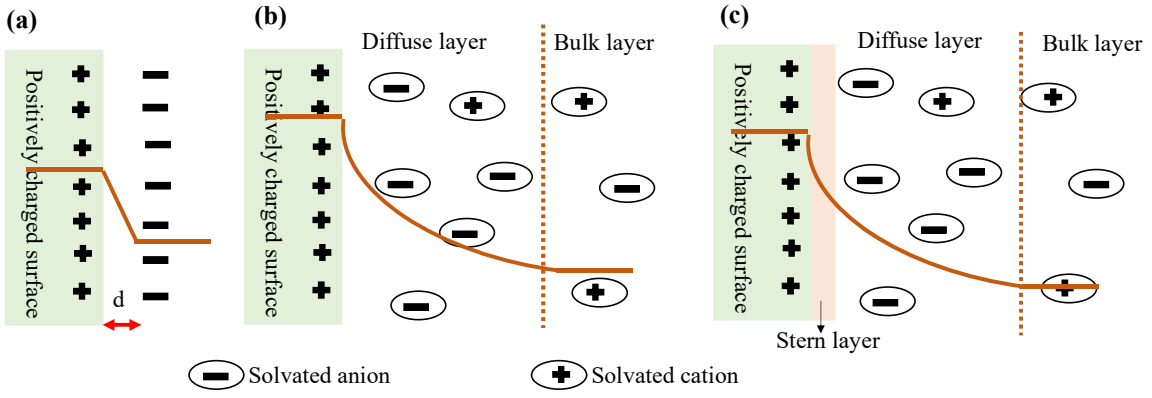

Figure 2.2. Models of EDLCs. a) Helmholtz, b) Gouy Chapman and c) Stern.

The two layers are in agreement with two series capacitors with capacitances C_H and C_D that are Helmholtz layer (Stern layer) and diffuse layer capacitances, respectively [23]. C_{Eq} is the capacitance of the electrode as can be evaluated as

$$C_{Eq} = \frac{1}{C_H} + \frac{1}{C_D}. \tag{2.4}$$

The electrolyte ions, the solvent that dissolves them and the chemical affinity that exists between the surface of the active material and the adsorbed ions, all have an impact on the performance in EDLCs.

PCs possess a Faradaic way of charge storage in electroactive materials by means of reversible redox processes [59]. Electrodes are generally doped with transition metal oxides, such as oxides of Mn, Ni, Co, Ru, and Fe, or covered in conductive polymers in order to fabricate PCs. The fast Faradaic process involves the transmission of charges through the double layer [60]. Equation 2.5 illustrates how interfacial adsorption/desorption processes relate to potential and charge extent [45]. In equation 2.5, E denotes the potential, E_0 denotes the standard potential, R denotes the ideal gas constant, T denotes the temperature, n denotes the number of electrons, F denotes the Faraday constant and X denotes the fractional coverage of the surface or inner structure as in

$$E = E_0 - \frac{RT}{nF} Ln(\frac{X}{1-X}). \tag{2.5}$$

Capacitance can be calculated as in

$$C = (\frac{nF}{M})\frac{X}{E}, \tag{2.6}$$

where M is the weight of the electrode material.

Although higher capacitance and higher energy density can be obtained via PCs as compared to EDLCs, PCs have poor cycling stability. A hybrid supercapacitor combines the double-layer capacitance and the pseudocapacitance to store electrical energy. One electrode is composed of a material with pseudocapacitive properties,

while the other has charge separation as a result of the creation of a double layer. By carefully designing a hybrid system, these supercapacitors address the particular problems associated with either supercapacitors or batteries [61].

2.2. Components of EDLC Supercapacitors

An EDLC supercapacitor device is composed of a negative and a positive electrode, an electrolyte, current collectors and a separator.

2.2.1. Carbon Based Electrode Materials

Carbon-based materials are considered as the most promising candidates as electrode materials for the commercialization of supercapacitors, particularly EDLCs. EDLCs have made use of graphene, carbon nanotubes (CNTs) and activated carbon (AC) thanks to their affordability, high chemical stability, good electrical conductivity, light weight, and broad operating temperature range [62]. Since carbon based materials store charges through physical adsorption and desorption, specific surface area, pore size and structure, and electrical conductivity are important factors to evaluate the performance of carbon based materials. As can be seen from Figure 2.3, the performance of supercapacitors are considerably affected by those properties mentioned above.

Graphene can be found in the form of graphite in nature. Single layer graphene was obtained by Andre and Konstantin in 2004 for the first time [17]. Graphene is the most thermally conductive carbon material and it has excellent optical properties as well as high chemical stability and surface area, which makes it an ideal candidate for the applications of supercapacitors. The main techniques for preparation of graphene include mechanical exfoliation, chemical vapor deposition (CVD) and chemical derivation [63].

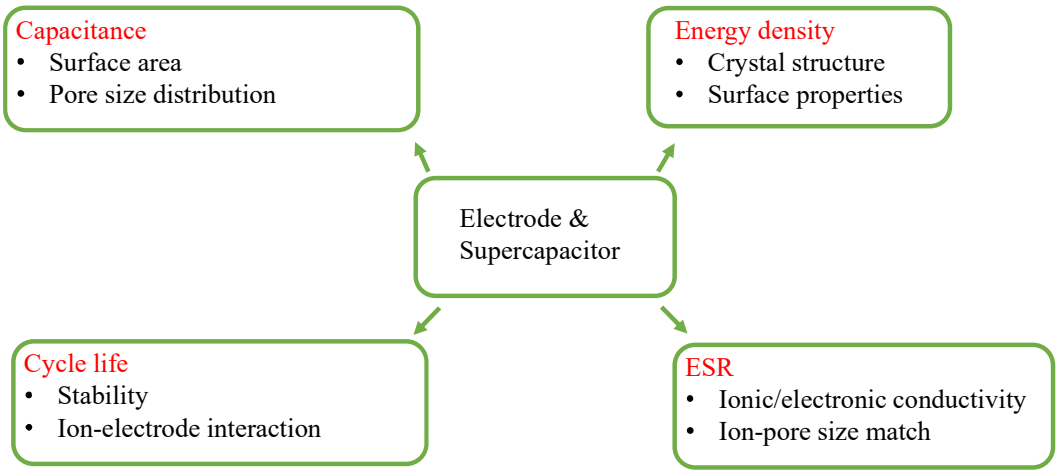

Figure 2.3. Electrode properties and supercapacitor.

CNTs, multi-walled CNTs (MWCNTs), was discovered in the year of 1991 by Iijima for the first time [64]. CNTs possess high surface area, high conductivity, low resistance, excellent tensile strength and good chemical stability [65]. CNTs are mostly prepared by the methods of arc discharge, laser ablation and chemical vapor deposition (CVD) [66]. Among those methods, CVD is the common one due to the fact that it offers easy control of the reaction process, low reaction temperature and high yield.

Activated carbon is the most widely used carbon material and it entered the commercial area in the vicinity of 1900 by von Ostreijko who got two patents [67]. AC's high porosity, large specific surface area, high conductivity, and low cost make it an excellent electrode material for supercapacitors. AC preparation methods can be classified into two steps as carbonization and activation. Since the scope of this thesis includes biowaste derived AC preparation and application, the details of preparation methods and studies in literature will be given in 2.2.2.

Further, carbon quantum dots (CQDs) are a new class of carbon materials and recent research has been focused on CQDs due to having ultra-small sizes (lower than 10 nm), uniform dispersion, excellent charge transfer/reservoir properties, abundant surface functional groups and photoluminescent properties [68]. CQDs are incorporated into various active electrode materials and electrolyte as given in Table 2.2. High

Table 2.2. CQDs incorporation to electrode and electrolyte materials in literature.

Electrode	**Electrolyte**	**Performance**	**Ref**
Activated carbon/CQD	6 M KOH	100-134 F/g	[69]
N,P-RGO/CQD	6 M KOH	217-453 F/g	[70]
MnO_2/CQD	1 M Na_2SO_4	230-340 F/g	[71]
Bi_2O_3/CQD	1 M $LiPF_6$ and 3 M KOH	343 F/g	[72]
GNP	CQD-Gel	140 F/g	[62]

gravimetric capacitances are achieved with CQD incorporation to activated carbon and reduced graphene oxide ([69, 70]). Besides, CQD addition to pseudocapacitive materials such as MnO_2 and Bi_2O_3 improved capacitances to a great extent [71, 72].

Apart from common EDLC elecrode materials, carbide derived carbon (CDC) and carbon nanospheres are gaining significance in energy storage applications. CDC is a unique material created by selectively removing non-carbon elements from metal carbides, typically through a high-temperature chlorination process [73]. This results in a highly porous, structured form of carbon with exceptional surface area and tunable properties, making it an ideal candidate for applications in energy storage [74]. Its remarkable versatility and tailored pore structure have made CDC a subject of growing interest in advanced materials research.

On the other hand, carbon nanospheres are spherical particles composed of pure carbon, typically ranging from a few nanometers to several micrometers in size. These nanostructures exhibit unique properties such as high surface area, electrical conductivity, and excellent chemical stability [75]. Due to their small size, uniform shape, and tunable surface characteristics, carbon nanospheres have found promising applications in areas like energy storage, sensors, and electronics, making them a key material in nanotechnology research [76].

2.2.2. Biowaste Derived Activated Carbon as Electrode Material

The renewable biowaste derived activated carbons are of special interest among carbon based materials since they offer higher specific surface areas, superior chemical stability, and favorable environmental compatibility at comparatively lower costs. AC can be prepared mainly by two steps: carbonization and activation. The carbon rich organic precursor must first be carbonized into char in an inert atmosphere [77]. One of the most important stages that influences the performance of AC as an electrode material is the activation process.

There are several methods to create porous conductive carbon, each with distinct processes and advantages. Physical activation involves heating carbon materials in a gas atmosphere (such as CO^2 or H_2O) at high temperatures, which leads to the breakdown of bonds and formation of a porous structure. Chemical activation, on the other hand, uses chemical agents like phosphoric acid or potassium hydroxide to enhance porosity at lower temperatures [78]. The sol-gel method is another approach where organic precursors are converted into gels, which are then carbonized to form porous structures. Template-based methods use a porous material mold to shape the carbon, which is later removed to leave behind a structured, porous carbon [78, 79]. Pyrolysis involves heating organic materials (like biomass or polymers) in an oxygen-free environment, causing them to carbonize while forming porosity. 3D printing technology offers a more customized approach, building porous carbon materials layer by layer, while nanotechnology techniques, such as incorporating carbon nanotubes or graphene, enhance conductivity and surface area at the nano scale [80]. Additionally, electrical or chemical polymerization can be used to modify the carbon structure and improve its properties. Each method offers different benefits depending on the intended application, with trade-offs in cost, complexity, and material properties. Owing to their affordability, renewable nature, and environmental friendliness, various types of biomass have been used to create useful carbon based electrode materials and Table 2.3 summarizes some of the biomasses and their utilization in supercapacitors. 2E denotes for 2-electrode whereas 3E denotes for 3-electrode.

Table 2.3. Biomass based carbon materials and their performance.

Biomass	**Electrolyte**	**Capacitance, F/g**	**Ref**
Onion husk	1M $TEABF_4$	188 (3E)	[81]
Palm kernel shell	1M KOH	210 (3E)	[82]
Watermelon rind	6M KOH	333 (3E)	[83]
Peanut shell	1M H_2SO_4	340 (3E)	[84]
Rose flower	6M KOH	460 (3E)	[85]
Jujube fruit	6M KOH	350 (3E)	[86]
Tea waste buds	6M KOH	332 (3E)	[87]
Water bamboo	6M KOH	268 (3E)	[88]
Fir wood	0.5M H_2SO_4	142 (3E)	[89]
Banana fibers	1M Na_2SO_4	74 (3E)	[90]
Corn grain	6M KOH	257 (3E)	[91]
Coffee beans	1M H_2SO_4	368 (2E)	[92]
Coffee shells	6M KOH	156(2E)	[93]
Waste paper	6M KOH	180 (2E)	[94]
Cherry stones	2M H_2SO_4	230 (2E)	[95]
Potato starch	6M KOH	335 (2E)	[96]
Cassava peel	0.5M H_2SO_4	153 (2E)	[97]
Rubber wood sawdust	1M H_2SO_4	33.7 (3E)	[98]
Wheat straw	1M $MeEt_3NBF_4$	251 (2E)	[99]
Sun flower seed shell	30 wt. % KOH	311 (3E)	[100]
Auricularia	6M KOH	347 (3E)	[101]
Egg shell membrane	1M KOH	203 (3E)	[102]
Celtuce leaves	2M KOH	421 (3E)	[103]
Coconut shell	6M KOH	268 (3E)	[104]
Cotton stalk	1M Et_4NBF_4	114 (2E)	[105]
Ginkgo shell	6M KOH	178 (3E)	[106]
Hemp	BMPYTFSI	122 (2E)	[107]
Wallnut shell	6M KOH	117 (2E)	[108]
Tea leaves	2M KOH	330 (3E)	[109]
Pomelo peel	6M KOH	342(3E)	[110]
Human hair	6M KOH	340 (3E)	[111]
Sago bark	5M KOH	180 (2E)	[112]
Paulownia flower	1M H_2SO_4	297 (2E)	[113]
Soybean	6M KOH	425 (3E)	[114]
Willow catkins	6M KOH	340 (3E)	[115]
Shiitake-mushroom	6M KOH	306 (3E)	[116]
Fallen leaves	6M KOH	268 (3E)	[117]
Albumen	1M H_2SO_4	255 (3E)	[118]
Corncob	6M KOH	314 (3E)	[119]
Rice husk	6M KOH	245 (2E)	[120]
Stiff silkworm	6M KOH	304 (3E)	[121]
Stiff silkworm	6M KOH	304 (3E)	[121]
Mustard oil	H_2SO_4-PVA	115 (2E)	[122]
Coca Cola	6M KOH	352 (3E)	[123]

Soybean reported by Wang and others ([115]) and celtuce leaves reported by Long and others ([114]) gave high gravimetric capacitances as they offer high surface area and hierarchical pore size distribution for supercapacitors. Boyjoo et al. studied on Coca-Cola as carbon source for the active electrode material and they revealed a high gravimetric capacitance in 3-electrode set-up [123]. Following these works (many are mentioned in Table 2.3), the biomass based activated carbon usage in the applications of supercapacitors have been attracted increasing attention with some significant progress that was made in recent years.

2.2.3. Electrolyte Types

The electrolyte, which is one of the key components of supercapacitor, consists of electrolyte salt and solvent. Electrolyte offers ionic conductivity, which makes charge adjustment easier on the electrodes [124]. In general, different types of electrolytes have been developed to date. Electrolytes have an impact on capacitance and it is vital to choose an electrolyte with suitable ion sizes so that there will be a good match between ion size of the electrolyte and pore size of the electrode. The potential window of the electrolyte is critical for achieving higher energy density. Moreover, the selection of electrolyte has a major impact on equivalent series resistance (ESR) [125]. Electrolytes with strong ionic conductivity will have lower ESR and higher power densities [124]. Overall, electrolytes should possess low viscosity, high ionic conductivity, wider potential window, high chemical stability, low-cost and they should be environmentally friendly (Figure 2.4).

Electrolytes can be classified as liquid (aqueous, organic, ionic liquids (ILs)) and solid-state electrolytes [126]. Aqueous electrolytes can be grouped into alkaline, acid and neutral solutions, the most commonly used ones are Na_2SO_4, H_2SO_4 and KOH, respectively. High capacitance and conductivity can be achieved by aqueous electrolytes; nevertheless, they have a limited operating voltage due to their restricted decomposition voltage. On the other hand, organic electrolytes dominate commercial market due to their large operating electric potential window (in the region of 2.5-2.8 V). The

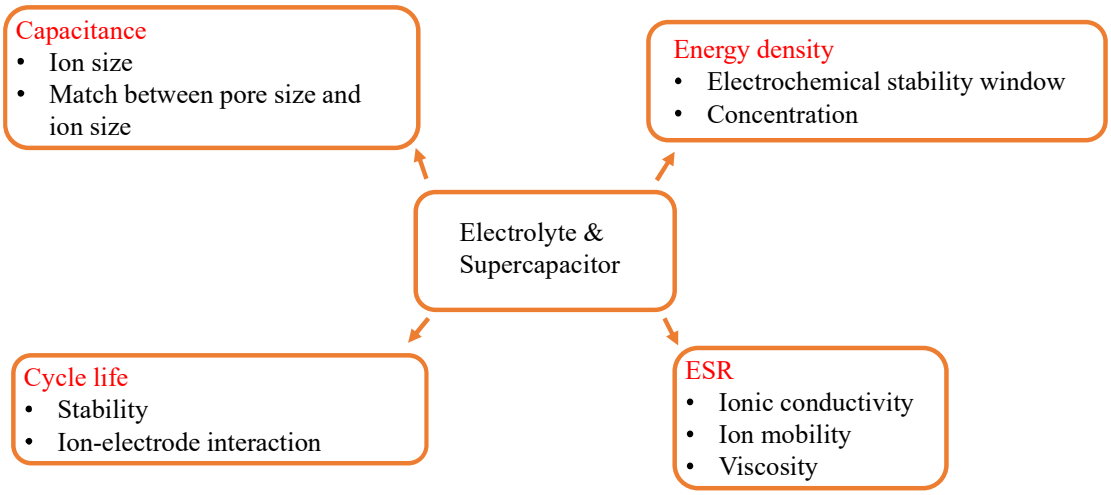

Figure 2.4. Electrolyte properties and supercapacitor.

conductive salts are used for organic electrolytes in EDLCs [127]. Tetraethylammonium tetrafluoroborate ($TEABF_4$) dissolved in propylene carbonate (PC) or acetonitrile (ACN) is one of the most common organic electrolyte [25]. The demerits of organic electrolytes are that they generally have low conductivity, high cost, and they are toxic and flammable [127]. ILs are good candidates for supercapacitors that operate at high temperatures due to their high chemical and thermal stabilities, wide operating voltage ranges and nonflammability [128].

Recently, solid-state electrolytes for energy storage devices have gained much attention since they can operate on long-term and they can prevent leakage problems [129]. Also, they function both as the ionic conducting media and the separator [124]. To date, major types of the solid-state electrolytes have been polymer based electrolytes. The polymer based solid electrolytes can be classified as the solid polymer electrolyte (SPEs), the gel polymer electrolytes (GPEs) and the polyelectrolyte.

SPEs are created by dissolution of typically lithium salts in the polymeric backbone in order to provide ionic conductivity [130]. The merits of SPEs are nonvolatility, flexibility, enhanced mechanical properties, safety, and ease of device fabrication whereas the demerits of them are related to low conductivity and poor electrochemical stability [131]. Also, the interfacial contact between electrode and electrolyte would

Table 2.4. Supercapacitors using PVA-KOH based gel electrolyte.

Electrode	**Electrolyte**	**Energy density, Wh/kg**	**Ref**
Activated carbon	PVA-KOH	14.8	[138]
Activated carbon	PVA-KOH-HQ	45	[136]
Activated carbon	PVA-KOH	10	[139]
Activated carbon	PVA-KOH-KI	7.8	[137]

be a potential problem in SPEs since SPEs form contact on the area of the electrode they touch, in contrast to GPEs [132]. GPEs are fabricated by involving the liquid electrolyte within the polymeric matrix [133]. GPEs possess mechanical integrity via the polymeric matrix and the ion mobility in liquid electrolytes provides the ionic conduction. Because of their correspondingly high ionic conductivity values, great compatibility with electrode materials, mechanical integrity and flexibility, appropriate potential window, and extended life for supercapacitor devices, GPEs are attractive candidates to demonstrate magnificent electrochemical capabilities [134, 135].

Among gel polymer electrolytes, PVA-KOH has been used in various studies due to their affordability and convenience in preparation of those electrolytes. As seen in Table 2.4, PVA-KOH has also been incorporated with chemicals to improve conductivity in the application of supercapacitors. Jinisha and others incorporated hydroquonine (HQ) and observed that energy density improved to a great extent [136]. Also, Yu and coworkers studied the effects of potassium iodide (KI) addition into gel polymer electrolyte [137].

2.2.4. Current Collectors and Separator

The heart of the supercapacitor which determines energy storage capability at the electrochemical interface is current collector. The main role of current collector is to transport charge carriers from/to electroactive materials during the charge–discharge process. High mechanical strength, strong thermal and electrochemical stabilities, elec-

trical conductivity, surface area, reduced contact resistance, light weight, and low cost are all characteristics of an ideal current collector. Nickel, stainless steel, titanium, copper, and aluminum are utilized as metal-based current collectors. Nevertheless, because of the corrosion and dissolution reactions, the usage of these metals as current collectors varies depending on the kind of electrolyte systems and the operational potential window [140]. Because of their superior electrochemical and thermal stabilities as well as their light-weight nature, carbon-based current collectors—such as carbon cloth, carbon fiber, carbon paper, glassy carbon, and graphite foil—are preferable to metal-based current collectors [141, 142]. The surface modification and heteroatom doping techniques can be used to improve electrical conductivity and decrease the charge transfer resistance [55].

Separator is another significant part of supercapacitors. Separator material provides a physical barrier between the electrodes to prevent shorting. Generally, most of three electrode systems do not have a separator while two electrodes have. Separators should possess higher physical strength, ion permeability, thermal and chemical stabilities, low thickness, high dielectric constant and good electrolyte wettability for a better performed supercapacitor [143,144]. Polymer membrane-based, paper-based, and inorganic/ceramic separators are the main separator types. Celgard known as Polypropylene is a widely utilized separator among polymer-based separators. Poly(vinylidene fluoride) (PVDF), poly(vinyl chloride) (PVC), and poly(ethylene oxide) (PEO) are other examples of polymer-based separators. The selection of separators depends on the electrolyte type [38]. For instance, PVDF can be used in the application of organic electrolytes. Because of their high porosity and mechanical resilience, paper-based separators made from natural cellulose resources are strongly recommended for large-scale fabrications, even when using organic solvents. The dielectric constant and ionic conductivity of ceramic materials are higher by nature, and this leads to an improvement in the electrochemical performances of polymer-based separators when they are incorporated into polymer-based separators [145]. Also, in recent years, there has been growing interest in the development of advanced separators with smaller pores and selective transport properties. These separators aim to provide more controlled

ion or molecular transport by utilizing materials that can selectively permit the passage of specific ions or molecules while blocking others, which improve the longevity and durability of the devices. Research has focused on the synthesis of nanostructured materials, including nanoporous polymers, metal-organic frameworks (MOFs), and two-dimensional materials like graphene oxide, which offer precise control over pore size and transport characteristics [146, 147]. These innovations have led to improved separator performance, particularly in terms of ionic conductivity, selectivity, and resistance to fouling, making them highly suitable for advanced applications that demand high precision and performance.

2.3. Testing and Performance Evaluation of Supercapacitors

Electrochemical performances of supercapacitors can be tested in a 3-electrode or 2-electrode set-up as given in Figure 2.5 (a) and (b), respectively. 3-electrode set-up can be used to test performance of electrode material regarding capacitance and operating potential. If an electrode material is found to be promising, 2-electrode measurements further can be carried out in order to investigate energy and power densities as well as cycling stability.

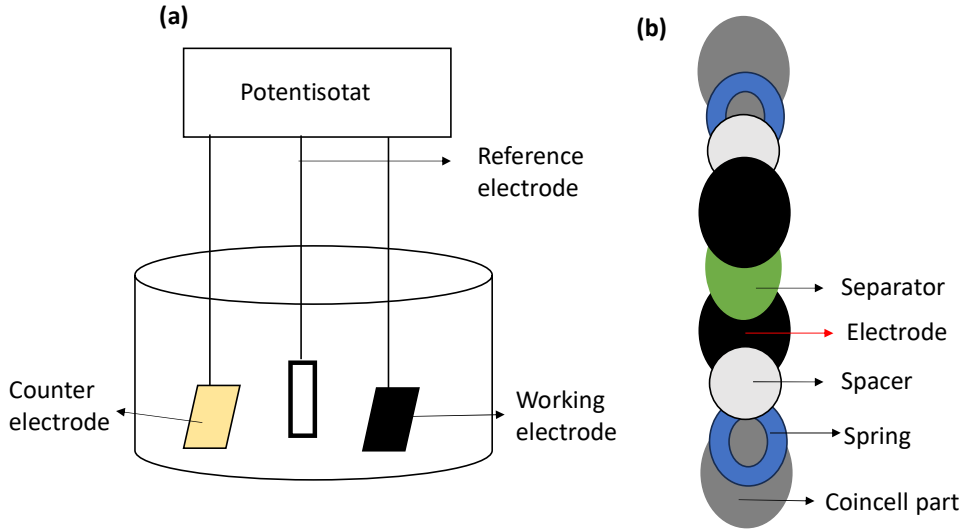

Figure 2.5. Fabrication of supercapacitors. a) 3-electrode set-up (half-cell) and b) 2-electrode set-up (device).

As can be seen from Figure 2.5 (a), 3-electrode system consists of a working electrode which is the synthesized active electrode material, a counter electrode along with a reference electrode, and a chosen electrolyte [148]. The counter electrode is generally chosen as glassy carbon and platinum since they are very conductive and inert. It generates current and change the potential of working electrode within electrolyte. The reference electrode acts as a reference point for potential measurements [45]. The counter and reference electrodes are selected based on the type of electrolytes used [149].

As can be seen from Figure 2.5 (b), 2-electrode device is made up from the anode, separator, and cathode addition to metallic spacer and a spring. Spacer and spring provide with tight contact. The corresponding specific capacitance (F/g) of a device can be equal to one quarter of the capacitance for a half-cell [150].

Cyclic voltammetry (CV) and galvanostatic charge-discharge (GCD) are both electrochemical techniques used to characterize energy storage materials but differ in their approach. CV involves sweeping the electrode potential and measuring the resulting current to analyze the electrochemical properties, reaction kinetics, and reversibility of the material. It provides fast insights into the material's electrochemical behavior. On the other hand, GCD applies a constant current to charge and discharge the material, providing real-world data on specific capacity, energy, and power densities, and is useful for assessing long-term cycling stability. While CV is quicker and ideal for fundamental characterization, GCD is more suitable for evaluating practical performance.

2.3.1. Cyclic Voltammetry

Cyclic voltammetry (CV) has been widely used to evaluate the electrochemical performance of supercapacitors. In brief, a positive voltage sweep charges to a specific voltage, and then it reverses for discharging. The electrochemical performance of supercapacitors can be assesses using the applied voltage and current response [141,151].

The capacitance from CV cycle is calculated as in

$$C = \frac{\int I * dV}{v * m * \Delta(V)}, \tag{2.7}$$

where I is the current, V is the applied potential, v is scan rate, and m is the mass of the electrode material. This can be also called as material specific capacitance (C_s). For a symmetrical cell, the relation between cell specific capacitance $C_{s,cell}$ and material specific capacitance, C_s, may be derived as in

$$\frac{1}{C_{cell}} = \frac{2}{mC_s}. \tag{2.8}$$

The cell capacitance can be given as in

$$C_{cell} = \frac{mC_s}{2}. \tag{2.9}$$

Also, cell specific capacitance, $C_{s,cell}$ can be defined as in

$$C_{s,cell} = \frac{C_{cell}}{2m}. \tag{2.10}$$

By combining equations of 2.9 and 2.10, the relation between cell specific capacitance and cell capacitance is established as in

$$C_{s,cell} = \frac{C_s}{4}. \tag{2.11}$$

Therefore, the capacitance of two electrode set-up is calculated as in equation 2.7 while that of three electrode is divided by 4 of the capacitance from two electrode set up.

The EDLCs and PCs electrochemical behaviour can be differentiated by CV method. EDLCs as in Figure 2.6 (a) show quasi-rectangular shape whereas the capacitance characteristic of PCs as in Figure 2.6 (b) is different. CV curves of PCs show redox peaks [152].

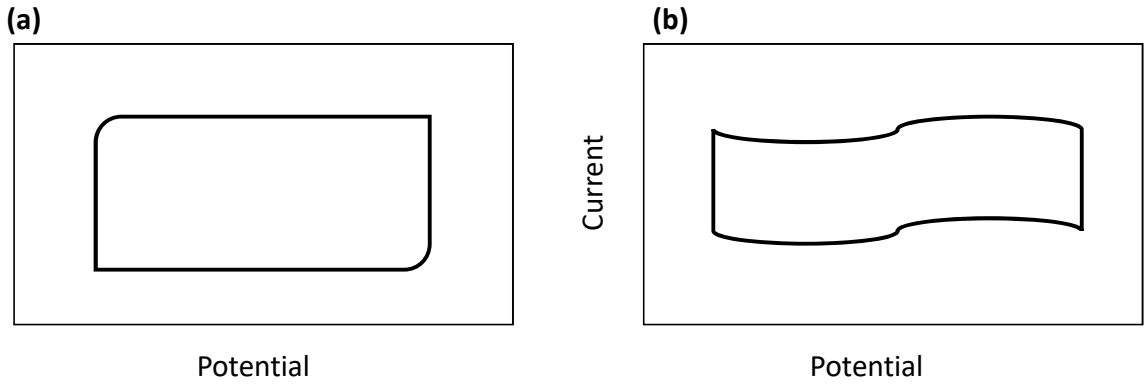

Figure 2.6. Illustrative current-potential properties of a) EDLC and b) Pseudocapacitor.

The higher integrated area of CV curve shows higher capacitance while higher response currents indicate higher active surface area of electrode, meaning facilitated penetration of electrolyte [153].

2.3.2. Galvanostatic Charge-Discharge

Galvanostatic charge-discharge (GCD) is a traditional evaluation method for capacitance, energy density, power density, and cycle stability. In the GCD process, the responsive potential relative to time is measured. The capacitance from charging-discharging cycle is calculated as a function of current density using

$$C = \frac{I * \Delta(t)}{m * \Delta(V)}, \tag{2.12}$$

where I is the discharged current, Δt is the discharge time, m is the mass of the electrode material, and ΔV is the voltage change. EDLC materials (Figure 2.7 (a)) show linear GCD curves which indicate good electrochemical capacitive nature [150]. However, PCs have non-linear variation (Figure 2.7 (b)) due to quasi reversible faradic reactions [154].

Energy and power densities are calculated for a packaged supercapacitor,; namely for 2-electrode system, as these parameters are not suitable for material level since they depend on the mass of the dead components and cell architecture [150].

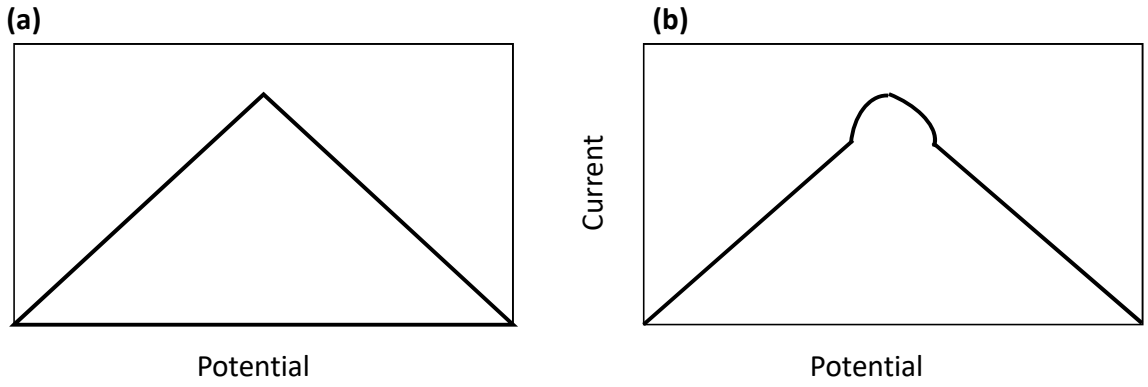

Figure 2.7. Illustrative potential-time properties of a) EDLC and b) Pseudocapacitor.

Energy density for a 2-electrode device is defined as in

$$E = \frac{1/2 * C}{V^2}, \tag{2.13}$$

where C is capacitance and V is voltage [155].

Power density for a 2-electrode device can be calculated as in

$$P = \frac{V^2}{4 * R}, \tag{2.14}$$

where V is voltage and R is equivalent series resistance (ESR) [155].

3. MATERIALS AND METHODS

3.1. Materials and Equipments

All the materials that were used for the experimental studies are given in Table 3.1.

Table 3.1. Materials used for the experimental studies.

Name	Formula	Source
Potassium hydroxide	KOH	Merck
Hydrochloric acid	HCl	Merck
Acetylene black	AB	Nanografi
Polytetrafluoroethylene	PTFE	Nanografi
N-Methyl-2-pyrrolidone	NMP	Merck
Commercial activated carbon	Com. AC	MTI. Corp
1-Ethyl-3-methylimidazolium tetrafluoroborate	EMIMBF4	Iolitec (electrical grade)
Acetonitrile	ACN	Sigma-aldrich (99.999%)
Polyvinyl alcohol	PVA	Merck

All the equipments that were utilized for the experimental studies are given in Table 3.2.

Table 3.2. Equipments used for the experimental studies.

Tubular Furnace	Protherm
Centrifuge	NÜVE 400
Ultrasonicator	Bandelin Sonoplus HD 4400
Potentiostat	BioLogic SP300

3.2. Activated Carbon Preparation Route

Cabbage-leaves based activated carbon preparation route is shown in Figure 3.1.

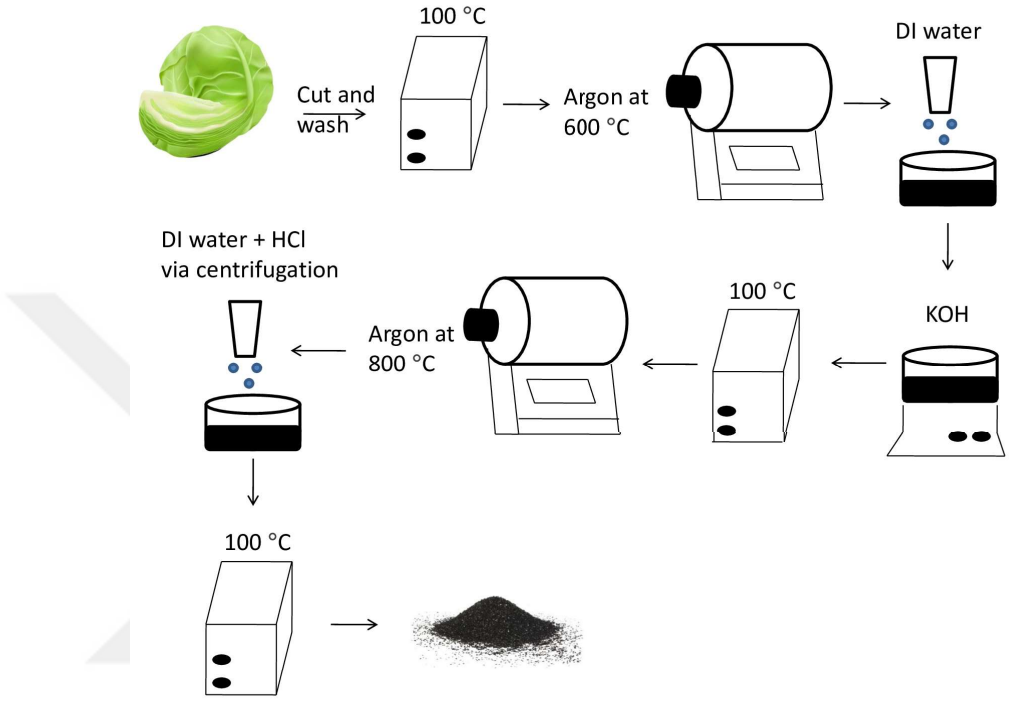

Figure 3.1. Activated carbon preparation route.

4 grams of chopped cabbage leaves were placed in a tubular furnace (Protherm), where they were calcined at 600 °C for two hours while being circulated with argon (Ar). The calcined cabbage leaves were cleaned with distilled water and then submerged in a solution of potassium hydroxide (KOH, Merck, pellets for analysis) with a mass ratio of 4:1 (KOH to calcined material). The mixture was then agitated for 10 hours at room temperature. The resultant material was dried at 80 °C and then activated in a tubular furnace at 800 °C for two hours, with a heating rate of 5 °C/min in an Ar atmosphere. Lastly, the products underwent centrifugation (1500 rpm, 20 min, 25 cycles) to be cleaned with distilled water and 1 M hydrochloric acid (HCl, Merck, 37 % for solution). The resulting solution was put into oven at 80 °C overnight for drying and the final product was named AC.

The following reactions are expected to occur during chemical activation which gives a way to pore creation due to erosion of carbon material [156].

Table 3.3. Chemical reactions during chemical activation.

$2C + 6KOH \rightarrow 2K_2CO_3 + 2K + 3H_2$	(1)
$K_2CO_3 \rightarrow K_2O + CO_2$	(2)
$K_2CO_3 + 2C \rightarrow 2K + 3CO$	(3)
$K_2O + C \rightarrow 2K + CO$	(4)
$2K + 2H_2O \rightarrow 2KOH + H_2$	(5)

3.3. CQD Preparation

Carbon quantum dots were obtained from citric acid (CA, Sigma-Aldrich) and urea (Sigma-Aldrich) as raw materials by solvothermal processes (Figure 3.2) [157]. Briefly, 0.384 g citric acid and 0.060 g urea were dissolved into 10 mL dimethylformamide (DMF, Sigma-Aldrich) and then sonicated to obtain a homogeneous solution. The mixture was transferred into teflon-lined stainless autoclave (50 mL) and heated to 180 °C for 6 h. The cooled resultant brown solution was purified within the dialysis bag (MWCO: 0.5 kDa, Spectrum Laboratories Inc. (USA)) for 15 min to remove residual precursor molecules. Ultra-pure water were freshly prepared in Millipore Direct-Q3 water purification systems. The obtained CQD solution was stored at +4 °C for further experiments.

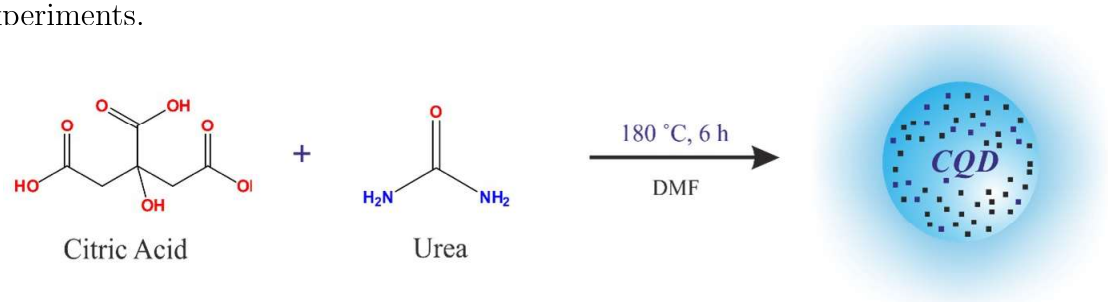

Figure 3.2. Schematic illustration for the preparation of CQD by bottom-up approach.

3.4. Preparation of Gel Electrolyte

The gel polymer electrolyte films were prepared by solution-casting as described here. First, 1 g of KOH was dissolved in 25 mL of deionized water by stirring on a magnetic stirrer at 95 °C for 3 h. Simultaneously, 1 g of polyvinyl alcohol (PVA, Merck) was also dissolved in 25 mL of water by stirring on a magnetic stirrer at 80 °C for 3 h. The two are subsequently mixed to form a homogeneous mixture. The mixture was cast into a glass Petri-dish and oven-dried at 95 °C until the water is completely removed and a white solid film was formed. SEM analysis of the gel film revealed an approximate thickness of 64-128 μm (Figure A.1). For CQD incorporation, a mixture of 30 % acetonitrile (ACN) and 70 % water was prepared. Subsequently, 1 g of KOH and 1 g of polyvinyl alcohol (PVA, Merck in powder form) were dissolved separately each in 25 ml of the ACN-water solution and mixed using a magnetic stirrer at 95 °C for 3 hours. The two solutions were then combined and stirred vigorously for 15 minutes to form a homogeneous mixture. CQDs, dissolved in dimethylformamide (DMF) as 5mg/mL, were added to the PVA-KOH/ACN-water gel electrolyte at varying concentrations (0.5 %, 1 %, and 1.5 % by weight). The mixture was stirred at 70 °C for 3 hours to ensure uniform dispersion. Finally, the homogeneous solution was cast into a glass Petri-dish and dried at 95 °C for $\simeq$ 1 hour to form the gel polymer electrolyte films.

3.5. Preparation of 3-Electrode Systems

At first, 3-electrode measurements were carried out in order to obtain electrochemical information of a single material. This set-up includes the reference electrode which measures the potential without being affected by the current flow, providing a better control of the potential at the working electrode. For preparation of the working electrode, the active electrode material (AC) was combined with 10 wt. % acetylene black (AB, Nanografi) and 20 wt. % polytetrafluoroethylene (PTFE, Nanografi) to create the working electrode. For 10 minutes at beginning, all of the solid ingredients were mechanically stirred. N-Methyl-2-pyrrolidone (NMP, Merck) was then added in a

volume of 2 ml, and the suspension was stirred for 15 minutes using a magnetic stirrer. It was then heated to 70 °C and mixed for two hours at 300–400 rpm. After that, it was mixed for ten hours at room temperature using a magnetic stirrer and ultrasonicated for 30 minutes (at an amplitude of 30 %). Lastly, a nickel foam of 1 cm by 1 cm was coated with the mixture, and a mass loading of $\simeq$1 mg was added. The working electrode was made and then baked at 80 °C for an overnight drying period. Ultimately, it was compressed for a minute under 1000 kg/cm^2. Using commercial activated carbon (MTI Corp.), the same process was used to create functional electrodes for comparison.

The working electrode, platinum counter electrode, 1.5 M or 2.5 M 1-ethyl-3-methylimidazolium tetrafluoroborate (EMIMBF$_4$, Iolitec, electrical grade) in acetonitrile (ACN, Sigma-Aldrich, 99.999 %) electrolyte, and a pseudoreference electrode made of platinum wire wrapped in a fritted glass sheath and filled with the same electrolyte were the components of the standard 3-electrode setup used for the CV measurements. The reason for usage of EMIMBF$_4$ is that it has high ionic conductivity among ionic liquids. An electronically operated BioLogic SP300 potentiostat was used for the electrochemical characterisation process.

3.6. Preparation of 2-Electrode Systems

2-electrode measurement was carried out to gather information about electrochemical performance of device. The current is passed through the working electrode, and the potential is measured relative to the reference electrode which also carries some of the current. As for preparation, solution-casting was used to form the gel polymer electrolyte films, as explained here. First, 25 mL of deionized water and 1 g of KOH were dissolved over the course of three hours at 95 °C using a magnetic stirrer. Concurrently, 25 mL of water were mixed with 1 g of polyvinyl alcohol (PVA, Merck) and heated to 80 °C for three hours using a magnetic stirrer. After that, the two are combined to prepare a homogenous mixture. After the mixture was poured onto a glass Petri dish, it was put into oven at 95 °C to remove all traces of water and form a white, solid layer.

AC was mixed with AB and PTFE with a weight ratio of 8:1:1 in an agate mortar for 10 minutes. NMP was added to the mixture to form a slurry containing 0.15 g/ml AC. A magnetic stirrer was then used to mix the mixture for two hours at 70 °C at 350 rpm. After the slurry had cooled to room temperature, it was stirred magnetically and kept there all night. A flexible PET film (1 cm^2) was printed with silver nanoparticles ink (Sigma-Aldrich) and heat-treated for five hours at 130 °C. After the slurry was cast onto the silver current collector, the films were dried for one hour at 95 °C to thoroughly evaporate the solvent. Additives such as CQDs, RGO or BRGO were combined with AC in a certain amount. RGO and BRGO was obtained from Graphitene. The composite electrode materials were prepared as follows. To fabricate films that contain CQDs, 5–10 wt.% CQD powder was mixed with AC in an agate mortar. The mixture was dispersed in ethanol and was ultrasonicated for 30 min. The slurry was dried and AC/CQD mixture was obtained in powder form. This was mixed with 10 wt.% PTFE and NMP to obtain a slurry that contain 0.15 g/ml AC/CQD. This slurry dispersed by magnetic stirring at 350 rpm for 2 h at 70 °C and overnight at room temperature. The samples were named as AC-5CQD (5 wt. %) and AC-10CQD (10 wt. %.) For RGO, 15-20 wt. % RGO was physically mixed with AC and the mixture was dispersed in ethanol and ultrasonicated for 30 min. After solution was dried, the electrode material (AC-15RGO or AC-20RGO) was mixed with PTFE and AB as explained in section 3.5. The same procedure was repeated to incorporate BRGO into AC. The samples were named according to weight percentages of BRGO in AC-PTFE-AB (AC-5BRGO, AC-10 BRGO and AC-15BRGO).

The gel film electrolyte was sandwiched between symmetric working electrodes and pressed to ensure good contact between layers.

3.7. Structural Characterizations

Using an automated pore size analyzer from Micromeritics ASAP 2020 Plus Chemi, nitrogen (N_2) adsorption-desorption analysis was used to examine the micro-pore structure of the samples. The specific surface area was determined using the

Brauner Emmet Teller (BET) method after the materials were degassed for 6 hours at 70 °C. Powder active electrode materials (Reinshaw inVia, λ= 532 nm) were subjected to Raman investigation. Using a Thermo K-Alpha X-Ray Photoelectron Spectrometer, X-ray photoelectron spectroscopy (XPS) was used to examine the surface chemistry of the materials. Using a Shimatzu 2600, ultraviolet-visible (UV-Vis) spectroscopy was used to analyze CQDs. The Bruker Vertex 80v spectrometer was used to perform Fourier-transform infrared (FTIR) spectroscopy. The gel electrolytes were examined by thermal gravimetric analysis (TGA) (TA Instruments,SDT 650) and X-ray diffraction (XRD) (PANalytical X'Pert PRO, lambda = 1.540 59A).

3.8. Electrochemical Characterizations

Electrochemical characterizations (CV and GCD) were conducted on BioLogic SP300 potentiostat instrument using the standard 2-electrode set-up and 3-electrode set-up.

4. DESCRIPTIVE STATISTICAL ANALYSIS OF SUPERCAPACITORS WITH EXPERIMENTAL VALIDATION

This chapter is based on a collaborative study published in *Journal of Power Sources, 2023* by Kaya D., Koroglu D. et al. [158]. My contributions included conducting experiments, and interpreting the results related to experimental work. Duygu Kaya contributed to optimization of machine learning algorithms.

A total of 1723 data points from 94 published articles on carbon-based supercapacitors were collected, and the relationship between descriptors (input variables) and capacitance values was identified [158]. The dataset was analyzed using basic descriptive statistics to highlight general trends in the field and to compare the performance of various materials. This dataset was used to obtain a machine learning model that estimates capacitance by one of the colleagues. Artificial neural network (ANN) model was established and an experimental data was used as a test data to validate the real-life performance and robustness of the constructed ANN model.

4.1. Descriptive Statistical Analysis of Supercapacitors

1723 data points from 94 published articles on the carbon based supercapacitors were extracted and the relations between descriptors (input variables) and capacitance values was established. The dataset was analyzed using simple descriptive statistics to show the general trends in the field, and compare the performance of materials. The possible descriptors can be categorized in two main groups: categorical and numerical. Categorical variables are electrode materials, electrode material preparation methods, electrolyte types, current collector, binder, and separator. Numerical variables can take any value within a physically reasonable range and include the parameters associated with the microscopic structure of the electrode material including nano-/micro-/meso-pore size distribution, pore volume, specific surface area(SSA), de-

fect and doping content, oxygen/nitrogen/boron concentration, electrolyte properties including concentration, scan rate and absolute potential window.

As illustrated in Figure 4.1 (a), activated carbons are the most commonly used electrode materials due to their high surface area, good electrical conductivity, and low-cost. Graphene, another prominent electrode material, is highly favored for its high surface area and superior electrical properties. Additionally, carbon materials exhibiting diverse morphologies, such as carbon nanoflakes, nanobelts, nanofibers, and nanosheets, have an influence on the capacitance of energy storage devices. As depicted in Figure 4.1 (a) , both activated carbon and graphene emerge as key electrode materials, widely used for their ability to deliver good capacitance performance.

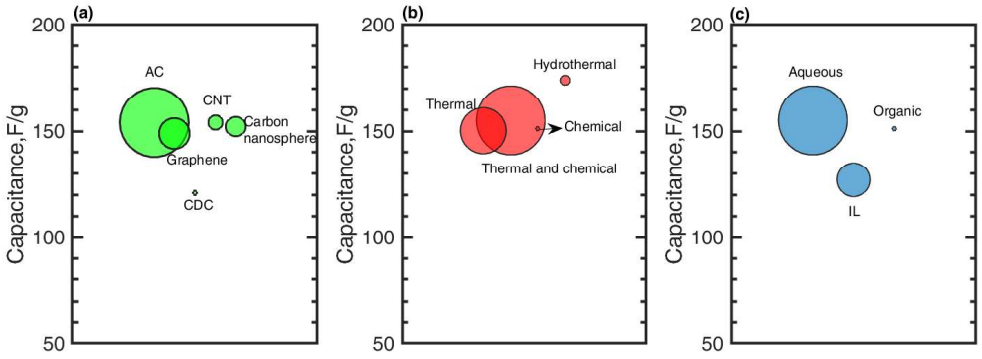

Figure 4.1. Performance of a. Electrode materials, b. Electrode material preparation methods and c. Electrolyte types.

Various electrode preparation methods are employed in the literature, including thermal activation, chemical activation, a combination of thermal and chemical activation, hydrothermal synthesis, and chlorination. As depicted in Figure 4.1 (b), thermal activation is widely utilized in our data, as it allows for precise control over porosity and pore size distribution by adjusting the activation temperature. Chemical activation is another common technique, particularly effective for achieving high surface area and well-developed porosity. The hydrothermal method, conducted at moderate temperatures, prevents degradation of the carbon structure that may occur at elevated temperatures. Chlorination, primarily employed for the preparation of carbons derived from chlorinated precursors (CDC), offers the advantage of achieving both

atomic-level porosity and an extensive specific surface area. However, chlorination is typically carried out at higher temperatures, which may become detrimental to the carbon framework.

The performance of supercapacitors is influenced not only by the electrodes but also by the electrolytes. Two critical factors for electrolytes are electrical conductivity and electrochemical stability. Higher electrical conductivity enables faster charging and discharging of the supercapacitor. Likewise, the stability of the electrolyte under the applied potential is crucial. Non-aqueous electrolytes exhibit greater stability compared to aqueous electrolytes and ionic liquids. As illustrated in Figure 4.1 (c), organic electrolytes yield better performance.

The core components of a supercapacitor, which ultimately determine its energy storage capacity at the electrochemical interface, include the current collector, binder and separator. The current collector plays a pivotal role in facilitating the efficient transport of charge carriers to and from the electroactive materials during the charge-discharge cycles, thus directly influencing the device's overall energy performance. As can be seen from Figure 4.2 (a), Nickel is mostly used as current collector due to its favorable combination of electrical conductivity, mechanical strength, and resistance to corrosion.

Further, binders and separator materials are also significant to the functionality of supercapacitors. Binders add the mechanical integrity to the electrode by binding carbon particles together, introduce a degree of electric and ionic resistance into the system. This resistance can adversely affect the power capabilities of the supercapacitor, as the charge transport efficiency is impeded. Notably, 44 % of studies in the existing literature choose not to use binders, possibly due to their negative impact on performance (Figure 4.2 (b)). However, a majority of studies continue to incorporate binders, likely because of their critical role in enhancing the mechanical integrity and overall performance of the electrode material.

The separator, on the other hand, serves as a vital component that provides a physical barrier between the positive and negative electrodes, thereby preventing electrical short circuits. While most three-electrode systems do not require a separator, it is an essential element in two-electrode systems, where the risk of shorting is greater due to the direct contact between the electrodes. Celgard, polypropylene and polyethylene membrane, is commonly used separator, 21 % as can be seen in Figure 4.2 (c), due to the fact that it is engineered with a porous structure that allows electrolytes (liquid or gel) to permeate easily, which facilitates the movement of ions across the separator. Together, these materials contribute to the overall efficiency and performance of supercapacitors.

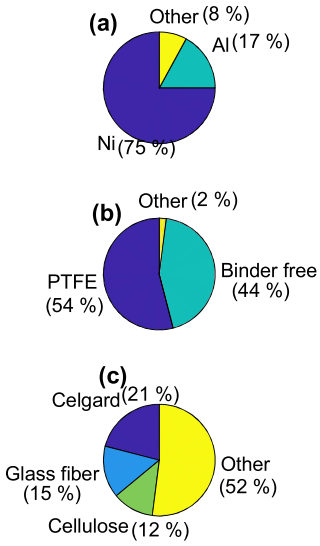

Figure 4.2. Distribution of a. Current collector , b. Binder and c. Separator in literature.

The development and optimization of supercapacitors are governed by a variety of structural and electrochemical characteristics as given by Figure 4.3. Below, key parameters and their roles for the performance of supercapacitors have been discussed.

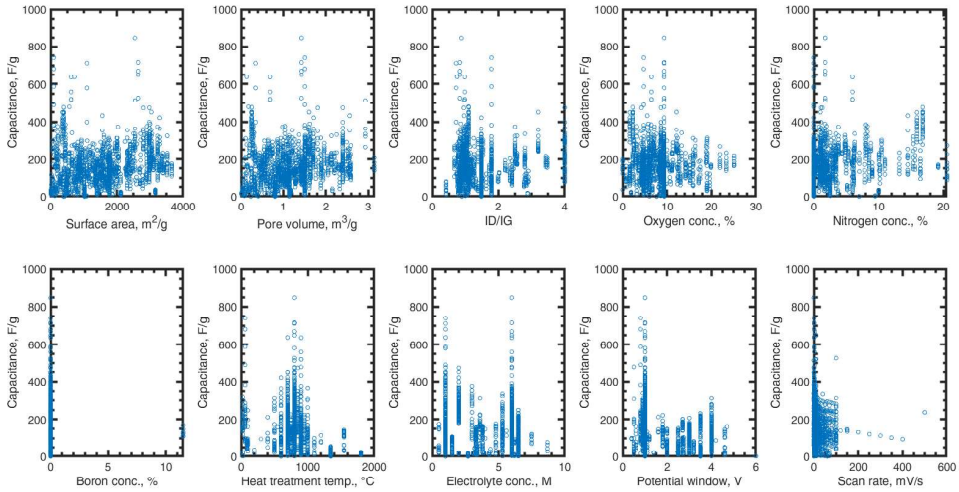

Figure 4.3. Capacitance as a function of numerical input variables.

Firstly, the surface area of an electrode material is one of the most critical factors that governs its performance in energy storage applications. A larger surface area typically correlates with a higher number of accessible sites for charge storage, thereby enhancing the capacitance and energy density of the material. The variation from 6 to 3500 m^2/g suggests that the electrode material can vary from being relatively compact and less efficient to highly porous, which would provide a far greater surface for interaction with the electrolyte. Materials with a surface area in the higher range (above 1000 m^2/g) often exhibit superior electrochemical performance by accommodating more ions during charge/discharge cycles, thereby enabling faster charge transfer and higher power density. However, it is crucial to balance surface area with mechanical and structural stability; overly high surface areas can lead to material degradation, poor conductivity, or thermal instability.

Pore volume is linked to the surface area and is another important characteristic which has impact on energy storage capacity. The pore structure dictates the accessibility of the electrolyte ions to the electrode surface. Larger pore volumes are desirable as they provide more space for storing charge in the form of ions. However, the optimal pore volume is often material-dependent; while larger pores enhance ion storage, excessively large pores may reduce the electrode's ability to maintain structural integrity, and excessively small pores may limit the electrolyte's accessibility. A

maximum pore volume of 2.60 cm^3/g (Figure 4.3) implies that the material in question can accommodate a significant volume of electrolyte ions, which is beneficial for high-capacity energy storage. The interconnectivity of pores also plays a crucial role in ion transport and rate capability, making a balanced porous architecture essential for optimal performance.

The ID/IG ratio, derived from Raman spectroscopy, measures the disorder or defects in the carbon structure of the material. The D-band (disordered band) is associated with defects, while the G-band (graphitic band) reflects well-ordered carbon structures. A low ID/IG ratio (close to 0.42) is indicative of a highly ordered, graphitic structure, which typically favors better electrical conductivity, structural stability, and overall electrochemical performance. Higher ID/IG ratios (approaching 4 in Figure 4.3) suggest increased defect density in the material, which can lead to reduced conductivity and compromised electrochemical behavior. While defects can sometimes enhance pseudocapacitance by providing additional active sites for charge storage, an excessive number of defects can detract from the material's performance by increasing resistive losses. Therefore, an optimal balance between order and defect density is necessary, with a low to moderate ID/IG ratio being ideal for most applications.

The incorporation of functional groups, such as oxygen and nitrogen, onto the surface of carbon-based electrode materials has been shown to improve electrochemical performance by enhancing the material's wettability, conductivity, and charge storage capacity. Oxygen-containing groups (such as carboxyl, hydroxyl, and carbonyl groups) generally enhance the material's surface polarity, enabling better electrolyte interaction and improved ion adsorption. Nitrogen doping, on the other hand, can increase the conductivity of the material, modify the electronic structure, and introduce additional electrochemical activity. A maximum of 25 % oxygen and 20 % nitrogen concentration suggests that the materials are likely tailored for high capacitance and pseudocapacitance behavior. However, there is a delicate balance to strike, as excessive functionalization could lead to the formation of weak or unstable bonds that may degrade over time, negatively impacting cycling stability.

Boron is often used as a dopant to improve the conductivity and electrochemical performance of electrode materials. In low concentrations, for instance concentrations lower than 0.5 as in Figure 4.3, boron can enhance the structural stability and electron mobility within carbon-based electrodes. However, at concentrations higher than 1 %, boron may introduce structural defects which might have an adverse impact on material's stability and long-term performance. This observation underlines the importance of optimizing the concentration of dopants. Materials with low boron concentrations are generally considered to exhibit better performance due to their ability to maintain an optimal balance between conductivity and structural integrity.

Heat treatment is a critical processing step in the synthesis of electrode materials, as it can influence the crystallinity, porosity, and overall electrochemical behavior of the material. However, temperatures above 1000 °C, as can be seen in Figure 4.3, are typically avoided because they can cause the material to undergo significant structural changes, such as the collapse of the porous network or the loss of functional groups. While heat treatment can enhance graphitization and improve conductivity, excessive temperatures can degrade the material, leading to a decrease in surface area, pore volume, and overall performance. The temperature range selected for heat treatment thus plays a pivotal role in determining the material's electrochemical properties.

The electrolyte concentration directly influences the ionic conductivity and the efficiency of ion transport within the electrode material. A higher concentration of electrolyte generally increases the ion mobility, which is beneficial for the rate performance and overall charge/discharge cycles. However, excessively high concentrations may lead to side reactions or undesirable interactions with the electrode material, potentially affecting its stability and performance. The range of 0.5 to 6.5 M as can be seen by Figure 4.3, indicates that a fine-tuning of the electrolyte concentration is required based on the type of electrolyte used, and the nature of the electrode material itself. The optimal electrolyte concentration should maximize ionic conductivity while maintaining the stability and efficiency of the electrochemical process.

The potential window, defined by the voltage range in which the electrode material can operate without degradation, is crucial for determining the energy density of the electrode. A broader potential window allows for a higher voltage range, which in turn leads to a higher energy density, as more charge can be stored. However, the potential window must be balanced with the stability of the electrode material. Operating outside of the material's stable potential window can lead to irreversible chemical reactions, degradation of the material, or loss of electrochemical capacity. Therefore, careful optimization of the potential window is essential for maximizing the performance of energy storage devices.

The scan rate refers to the speed at which the potential is varied during electrochemical measurements, such as cyclic voltammetry, and is a key parameter in determining the capacitance of electrode materials. A higher scan rate typically reduces the time available for ion diffusion and charge storage, which may lower the observed capacitance. On the other hand, low scan rates allow more time for ion movement and charge accumulation, resulting in higher capacitance. The choice of scan rate is critical in characterizing the performance of the electrode material, as it affects the apparent capacitance, power density, and rate capability. Optimizing the scan rate for a specific application ensures that the material's performance is accurately assessed under realistic operating conditions.

Overall, the performance of electrode materials is governed by many factors, including surface area, pore volume, doping concentrations, heat treatment conditions, electrolyte concentration, and the electrochemical properties of the material. Each of these factors must be carefully optimized to achieve the desired balance between energy density, power density, cycling stability, and overall efficiency. Understanding the interrelationships between these parameters allows for the design of advanced electrode materials with superior performance for energy storage applications, driving forward the development of more efficient and durable energy storage devices.

This literature data collection was utilized to develop a machine learning algorithm designed to estimate capacitance, as part of a collaborative effort by one of the colleagues. Various models were constructed, including linear regression, lasso regression, regression tree, random forest, gradient boosting, and artificial neural networks (ANN). The performance of these models was evaluated on two datasets: literature data that was not included in the training process and experimental data obtained after the model was developed. As depicted in Figure 4.4, the artificial neural network (ANN) was identified as the most effective machine learning algorithm. Following a thorough hyperparameter tuning process, the optimized ANN model, consisting of a single hidden layer with 16 neurons, was selected. The performance of the model was assessed through 10-fold cross-validation, yielding a root mean square error (RMSE) of 19.2 F/g, while the test dataset from experimental studies achieved an RMSE of 26.5 F/g [158].

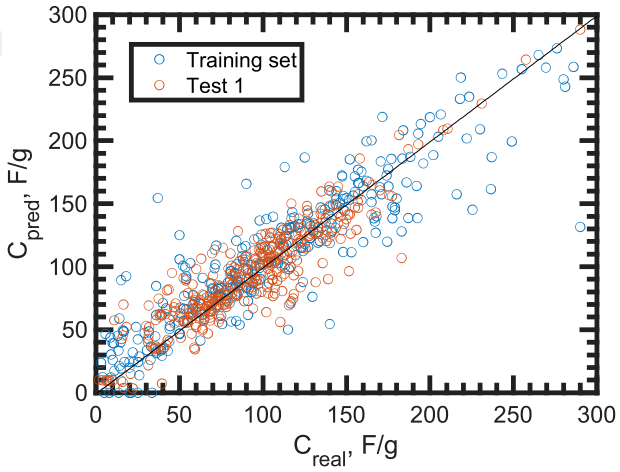

Figure 4.4. Comparison of real capacitance and predicted capacitance values from the ANN model.

4.2. Experimental Validation

Activated carbon (AC) is synthesized via the thermal and chemical activation method as explained in section 3.2, and subsequently performed structural (Figure 4.5) and electrochemical characterizations (Figure 4.6) are given.

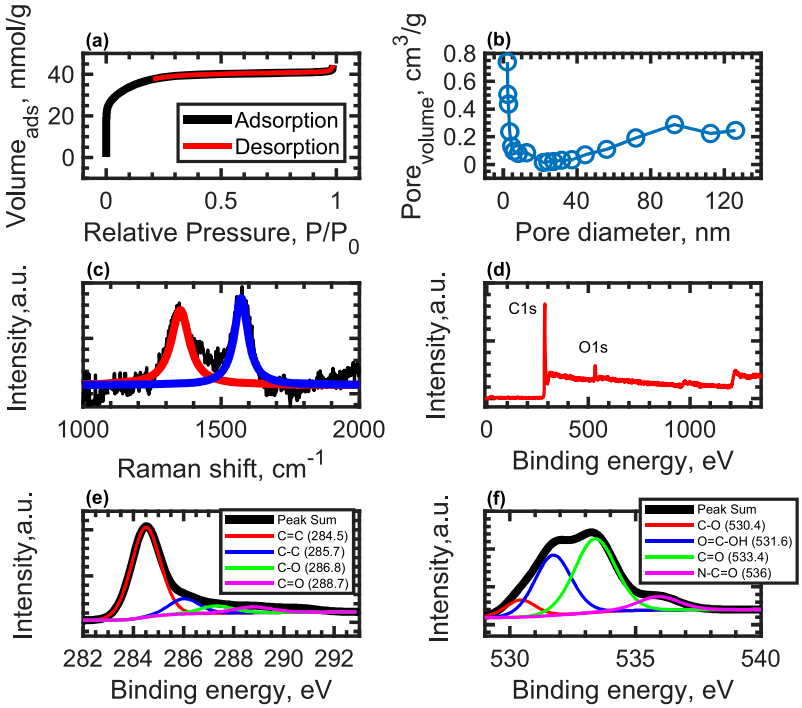

Figure 4.5. AC a. N_2 ads/des isotherms, b. Pore size distribution, c. Raman spectra, fitting curves. Red line represents the Lorentzian fit to the D-peak and Blue line represents the BWF fit to the G-peak, d. The total XPS spectra, e. The XPS Deconvolution of C1s spectra and f. The XPS Deconvolution of O1s spectra.

According to Raman, the peaks located around 1360 and 1570 cm^{-1} are assigned to D and G bands and ID/IG ratio of 0.92 is obtained, which indicates the synthesized AC has a defective structure. Defects provide AC with more active sites; thereby increasing capacitance. BET surface area of AC is determined as 3038 m^2/g. Nitrogen adsorption–desorption isotherms of AC reveal microporous structure is well developed in the active electrode material with some amount of mesopores. The presence of both micropores and mesopores enhances charge adsorption on AC surface while also facilitating transport inside the porous network. A C/O ratio of 11 is obtained from XPS analysis.

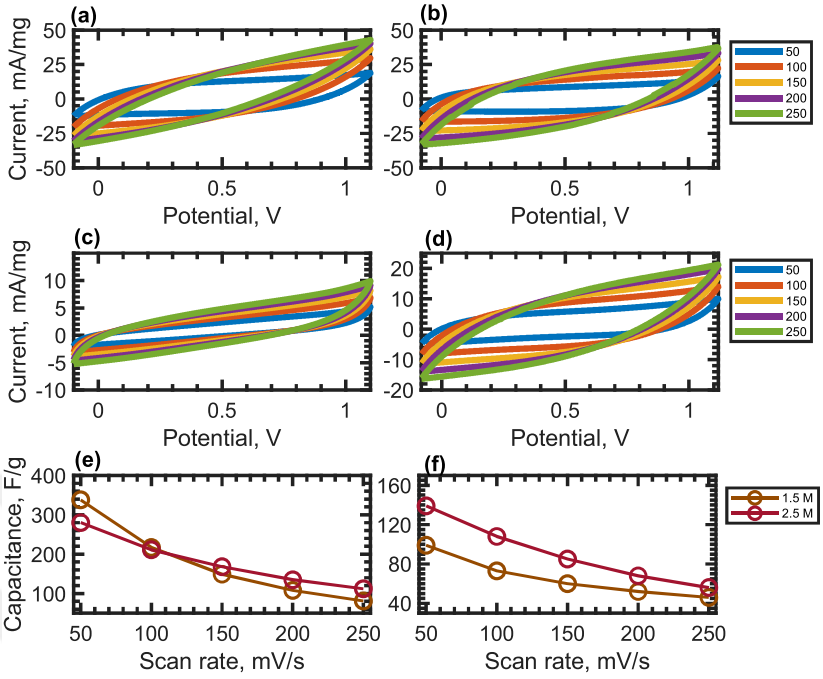

Figure 4.6. a. AC CV of different scans with 1.5 M [EMIM$^+$][BF$_4^-$], b. AC CV of different scans with 2.5 M [EMIM$^+$][BF$_4^-$], c. Commercial AC CV of different scans with 1.5 M [EMIM$^+$][BF$_4^-$] d. Commercial AC CV of different scans with 2.5 M [EMIM$^+$][BF$_4^-$], Capacitance vs. scan rate e. for AC and f. for commercial AC.

In order to assess the performance of cabbage-derived activated carbon, cyclic voltammetry measurements were performed in a 3-electrode configuration. Figure 4.6 (a) and (b) shows the cyclic voltammetry profiles of AC electrodes in 1.5 and 2.5 M [EMIM$^+$][BF$_4^-$]/ACN mixtures at 1.2 V at scan rates between 50 and 250 mV/s. It can be seen that all voltammograms exhibit quasi-rectangular behavior with anodic and cathodic runs almost symmetrical. This indicates nearly ideal capacitive behavior with charge stored primarily through physical ion adsorption. The superior electrochemical performance of cabbage-derived AC can be attributed to its high defect density and the presence of oxygen functionalities, as identified in the Raman and XPS analysis. The increased ID/IG ratio highlights the presence of structural defects, which improve quantum capacitance by increasing the density of states at the Fermi level, thus enhancing the overall capacitance of the material. Furthermore, the oxygen-containing groups increase the wettability of the carbon surface, promoting better ion transport through the porous structure and further contributing to the improved capacitance.

The capacitance C of the electrodes was calculated as a function of scan rate using the following expression

$$C = \frac{\int I dV}{v\Delta(V)}, \tag{4.1}$$

where I is the current in amperes, V is the applied potential in volts, v represents the scan rate in V/s and and ΔV is the potential window. To determine the specific capacitance C_s in farads per gram (F/g) for the three-electrode measurements, the capacitance was normalized by the electrode mass m (in grams) using

$$C_s = \frac{C}{m}. \tag{4.2}$$

Maximum capacitance is obtained at 50 mV/s for both cabbage-derived and commercial ACs. It can be observed from Figure 4.6 (e) that while the current densities increase with scan rate, the corresponding specific capacitance decreases from 338 to 81 F/g at 1.5 M [EMIM$^+$][BF$_4^-$]/ACN. This is attributable to the fact that at lower scan rates, electrolyte ions are capable of diffusing into the electrode pores more effectively, while at higher scan rates, a smaller portion of the ion-accessible specific surface area is utilized. As it can be seen from Figure 4.6 (e) and (f), both for cabbage- derived AC and commercial activated carbon, capacitance is higher in the more concentrated electrolyte except for the smallest scan rate. An increase in current density with increasing scan rate from 50 to 250 mV/s is observed in Figure 4.6 (a), (b), (c), and (d), indicating the capacitive nature of energy storage. Among the two different types of ACs, cabbage-derived AC exhibits superior performance at all scan rates. This aligns with the expectation that the material possessing a greater proportion of pores with diameters similar to those of ions exhibits higher specific and areal capacitance. [159–163]. Additionally, cabbage-derived AC has higher specific surface area and pore volume as well as higher ID/IG and C/O ratio, supporting that AC has a better electrochemical performance as compared to commercial one. Overall, both cabbage-derived AC and commercial AC electrodes exhibit superior capacitance performance in 2.5 M [EMIM$^+$][BF$_4^-$]/ACN electrolyte. This is consistent with previous experimental and modelling work that exhibit enhancement in capacitance with increasing bulk

electrolyte concentration at intermediate electrolyte concentrations due to improved ion polarization in electrode pores [57, 159, 164–168].

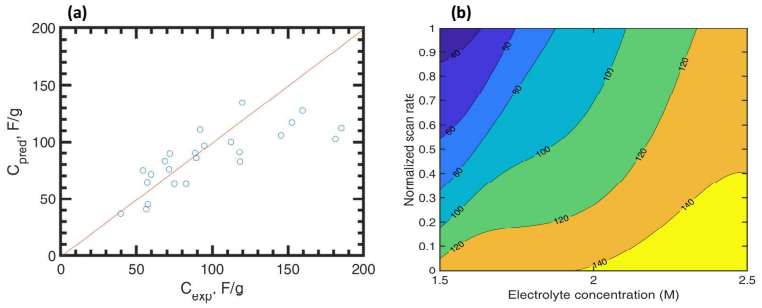

Figure 4.7. a. Comparison of experimental capacitance and predicted capacitance obtained from the ANN model and b.Effect of electrolyte concentration and normalized scan rate on capacitance (F/g).

As seen in Figure 4.7 (a), predictions of ANN model are consistent with the experimental capacitance values, this indicates that our model is able to capture the relationship between input variables and capacitance for the experimental data set. ANN model can provide a framework that is applicable to real-life design problems, which further proves that ANN can provide guidelines to experimental in designing supercapacitors with improved capacitance. Figure 4.7 (b) shows that the relationship between the normalized scan rate and electrolyte concentration plays a crucial role. With a higher electrolyte concentration, the ionic conductivity increases, which improves the capacitance. The ions can move more freely, leading to better performance even at lower scan rates. With slower scan rates, the ions have more time to diffuse, so the supercapacitor can charge and discharge more effectively, leading to better energy storage and higher power efficiency. This region represents the ideal case for achieving a balance between energy and power densities with low degradation. The optimum electrolyte concentration was found as 2.5 M while normalized scan rate lower than 0.3 gave better results.

5. FLEXIBLE SOLID-STATE SUPERCAPACITORS BASED ON BIOWASTE-DERİVED ACTIVATED CARBON AND NANOMATERIALS FOR BETTER PERFORMANCE

In this part, flexible solid-state supercapacitors were fabricated with improved capacitance and cycle life. Activated carbon (AC) was synthesized from cabbage leaves as a low cost, biowaste-derived active electrode material. To improve mechanical flexibility and conductivity, we incorporate reduced graphene oxide sheets (RGO) and carbon quantum dots (CQDs) into the electrodes. It is shown that at the optimum AC-RGO-CQD composition, the capacitance of the solid-state supercapacitor is maximized while its scan rate dependence and bending stability are simultaneously improved. We envision that this approach offers significant potential for delivering efficient energy storage devices for consumer electronics.

5.1. Structural Characterization of Active Electrode Materials

5.1.1. Cabbage-derived Activated Carbon

N_2 adsorption-desorption measurements confirm the microporous structure of AC (Figure 4.5 (a)). According to IUPAC classification, AC exhibits a type I isotherm indicating the material has a microporous structure [169]. The steep N_2 uptake at low relative pressures indicates the formation of a large amount of micropores. Figure 4.5 (b) shows AC has a micropore-dominated pore-size distribution. The increase in N_2 uptake at high relative pressures reveal the presence of some mesoporosity which is also supported by the pore size distribution profile in Figure 4.5(b). The BET surface area of AC is found as 3038 m^2/g with 1.02 cm^3/g pore volume. Meanwhile, commercial activated carbon has a smaller BET surface area (408 m^2/g) and pore volume (0.4 cm^3/g).

The Raman spectrum of AC exhibits D- and G-peaks located at 1360 and 1570 cm^{-1} (Figure 4.5 (c)). These peaks were fit using the Lorentzian and Breit-Wigner-Fano functions for D- and G-peaks, respectively. The ratio of the intensities of the peaks (ID/IG) is obtained as 0.92. This is larger than the ID/IG ratio of commercial activated carbon,which is 0.4 (Figure A.2). This indicates that AC has a more defective structure. From an electrochemical perspective, the defect density plays a significant role in enhancing the overall capacitance performance. Moderate levels of defects in the carbon structure can disrupt the sp^2 lattice and create localized states that increase the density of states (DOS) at the Fermi level [170]. This, in turn, enhances quantum capacitance, which contributes to the total capacitance of the material [170, 171]. Defects act as active sites for ion adsorption, allowing for better ion accessibility and faster charge/discharge cycles. As a result, the higher ID/IG ratio in AC translates to improved conductivity and enhanced charge storage capability, directly impacting the performance of the supercapacitor.

Figure 4.5 (d) shows the full scale XPS spectra for AC that provide information about chemical composition and bond structure. This is in agreement with the higher C/O of AC as determined from XPS analysis ($\simeq 11$), compared to that of commercial activated carbon ($\simeq 9$). Lower amount of oxygen-containing functional groups facilitate ion penetration into electrode pores.

Oxygen-containing functional groups affect the surface chemical properties of carbon materials. In order to further explore the type and composition of oxygen functional groups on the surface of AC, the deconvoluted C1s and the O1s XPS spectra are presented in Figure 4.5. C1s peak is deconvoluted into four peaks (Figure 4.5(e) and (f)), i.e. C=C at 284.5 eV , C-C at 285.7 eV , C-O at 286.8 eV, C=O at 288.7 eV. The O1s spectra indicate that C=O components (mainly attributed to carboxyl or ester carbon) are the dominant functional groups on AC, while carboxylic functional groups (O=C-OH) take second place. In commercial AC, C=O and C-O groups account for most of the oxygen content, and the peak at 536.0 eV confirms N_2 is doped into the carbon structure (Figure A.2). Moderate levels of oxygen functionalities ($\simeq$

10), particularly C-O and C=O groups, can enhance the wettability of the material by the electrolyte, facilitating better ion transport and improving the interaction between the electrode and the electrolyte. This increases the effective surface area for charge storage and enhances the electrochemical performance. Moreover, oxygen-containing groups provide additional active sites for ion adsorption and contribute to faster ion diffusion through the porous structure. However, it is important to maintain a balance, as excessive oxygen functionalities could potentially block micropores or lead to pore wall collapse, reducing the specific surface area and overall capacitance. In our material, the moderate presence of these functionalities supports improved ion accessibility without compromising structural integrity, which contributes to the superior capacitance performance observed [172, 173].

5.1.2. Reduced Graphene Oxide

RGO depicts a typical type IV isotherm with a hysteresis loop (Figure 5.1 (a)), exhibiting a BET surface area of 324 m^2/g and a cumulative pore volume of 0.7 cm^3/g (Figure 5.1(b)). The open channels between the RGO sheets account for most of the BET surface area and pore volume. The increase of the N_2 adsorption at high relative pressures above 0.9 is associated with large interlamellar voids. The average pore diameter of RGO is calculated to be 11.6 nm, consistent with the formation of large interlamellar voids.

Based on Raman spectroscopy results, RGO exhibits the characteristic D- and G-peaks around 1332 and 1585 cm^{-1}, respectively. The D-peak represents the breathing mode of six-membered aromatic rings observed in the presence of defects that disrupt the aromatic domains, while the G-peak is due to the in-plane oscillations of sp^2 carbon bonds [174]. The D- and G-peaks were respectively fit to Lorentzian and Breit-Wigner-Fano functions. The ID/IG of RGO ($\simeq$ 1.10) depicts the defective nature of the material. This conclusion is in well agreement with the conclusions derived from XPS analysis. The C/O ratio of RGO is 8.04 suggesting that oxygen functionalities are removed from the material during reduction. The high resolution C1s XPS spectrum of

RGO shows the presence of oxygenated functional groups, although the peak intensities for these fitting components are small. The O1s spectra show an intense peak at at 533.1 eV attributed to C-O components, and smaller peaks corresponding to O=C-OH at 531.2 eV and C-OH at 533.5 eV.

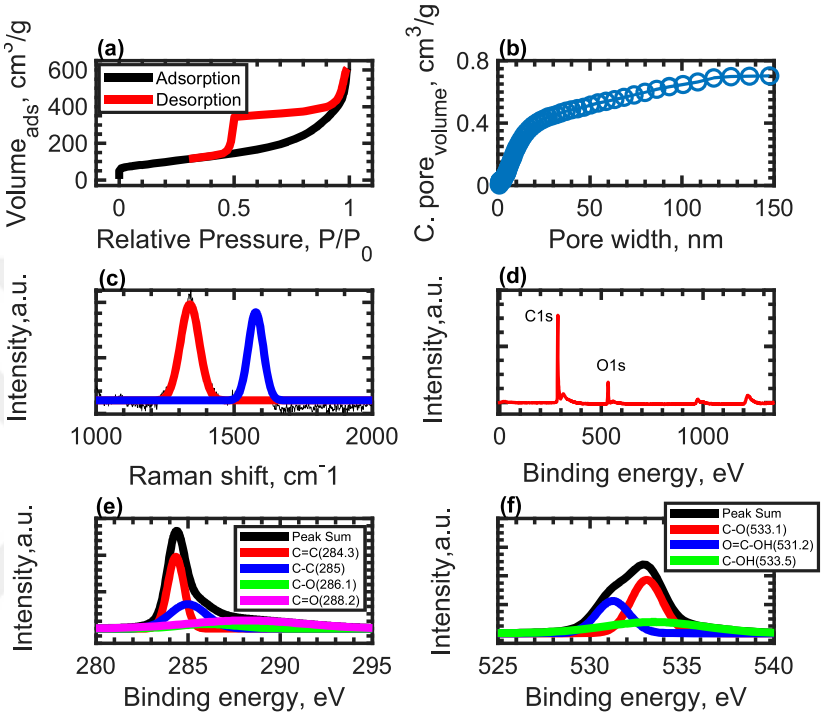

Figure 5.1. RGO a. N_2 ads/des isotherms, b. Pore size distribution, c. Raman spectra, fitting curves. Red line represents the Lorentzian fit to the D-peak and Blue line represents the BWF fit to the G-peak, d. The total XPS spectra, e. The XPS Deconvolution of C1s spectra and f. The XPS Deconvolution of O1s spectra.

5.1.3. Carbon Quantum Dots

The XPS spectrum of CQDs (Figure 5.2 (a)) reveal the presence of C, O and N atoms with a C/O ($\simeq$ 2.9). The existence of oxygen-containing functional groups improve the wettability of the electrodes by the electrolyte, hence facilitate ion transport inside the electrodes. C1s peak is deconvoluted into three peaks (Figure 5.2 (b)), i.e. C=C at 284.5 eV , C-O at 285.9 eV, C=O at 287.8 eV. The O1s fitting results reveal that C=O components are the dominant functional groups. Furthermore, the peaks at 399.69 eV and 402.5 eV confirm nitrogen is successfully doped into the CQD structure.

According to UV-Vis spectra, CQD shows a peak at 348 nm, probably resulting from n-π^* transition of oxygenated functional groups such as C=O, C-O and epoxy. From both XPS and UV-vis results, it is very clear that CQDs are decorated with surface oxygen-containing functional groups. The FTIR spectrum of CQD shows (Figure 5.2 (f)) broad peak around 2970 cm^{-1} which can be ascribed to C-H stretching. There is also a peak appearing in the spectra around 1651 cm^{-1} which can be ascribed to C=O stretching vibration while the bands around 1413 cm^{-1} and 1000 cm^{-1} are assigned to C=C and C-O vibrational stretch, respectively.

XPS and FTIR analyses of CQDs both indicate that the surface of CQDs were partially oxidized, which contributes to the hydrophilicity of CQDs. This is expected to improve wettability of AC and facilitate electrolyte adsorption. XPS analysis also reveals that in addition to carbon and oxygen-containing groups, CQDs contain the nitrogen heteroatom. Moreover, to elucidate the optical properties of CQD, the fluorescence behavior in DMF solution is explored. CQD fluorescence emission spectra is observed at various excitation wavelengths ranging from 250 to 430 nm. The strongest fluorescence appears in the synthesized CQDs with an increasing emission peak in 350-400 nm. Under the maximum excitation wavelength of 374 nm, the fluorescence spectra showing a maximum emission located at 441 nm (Figure 5.2 (g)) is observed.

5.1.4. Composite Materials

Composite materials prepared by incorporating RGO and CQD into AC are also characterized. Figure 5.3 (a) shows the XRD patterns of AC and composite materials in the 2θ ranges of 10-80°. The weak peaks around 24 and 43° in AC reveal the tendency to form graphitic phases from the amorphous structure of AC [175]. The AC-15RGO has two broad peaks at 23.3 and 43.4°.

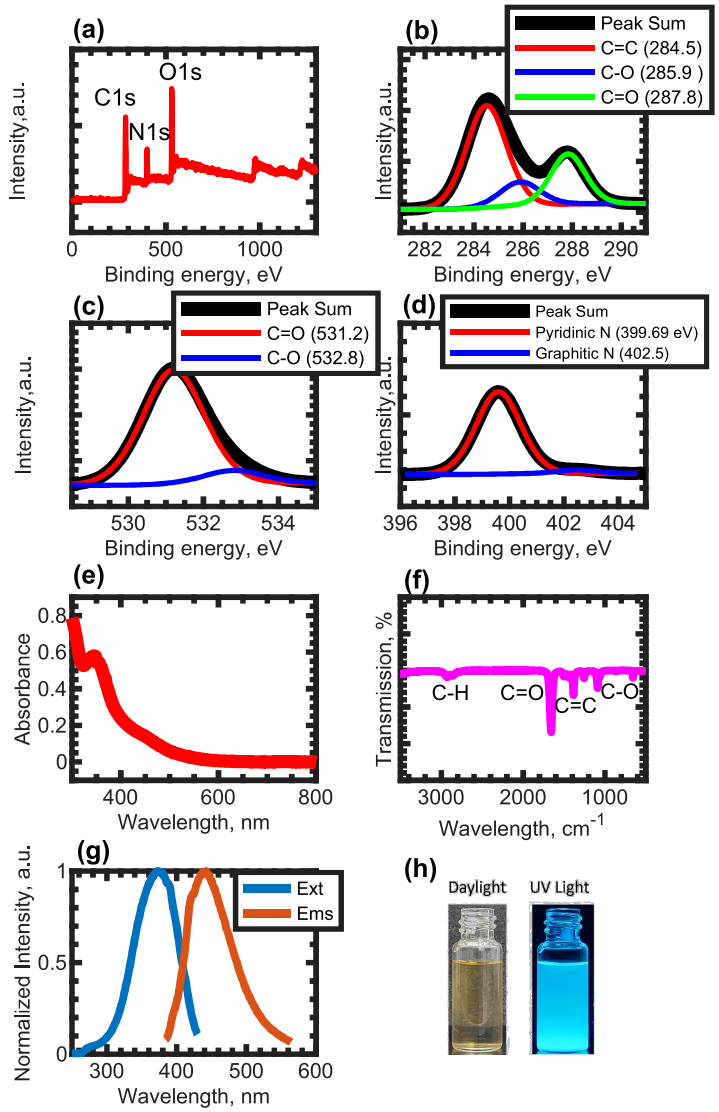

Figure 5.2. CQD a. The total XPS spectra, b. The XPS Deconvolution of C1s spectra, c. The XPS Deconvolution of O1s spectra, d. The XPS Deconvolution of N1s spectra, e. UV-Vis spectroscopy, f. FTIR spectrum, g. Fluorescence excitation and emission spectra and h. Photos of CQD solution taken under daylight and UV light.

This is a typical pattern for carbon having a turbostratic structure. The turbostratic model suggests that the building blocks of carbon samples are close to graphitic-like structure, which stack in a roughly parallel way within the structure with some random orientations. This result indicates that RGO, which has two wide peaks around 24.7 and 43.3° (Figure A.3), is successfully incorporated into AC. On the other hand, AC-CQD sample shows two broad peaks at 22 and 43.4°. Those peaks

come from the graphitic nature of CQD. AC-RGO-CQD has two wide peaks at 22.7 and 43.2°, implying that RGO and CQD are successfully incorporated into activated carbon.

Based on Raman spectroscopy results, composite materials show characteristic D- and G-peaks around 1330 and 1580 cm^{-1}, respectively. The D- and G-peaks are respectively fit to Lorentzian and Breit-Wigner-Fano functions. The ID/IG of AC-10CQD, AC-15RGO and AC-RGO-CQD are found as 1.01, 1.2 and 1.25, respectively. The results depict the successful incorporation of additives into activated carbon due to improvement in ID/IG as compared to AC (0.92). The increase in ID/IG indicates defective nature of the composite material. The increase in defect sites results from the reduction in sp^2 lattice size leading to an increase in sp^2 domains which is typically assocaiated with an increase in electrical conductivity [176, 177].

Using FTIR, surface functional groups in AC, RGO, CQD and its composites are investigated. AC and RGO has transmission bands at 2163, 2024 and 1967 cm^{-1} , indicating the presence of C=C=C and C=C (alkyne group) stretching. The absorption bands at 1626 cm^{-1} (AC) and 1587 cm^{-1} (RGO) are attributable to carboxylic C=O stretching mode. The spectra of composite materials show similar peaks in the range of 3500–1000 cm^{-1}.

5.1.5. The Gel Electrolytes

The gel polymer electrolyte films were prepared by solution-casting as described in section 3.4. The gel electrolyte was based on PVA-KOH in water as solvent, which is the most common gel electrolyte in literature.

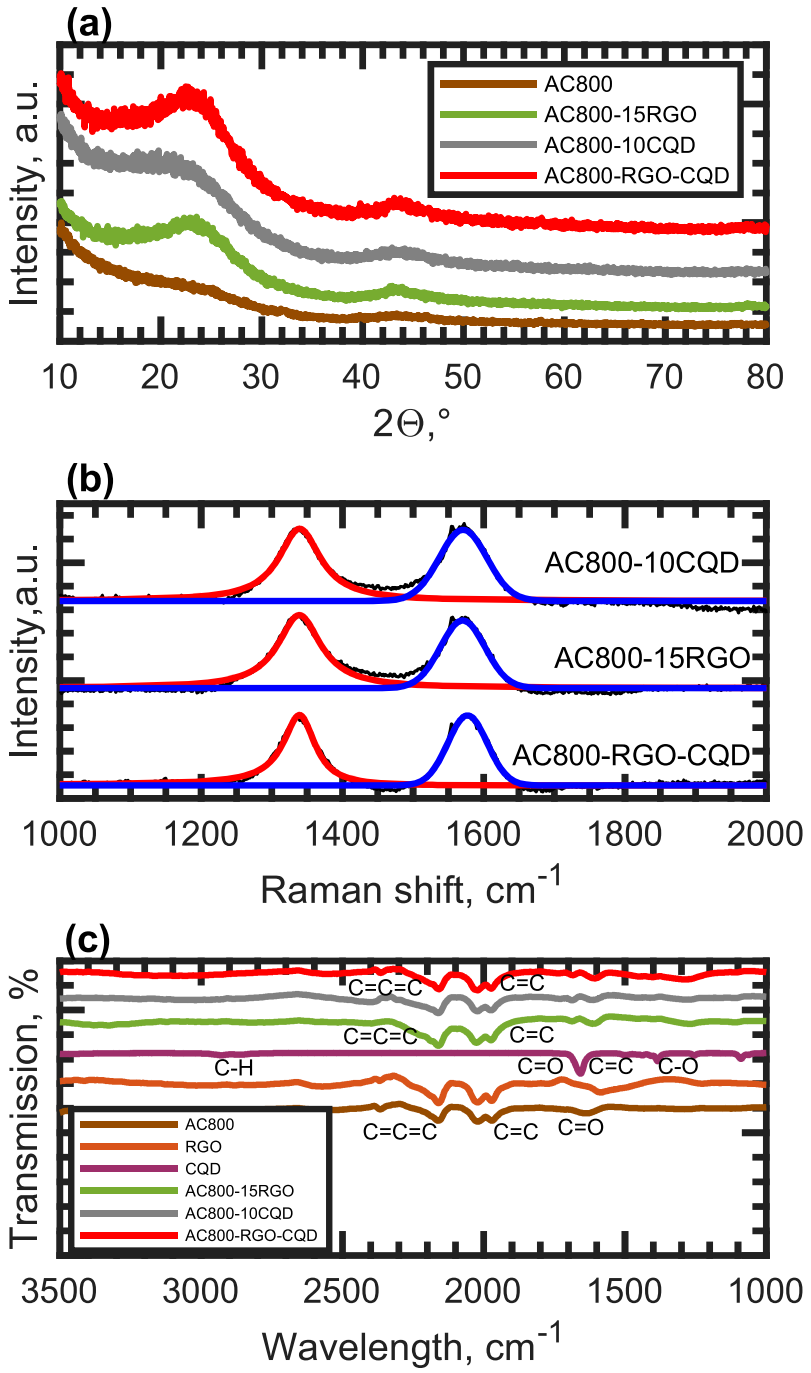

Figure 5.3. Structural characterizations of composite materials a. XRD spectrum, b.Raman spectra, fitting curves. Red line represents the Lorentzian fit to the D-peak and Blue line represents the BWF fit to the G-peak and c. FTIR spectrum.

5.2. Electrochemical Characterization

AC suffers from the lack of interconnectivity within its carbon structure which causes increased resistance upon assembly into electrodes, and the presence of inaccessible pores associated with complications in ion penetration. Also, AC has a brittle structure that precludes its use in applications that require flexibility. Electrochemical measurements of AC with increasing amounts of CQD loading were performed to improve interconnectivity of activated carbon particles. Figure 5.4 (a) and (b) shows adding 5 wt.% CQD does not have a significant impact on capacitance. Meanwhile, when 10 wt.% CQD is added, specific capacitance increases from 99 to 110 mF/cm^2. Not only capacitance but also cycling stability under 0° were improved by incorporating CQDs into AC. One plausible explanation for the enhanced capacitance at higher CQD concentrations is that CQDs may occupy the defects within the carbon framework, thereby creating additional active sites for charge storage [69, 178, 179]. It is hypothesized that the high charge density of CQDs leads to an increased accumulation of counterions within the pores of activated carbon, thus facilitating accelerated charge transfer within the carbon framework. Additionally, due to the differing electronegativities of carbon and nitrogen, doping with CQDs introduces unique electronic transition properties that could improve charging kinetics [180].

Further, CQDs are known to possess functional groups like hydroxyl, carboxyl, and amine groups. When integrated into activated carbon, these groups can be further introduced to the surface of the carbon material, improving its wettability, providing additional active sites for charge storage, and enhancing interactions with the electrolyte in supercapacitors. The presence of these groups can lead to improved electrolyte adsorption and ion mobility (Figure 5.2 (b),(c),(d), and (f)). The carbon backbone of CQDs is generally highly conductive, and when incorporated into the activated carbon structure, the overall conductivity of the composite material can be enhanced. This is particularly important for electrochemical performance because improved conductivity facilitates faster electron transfer, reducing internal resistance and improving charge/discharge rates.

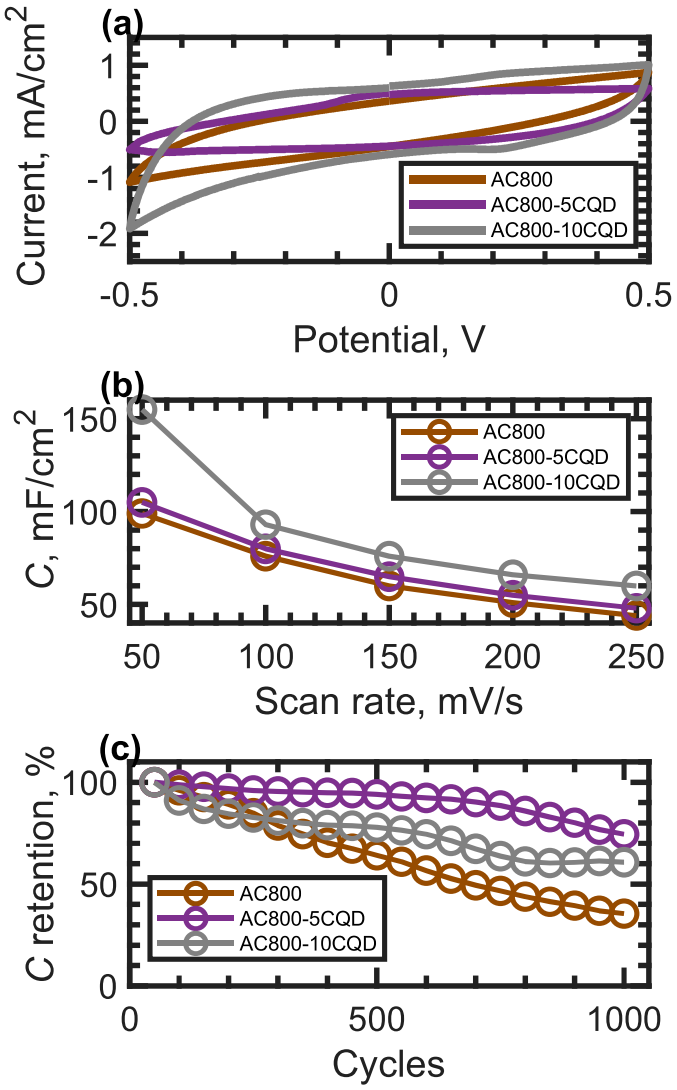

Figure 5.4. Electrochemical characterizations of AC, AC-5CQD and AC-10CQD in 2-electrode set-up a. Cyclic voltammogram at 50 mV/s, b. Capacitance vs. scan rate, c. Capacitance retention at 150 mV/s over 1000 cycles under 0°.

CQDs can also affect the meso- and microporosity of activated carbon. The introduction of CQDs into the activated carbon matrix can slightly alter the pore size distribution and overall porosity (Figure A.4). This modification can improve ion accessibility during charge/discharge cycles, which enhances the efficiency of charge storage in electrochemical devices. Also, the increased surface area can provide more sites for energy storage. The modification of the surface structure and the increased conductivity provided by the CQDs can facilitate faster ion diffusion through the electrode

material. This leads to better performance at high charge/discharge rates, which is essential for applications requiring quick energy delivery or uptake. Enhanced electron conductivity due to the presence of CQDs helps reduce the overall internal resistance of the material. This allows for faster electron transfer between the activated carbon and the current collector, enabling high power output during rapid charging and discharging cycles. The incorporation of CQDs can enhance the overall stability of the activated carbon. The functionalization of the carbon surface by CQDs helps bind the material structure together, potentially reducing the effects of electrode material degradation during repeated charge/discharge cycles. The CQDs can also help prevent the dissolution or detachment of active species from the surface, which contributes to better long-term stability. The small size and structural stability of CQDs can help improve the mechanical stability of the composite material. The increased stability of the carbon framework can prevent cracking or collapse of the porous structure during repeated cycling, which is a common issue with pure activated carbon. The improved electrochemical performance of activated carbon upon the incorporation of CQDs can be attributed to several mechanisms. The presence of functional groups on CQDs (such as hydroxyl and carboxyl) can increase the hydrophilicity of the activated carbon surface. This can improve the interaction between the electrode material and the electrolyte, leading to enhanced ion diffusion and increased capacitance. The conductivity of the CQDs and the increased connectivity between CQDs and the activated carbon framework can facilitate more efficient electron transfer. The reduction in electron resistance allows for faster charge/discharge cycles and improves the overall rate capability of the composite material. The smaller size of CQDs and their distribution within the activated carbon structure can enhance ion accessibility within the porous network of the material. The improved pore structure allows for better ion penetration and more efficient energy storage.

Although CQD incorporation into AC improved capacitance, scan rate dependence and stability simultaneously, the obtained results are not competitive with literature. Therefore, RGO was incorporated to AC to provide a conductive and stretchable network. As depicted in Figure 5.5 (a) and (b), electrodes comprising AC/RGO ma-

terial demonstrates an increase in capacitance from 99 mF/cm^2 to 160 mF/cm^2 and 130 mF/cm^2 with RGO contents of 15 wt.% and 20 wt.%, respectively, under 0° bending. This enhancement can be attributed to the oxygen-containing surface functional groups present in RGO, which improve the wettability of the electrodes by the electrolyte, consequently leading to higher capacitances. Moreover, RGO incorporation not only affects the specific capacitance but also alters the scan rate dependence. For instance, while the capacitance retention increases from 50 mV/s to 250 mV/s by 40 % for AC, it reaches 63 % for AC-15RGO. This improved rate capability indicates the fast charging properties of the AC-RGO composite electrode.

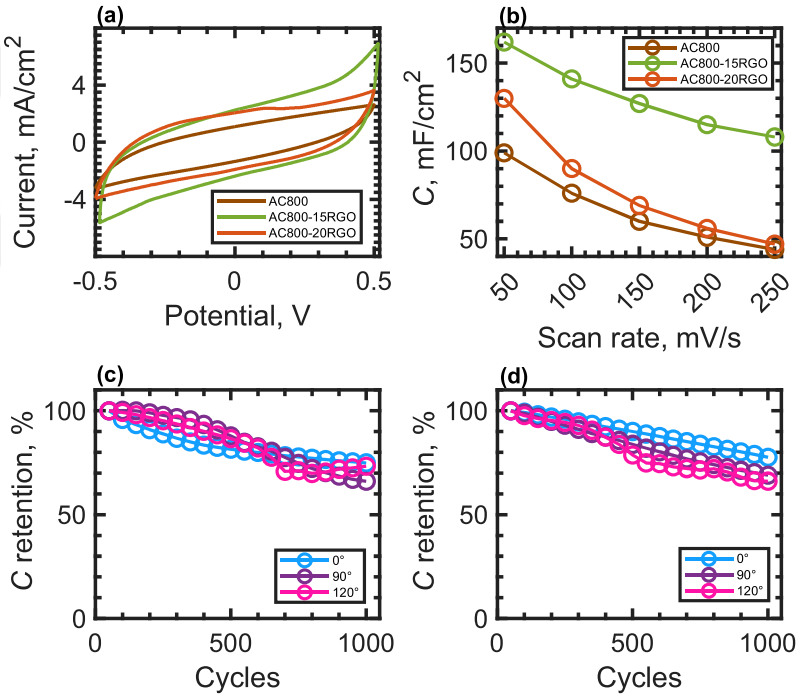

Figure 5.5. Electrochemical characterizations of AC, AC-15RGO and AC-20RGO a. CV at 50 mV/s, b. Capacitance vs. scan rate, c. Capacitance retention over 1000 cycles of AC-15RGO under different bending angles and d. Capacitance retention over 1000 cycles of AC-20RGO under different bending angles.

One of the most significant contributions of RGO to activated carbon is the enhancement of electrical conductivity. Activated carbon, while highly porous and surface area-rich, can sometimes have low intrinsic conductivity, which limits its performance in fast-charging applications like supercapacitors. RGO, on the other hand, is an ex-

cellent conductor of electricity due to its sp^2 hybridized carbon network. When RGO is combined with activated carbon, it forms conductive pathways that facilitate faster electron transfer, reducing the internal resistance of the material. This is crucial for improving the rate capability and overall electrochemical performance. The combination of AC and RGO provides a hybrid system in which the porous nature of activated carbon allows for high surface area and ion storage, while RGO improves the electron transfer between the activated carbon pores and the external circuit. This enhanced conductivity leads to a decrease in charge/discharge time and allows for more efficient energy storage. The introduction of RGO into the activated carbon matrix may alter the pore size distribution. RGO, with its layered and planar structure, may help to refine the mesopores and micropores of activated carbon (Figure A.4), improving ion accessibility during charge and discharge processes. This leads to a more efficient ion storage mechanism, improving the overall capacitance. The reduced graphene oxide sheets can also increase the surface area available for charge storage. In some cases, RGO can effectively fill voids in the activated carbon matrix or create additional surface area for interaction with the electrolyte, thereby increasing the number of active sites available for ion adsorption. The oxygenated functional groups on RGO can interact with the surface of activated carbon. These groups not only enhance the surface wettability of the composite material, which is beneficial for electrolyte-ion interaction but also provide additional sites for ion adsorption. The presence of oxygen-containing functional groups also facilitates the dispersion of RGO within the activated carbon matrix, preventing aggregation of RGO sheets and improving the overall stability and performance of the composite. Moreover, activated carbon predominantly stores energy through EDLC, which relies on the electrostatic attraction between the surface and electrolyte ions. RGO, with its high conductivity, ensures efficient electron flow during the charging and discharging process, enhancing the overall EDLC performance. RGO, due to its inherent mechanical strength, can help prevent the physical degradation of the activated carbon during repeated cycling. This is especially beneficial when dealing with the structural collapse or loss of surface area that can occur in pure activated carbon electrodes after many cycles. RGO can also act as a binder between activated carbon particles, preventing the aggregation or stacking of the carbon

sheets, which can lead to a loss of surface area and decreased performance over time. The strong interaction between RGO and activated carbon ensures that the composite material retains its structural integrity during extensive cycling, leading to improved long-term stability. Beyond this, RGO can help create stretchable composite materials. This is important for applications that require energy storage devices that can not only bend but also stretch without compromising performance. The RGO sheets, which are inherently flexible, contribute to the formation of a network that allows for stretching without breaking the conductive pathways. As a result, the composite retains its high conductivity and electrochemical performance even when stretched or deformed.

To test the flexibility of the device, we bent the device to different angles (90 and 120°) and measured the capacitance retention at a scan rate of 150 mV/s over 1000 cycles. Figure 5.5 (c) and (d) show that cycling stability of AC-15RGO is 75 % and that of AC-20RGO is 66 % under 120° bending.

Considering that the composition with 10 wt. % CQD and 15 wt. % RGO exhibits superior performance for flexible supercapacitor applications, the remaining part of this work focused on using the AC-RGO-CQD (10 wt. % CQD, 15 wt. % RGO, and 55 wt. % AC) composite for solid-state supercapacitor design. This composition was selected to maximize capacitance and flexibility by leveraging the synergistic effects of CQDs and RGO. As illustrated in Figure 5.6 (a) and (b), the AC-15RGO-10CQD composite achieves a high areal capacitance of 320 mF/cm^2 at 50 mV/s, significantly surpassing that of plain AC (99 mF/cm^2). Additionally, the composite demonstrates enhanced capacitance retention, maintaining 60 % of its initial capacitance as the scan rate increases from 50 mV/s to 250 mV/s, compared to only 40 % retention for plain AC.

These improvements in capacitance and retention can be attributed to the unique pore structure of AC-15RGO-10CQD, as detailed in Figure A.4 (a)-(c). The nitrogen adsorption/desorption isotherms and PSD data for plain AC (Figure 4.4 (a) and (b)) reveal a predominantly microporous structure, with the isotherm exhibiting a classic Type I shape. This structure provides a high surface area for ion adsorption, which

is beneficial for capacitance. However, the lack of mesopores in plain AC limits ion transport, as ions must navigate through narrow micropores, which can slow down charge/discharge rates under high current conditions. In contrast, the AC-15RGO-10CQD composite shows a mixed Type I and Type IV isotherm (Figure A.4 (b)), indicating the presence of both micropores and mesopores. This is further supported by the PSD data (Figure A.4 (c)), which shows a broader pore size distribution for AC-15RGO-10CQD, with both micropores (<2 nm) and mesopores (2–6 nm) present. The mesopores, introduced by the addition of RGO and CQDs, act as transport channels that facilitate rapid ion diffusion, allowing ions to access the inner micropores more efficiently.

This hierarchical pore structure is advantageous for EDLC applications, as it balances high capacitance (from micropores) with enhanced rate capability (enabled by mesopores). The observed degradation at higher bending angles can be attributed to the structural properties of both the electrode and the electrolyte. Electrodes with high specific surface areas, particularly those dominated by micropores, are more susceptible to clogging over prolonged cycling. In contrast, the AC-15RGO-10CQD composite benefits from a hierarchical micro-mesoporous structure that mitigates clogging by providing mesopores as transport channels for ions. This structure helps reduce the internal resistance, improving ion transport and minimizing degradation under mechanical stress.

Additionally, RGO acts as a structural reinforcement, preventing the collapse of the carbon framework during bending and repeated cycling. This structural integrity is crucial for flexible applications, as it allows the composite to maintain high capacitance retention even under varied bending conditions. The AC-15RGO-10CQD composite, with its reinforced structure and balanced pore architecture, effectively addresses these challenges, making it suitable for high-performance flexible EDLC applications.

In summary, the AC-15RGO-10CQD composite, with its balanced micro-mesoporous structure and reinforced stability from RGO, outperforms plain AC by enabling faster ion transport, maintaining structural integrity under bending, and achieving higher areal capacitance and rate capability. These features make AC-15RGO-10CQD an ideal material for flexible EDLC applications, where both high capacitance and me-

chanical flexibility are essential.

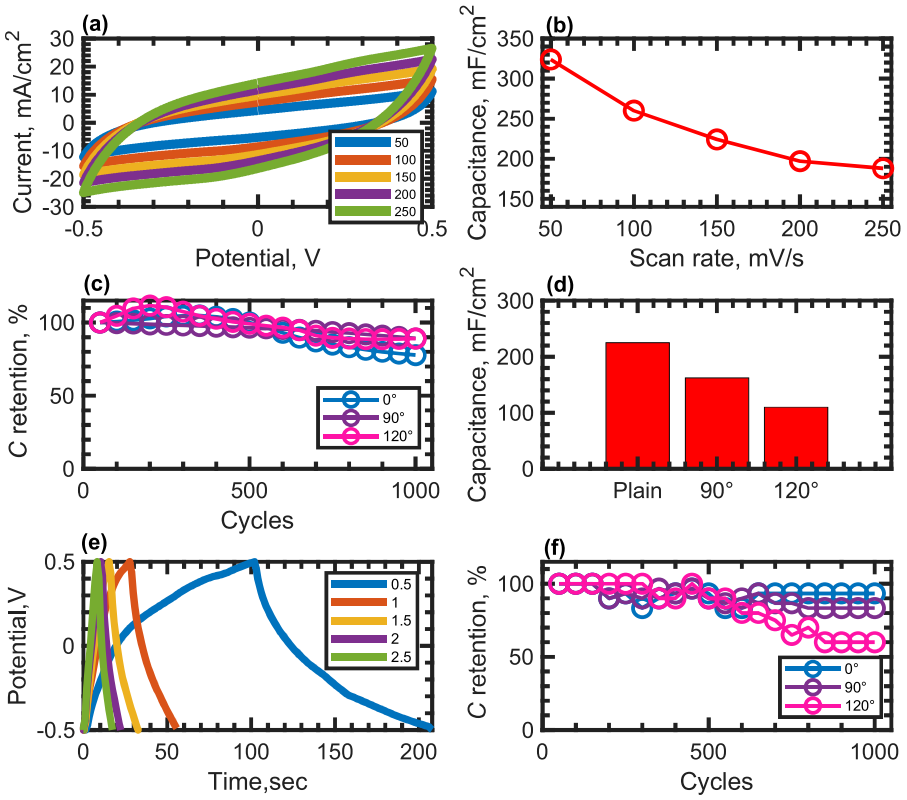

Figure 5.6. Electrochemical characterizations of AC-15RGO-10CQD a. CV at different scan rates, b. Capacitance vs. scan rate, c. Capacitance retention over 1000 cycles, d. Maximum attainable capacitance during bending, e. GCD at different current densities and f. Capacitance retention at over 1000 cycles.

The galvanostatic charge-discharge (GCD) curves for AC-15RGO-10CQD show a nearly symmetrical triangle shape, which implies the ideal capacitive behavior of the sample. The voltammograms display a quasi-rectangular shape with nearly symmetrical cathodic and anodic sweeps, indicating ideal capacitive behavior. This characteristic response is typical of EDLC materials, reflecting efficient ion adsorption and desorption processes at the electrode/electrolyte interface. The device has a specific areal capacitance of 285 mF/cm^2 at a current density of 0.5 A/g (Figure 5.6 (e)). As shown in Figure 5.6(f), the solid-state supercapacitor retains more than 60 % of its initial capacitance after 1000 cycles at 1.5 A/g under different bending angles. The simultaneous improvement in capacitance and bending properties is attributable to the

synergistic effect of accelerated charge transfer facilitated by CQDs and stretchable network provided by RGO.

Energy density was calculated as in

$$E = \frac{1}{2}CV^2. \tag{5.1}$$

Power density was calculated as in

$$P = \frac{E}{\Delta(t)}, \tag{5.2}$$

where C is capacitance, V is potential window and Δt is the discharging time. The energy density and power density range for activated carbon based flexible supercapacitors are between 10-50 Wh/kg and 500-10000 W/kg, respectively as can be seen by Figure A.5 (a). This indicates that the optimum composition of AC-RGO-CQD is competitive with literature.

Table A.1 presents a comparative analysis of the current study with existing research on carbon-based flexible solid-state supercapacitors. This targeted analysis focuses specifically on carbon-based electrodes and solid-state electrolytes, allowing for a precise evaluation of performance metrics relevant to these materials. The development of the AC-RGO-CQD composite demonstrates a notable improvement, showcasing competitive capacitance and enhanced cycling stability compared to previously reported carbon-based supercapacitors. The maximum attainable capacitance of the AC-RGO-CQD composite is superior to most results documented in the literature (see Figure A.4). Additionally, the capacitance retention of this composite under bending conditions aligns with the findings reported by other researchers (Table A.1). The high capacitance of AC-RGO-CQD is attributable to the improved ion accessibility of the material, facilitated by the incorporation of CQDs and the structural reinforcement provided by RGO. These features contribute to sustained charge-discharge performance over multiple cycles with minimal performance loss.

6. ENHANCED FLEXIBLE SUPERCAPACITORS WITH B-DOPED RGO ELECTRODES AND CARBON QUANTUM DOT GEL ELECTROLYTES

Boron doping introduces boron atoms into the graphene lattice, replacing carbon atoms. This substitution can lead to lattice distortions due to the size mismatch between boron (atomic radius:87 pm) and carbon atoms (atomic radius:67 pm), potentially affecting the material's mechanical properties. However, the strong boron-carbon bonds can help maintain structural integrity, and the specific impact on mechanical properties depends on factors such as doping concentration and distribution. Incorporating boron-doped reduced graphene oxide (BRGO) into an activated carbon (AC) matrix can enhance the composite's mechanical stability. The interaction between BRGO sheets and the AC matrix facilitates stress distribution during mechanical loading, reducing the likelihood of fracture. Additionally, boron doping can improve the adhesion between graphene sheets and the matrix, further enhancing mechanical stability. Further, carbon quantum dots were chosen to be added to the electrolyte due to their unique properties. Their incorporation can increase the overall performance of the supercapacitor by facilitating better ion transport, improving the interface between the electrolyte and electrode leading to better charge transfer, contributing to the stability of the device. CQDS with exceptional conducting properties arise from the quantum confinement and edge effect, which is related to the motion of charge carriers (like electrons) in such small structures. The motion of charges becomes restricted in one or more dimensions, leading to discrete energy levels, which alters the electronic properties such as increased conductivity. In this chapter, boron doped reduced graphene oxide incorporated into AC structure as electrode material along with CQD added gel electrolyte was used for the application of flexible supercapacitors.

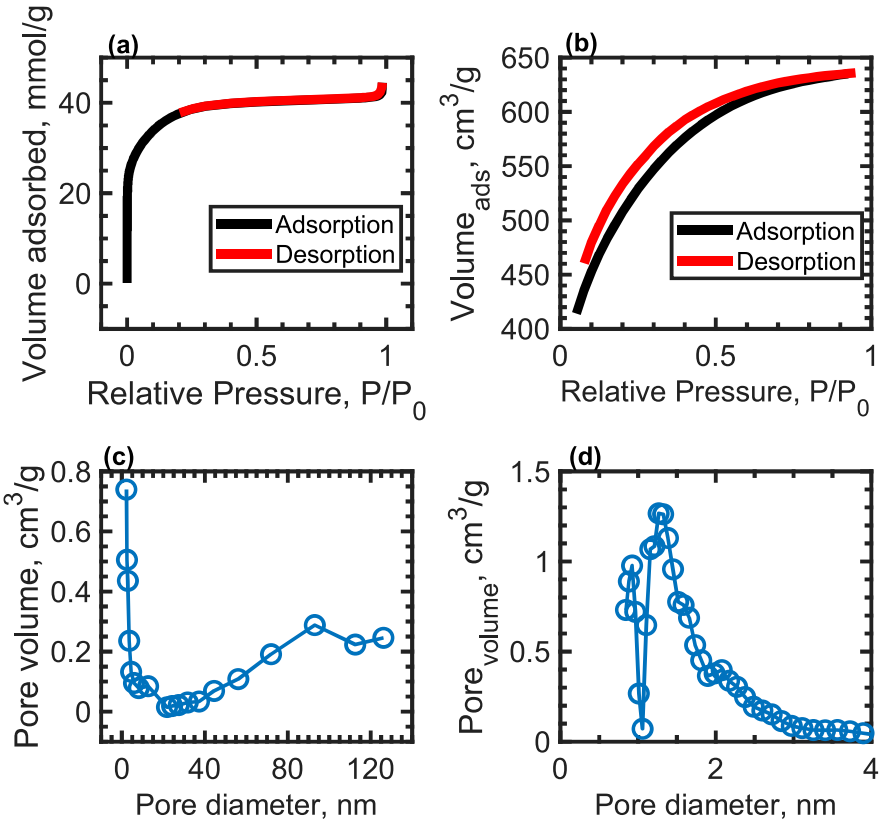

Figure 6.1. Pore structure analysis of AC and AC-10BRGO a. N_2 ads/des isotherms of AC, b. N_2 adsorption/desorption isotherms of AC-10BRGO, c. Pore size distribution of AC, and d. Pore size distribution of AC-10BRGO.

6.1. Structural Characterization of Active Electrode and Electrolyte Materials

6.1.1. Cabbage-derived Activated Carbon/Boron Doped Reduced Graphene Oxide

The structural properties of the activated carbon (AC) and AC-10BRGO composite were characterized using nitrogen (N_2) adsorption-desorption isotherms, pore size distribution analysis, X-ray photoelectron spectroscopy (XPS), Raman spectroscopy, Fourier-transform infrared (FTIR) spectroscopy, and X-ray diffraction (XRD).

Figure 6.1 (a) and (b) display the N_2 adsorption-desorption isotherms for AC and AC-10BRGO, respectively. The AC exhibits a type I isotherm characteristic of a microporous structure dominated by micropores, as per the IUPAC classification. In contrast, AC-10BRGO demonstrates a hybrid type I-IV isotherm, indicating a bimodal micro/mesoporous pore structure. The nitrogen is adsorbed by the AC-10BRGO, mainly, at low relative pressures which is typical of microporous structure. At higher relative pressures, with continued adsorption, mesoporosity is present in the structure of AC-10BRGO. The pore size distribution curves, shown in Figure 6.1 (c) and (d) for AC and AC-10BRGO respectively, further elucidate these findings. The specific surface area and cumulative pore volume of AC are measured as 3038 m^2/g and 1.02 cm^3/g, respectively, while AC-10BRGO possesses a smaller BET surface area (1724 m^2/g) and cumulative pore volume (0.98 cm^3/g).

The Raman spectrum of AC reveals D- and G-peaks centered at 1360 and 1570 cm^{-1}, respectively (Figure 4.5 (c)). These peaks are fit using the Lorentzian and Breit-Wigner-Fano functions for D- and G-peaks, respectively. The D-band is attributed to the defect of highly ordered carbonaceous materials while the G-band is attributed to C=C strecthing vibrations. The peak intensity ratio of the D-band and the G-band indicates the carbon-containing defects. The ratio of the intensities of the peaks (ID/IG) is obtained as 0.92, indicating a defective nature of AC.

XPS spectra of AC, depicted in Figure 4.5 (d), depict a C/O ratio of $\simeq 11$. To further investigate the oxygen functional groups on the surface of AC, the deconvoluted C1s and O1s XPS spectra are presented in Figure 4.5 (e) and (f), respectively. The C1s peak is deconvoluted into four peaks, indicating various carbon functionalities. Meanwhile, the O1s spectra suggest that C=O components dominate the surface functionalities of AC, followed by carboxylic functional groups (O=C-OH). The presence of N_2 doping into the carbon structure is confirmed by the peak at 536.0 eV.

The composite material, prepared by incorporating BRGO into AC, was also characterized by Raman, XPS, and FTIR. Raman spectra of RGO and BRGO show

that the ratio of the D-band to G-band (ID/IG) in the Raman spectra of the RGO samples is 1.1 and that of BRGO is 2.2 (Figure A.6). ID/IG ratio of 1.1 indicates a relatively moderate defect density in RGO. This suggests that a significant amount of oxygenated functional groups have been removed and some of the graphitic structure have been restored. The moderate ratio indicates that while the material is not pristine graphene, it has good potential for conductivity. On the other hand, ID/IG ratio for BRGO (2.2) indicates that BRGO has a significantly higher defect density compared to RGO. This may be attributed to additional defects or functional group modifications introduced into the graphene lattice during the synthesis of BRGO. Specifically, some reduction processes can lead to over-reduction, disrupting the graphene network and increasing disorder. The high level of disorder in the material creates defects that can act as active sites, enhancing electrochemical performance. Furthermore, the presence of additional oxygenated groups in the BRGO structure could improve electrolyte wettability, contributing to its overall performance. This relatively high ID/IG ratio is consistent with the introduction of defects and functional groups, which is typically expected in the presence of dopants, such as boron. The ID/IG ratio of AC-10BRGO, determined from Raman spectroscopy, was found to be 3, much higher than that of AC (0.92), suggesting successful boron doping on the reduced graphene oxide sheet. This increase in the ID/IG ratio indicates the presence of defects, potentially acting as active sites, may have enhanced capacitance.

In order to further explore the type and composition of functional groups on the surface of AC-10BRGO, the deconvoluted C1s and the O1s XPS spectra are presented in Figure 6.2 (c) and (d). C1s peak is deconvoluted into three peaks, i.e. C=C at 284.5 eV, C-O at 285.9 eV, and C=O at 288.6 eV. The O1s peak is deconvoluted into three peaks, i.e. C=O at 531.6 eV, C-O at 533.2 eV and O-C=O at 535.8 eV, indicating oxygen surface functionalities that may improve the wettability of the electrodes. XPS analysis also confirms the presence of boron in the AC-10BRGO structure. A peak found at 192.3 eV is a characteristic of B-O bond in B_2O_3, which proves boron incorporation into AC structure.

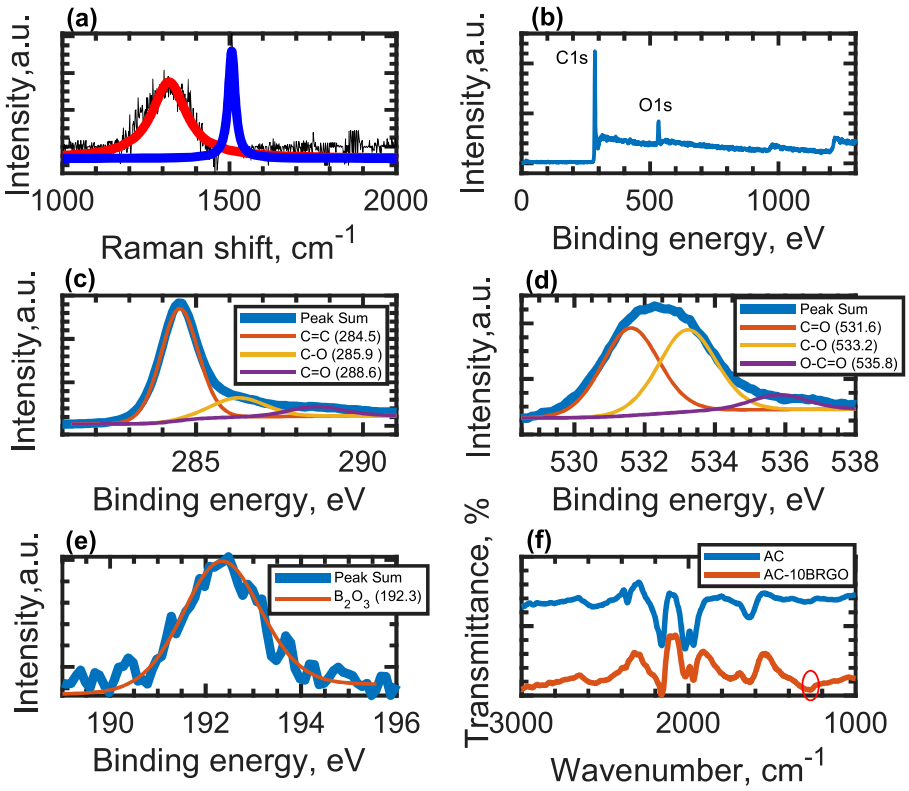

Figure 6.2. a.Raman spectroscopy of AC-10BRGO. Red line represents the Lorentzian fit to the D-peak and blue line represents the BWF fit to the G-peak, b.The total XPS spectra, c. Deconvoluted C1s XPS Spectra, d. Deconvoluted O1s XPS Spectra , e. Deconvoluted B1s XPS Spectra, and f. FTIR analysis.

Additionally, XRD patterns of AC and AC-10BRGO (Figure A.7) display peaks at 24.5° and 42.8°, with AC-10BRGO showing more intense peaks, confirming successful boron doping. These findings are consistent with the results obtained from Raman, XPS, and FTIR analyses.

Scanning electron microscopy (SEM) was used to gather information on the morphology of the powdered activated carbon and activated carbon-boron doped reduced graphene oxide (Figure A.8). The image (Figure A.8 (a)) shows irregularly shaped particles with rough and porous surfaces, characteristic of activated carbon. The particle size distribution from Figure 6.1 (c) appears heterogeneous, with some larger and smaller aggregates. The porous structure suggests a high surface area (Figure 4.5 (b)). The composite (Figure A.8 (b)) exhibits a layered and sheet-like morphology, typical of

reduced graphene oxide (RGO). The boron doping may have caused defect formation and wrinkling, leading to the observed folded and stacked layers. The layers appear to be interconnected, which can enhance electrical conductivity and ion transport pathways. AC is not distinctly visible as separate particles but the layered morphology of the BRGO likely encapsulates or intercalates the AC particles. This can occur during the synthesis process, where AC becomes embedded in or coated by the BRGO sheets. AC may contribute to the overall roughness or slight irregularities seen in the BRGO layers, as it provides a porous and textured substrate for the graphene sheets to anchor onto. While the BRGO layers dominate the visual morphology, AC likely maintains its porous structure within the composite as depicted by Figure 6.1 (c) and (d). These pores might not be directly visible due to the overlapping graphene layers but still contribute to the composite's overall surface area and ion accessibility. In this material, AC could serve as a structural backbone, providing mechanical stability to the composite. The layered BRGO sheets alone might be prone to agglomeration or collapse, but the dispersed AC particles may help maintain separation between layers and improve the structural integrity of the composite. While AC is not really visible, the wrinkles, folds, and roughness in the BRGO layers could be influenced by the underlying AC particles, indicating a potential interaction between the two materials. This interaction could also enhance the composite's conductivity and ion transport properties.

6.1.2. The Gel Electrolytes

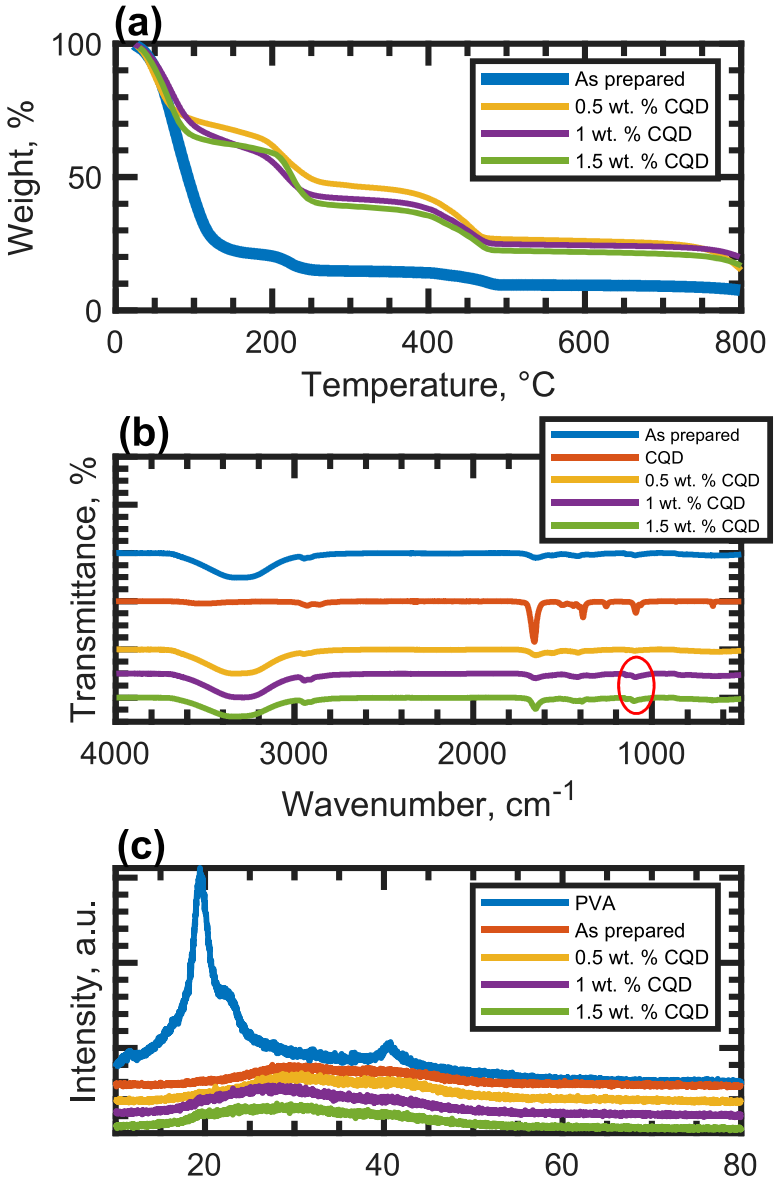

Figure 6.3. Structural characterizations of solo gel-electrolytes a. TGA curves, b. FTIR spectrum and c. XRD spectrum.

The thermal stability of the gel electrolytes was evaluated through thermal-gravimetric analyses (TGA), and the obtained TGA curves are depicted in Figure 6.3 (a). For the gel electrolytes, namely PVA-KOH and PVA-KOH-CQD, the initial mass loss occurs around 105 °C. A subsequent weight loss is observed at 211 °C, attributed to the elimination of OH groups and side chains. A third weight loss is noted around 485 °C, corresponding to the breaking of the PVA backbone [181]. Notably,

complete decomposition of PVA-KOH is observed at 800 °C; however, the addition of CQDs enhances thermal stability, with 20 % of the 1 wt. % CQD-added gel electrolyte remaining at 800 °C.

FTIR spectra were obtained for CQD, as well as as- prepared and CQD-added gel electrolyte samples. The presence of bands at 3330 and 2900 cm^{-1} is attributed to O-H stretching and bending, and CH_2 asymmetric stretching, respectively [181]. Additionally, bands at 1650 and 1100 cm^{-1} (as indicated by the red circle in Figure 6.3 (b)) correspond to C=O and C-O stretching, respectively, indicating the incorporation of CQDs into the gel electrolyte.

XRD patterns of pure PVA, as-prepared and CQD-added gel electrolyte films are illustrated in Figure 6.3 (c). The XRD spectrum of PVA exhibits a peak at 20°, indicative of a semi-crystalline structure [182]. However, in the prepared gel electrolyte, addition of KOH to PVA results in an amorphous structure. Upon incorporation of CQDs, a broad peak is observed in the range of 20-40°, suggesting an increase in the amorphous domain of the material [183]. Although the mechanism of ion transportation in gel electrolytes remains unclear, it is speculated that polymer chain motion exists within the amorphous structure [181, 183].

6.2. Electrochemical Characterization

6.2.1. Performance of Cabbage-derived Activated Carbon/BRGO Composites

Cyclic voltammetry were conducted for varying concentrations of B-doped RGO (AC-5BRGO, AC-10BRGO, AC-15BRGO) using 30 % v/v ACN during electrolyte preparation. Rational design of the layered structure of BRGO in AC can prevent the restacking of graphene sheets, enhancing the usage of surface area and establish effective ion transport channels [184]. The resulting cyclic voltammograms are presented in Figure 6.4 (a)-(d). Capacitance was calculated from equation 2.7.

The electrochemical measurements conducted at various boron concentrations (AC-5BRGO, AC-10BRGO, AC-15BRGO) provide insights into the performance of the electrodes. Figure 6.4 (a)-(d) depict the cyclic voltammograms of the samples at scan rates ranging from 50 to 500 mV/s within a 1.4 V potential window, demonstrating their electrochemical stability. Furthermore, Figure 6.4 (e) presents the specific capacitance as a function of scan rate for each boron concentration. The optimal boron concentration is determined to be 10 wt. %, resulting in an areal capacitance of 140 mF/cm^2 at 50 mV/s. The comparison of structural characterizations of AC and AC-10BRGO are given in Section 3.1. Based on N_2 adsorption-desorption isotherms, both AC and AC-10BRGO has a microporous structure. The pore size distrubution of AC is centered at 0.74 nm and that of AC-10BRGO is centered at 1.3 nm. The specific surface area of AC-10BRGO (1724 m^2/g) is smaller than that of AC (3038 m^2/g), suggesting that although specific surface area is significant for ion adsorption, the accessibility of electrolyte ions to the electrode surface outweighs for a better electrochemical performance [185]. The defective structure observed in AC-10BRGO, indicated by the threefold higher ID/IG ratio (3) compared to AC (0.92) from Raman analysis, suggests a significant role in ion adsorption due to the presence of defects, serving as active sites for electrolyte ions [176,177]. Further confirmation is provided by XPS spectra, revealing a dominance of oxygen surface functionalities in AC-10BRGO, as evidenced by the lower C/O ratio (8.96) compared to AC (11). The enhanced wettability resulting from the decoration of oxygen functional groups [186] on the electrode surface is supported by both Raman and XPS analyses. Additionally, FTIR results corroborate these findings, suggesting successful boron doping into the AC structure due to B-O bond at 1300 cm^{-1} and the presence of oxygen functionalities on the electrode surface.

The incorporation of BRGO into activated carbon improves the overall conductivity of the composite material. The high conductivity of BRGO forms conductive pathways that reduce internal resistance and allow for faster electron transfer during charge and discharge cycles. This results in enhanced rate capability, enabling the material to perform well even under rapid charging or discharging conditions. The BRGO sheets can also facilitate better ion diffusion within the composite material.

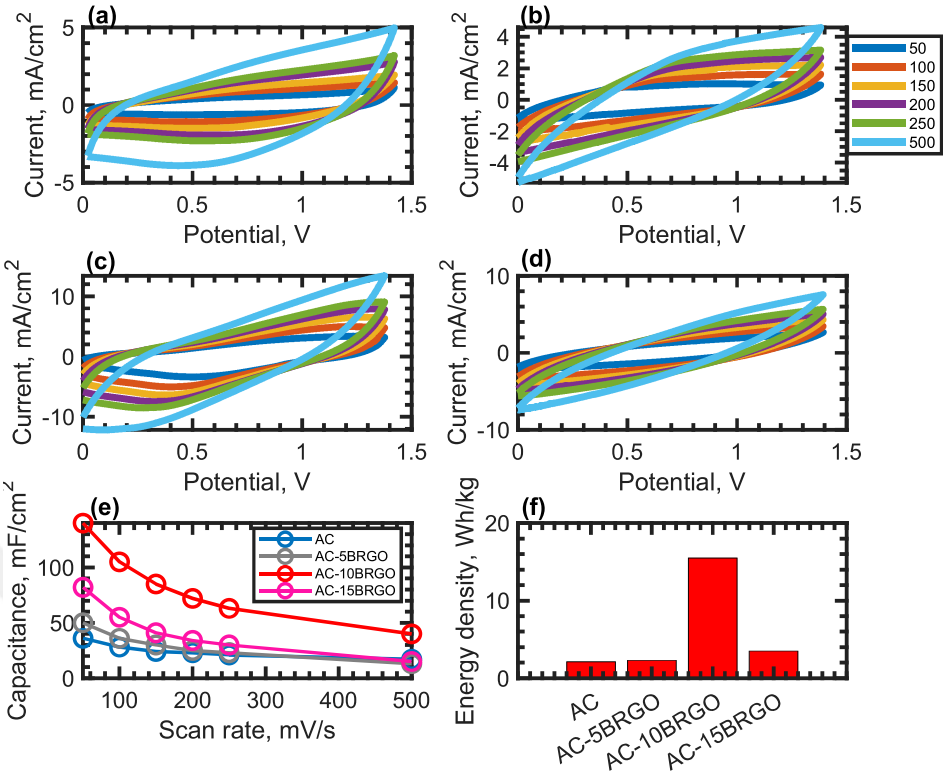

Figure 6.4. Electrochemical characterizations of AC and AC-BRGOs a. CV of AC, b. CV of AC-5BRGO, c. CV of AC-10BRGO, d. CV of AC-15BRGO, e. Capacitance vs. scan rate and f. Energy densities of the electrode materials at 50 mV/s at 1.4 V potential window.

The improved conductivity and the well-distributed BRGO network ensure that ions can quickly access the inner pores of activated carbon, enabling fast charge/discharge processes. The incorporation of BRGO into activated carbon can improve the mechanical properties of the composite. The boron-doped graphene oxide network provides structural support, preventing the collapse or degradation of the activated carbon matrix during repeated cycling. This helps preserve the surface area and porosity of the material over time, leading to better cycling stability. The strong covalent bonds in BRGO help prevent the loss of active material during cycling. Furthermore, BRGO acts as a binder that holds the activated carbon particles together, reducing the likelihood of material disintegration, which is common in pure activated carbon electrodes after many cycles. The electrochemical stability of BRGO/AC composites is also enhanced due to the presence of boron. The boron atoms increase the material's resistance to

oxidation and other side reactions with the electrolyte, thus improving the longevity and overall stability of the composite material in energy storage applications. Reduced graphene oxide, particularly when doped with boron, has excellent mechanical properties due to the strong covalent bonds between carbon atoms. When BRGO is incorporated into activated carbon, it can enhance the overall mechanical strength of the composite material, making it more resistant to deformation or fracture under mechanical stress. BRGO can impart flexibility to the activated carbon composite, enabling it to maintain its electrochemical performance even under bending or stretching. The layered structure of graphene oxide, combined with the doping of boron, allows the composite to be flexible without losing its conductive properties, making it suitable for applications in flexible supercapacitors.

6.2.2. Performance of Symmetric Supercapacitors with CQD-incorporated Gel Electrolyte

We integrated BRGO into AC structure during electrode preparation in order to improve charge transfer and elevate ion accessibility. BRGO amount in AC porous network was optimized as 10 wt. % (AC-10BRGO). AC-10BRGO was further tested with CQD contents of 0.5 wt.%, 1 wt.%, 1.5 wt.% in the gel polymer electrolyte.

Figure 6.5 (a), (c) and (e) display the cyclic voltammograms of the materials at various scan rates ranging from 50 to 500 mV/s. Additionally, charge-discharge curves spanning from 0.5 to 5 A/g are depicted in Figure 6.5(b), (d), and (f).

The capacitance from charging-discharging cycle is calculated as a function of current density using equation 2.12. Areal and mass capacitances are compared in Figure 6.5 (g) and (h) for different loading of CQD in gel electrolyte.

Cyclic voltammograms and GCD curves indicate that charge storage is primarily through physical adsorption of ions. 1.5 wt. % CQD addition to gel electrolyte has an adverse impact on capacitance (14.2 F/g at 0.5 A/g) and one plausible explanation for

the reduced capacitance at the highest CQD concentration is that CQDs may agglomerate and cause blockage within polymeric network. On the other hand, 1 wt. % CQD loading in gel polymer electrolyte enhances capacitance (107 F/g at 0.5 A/g), energy density (29 Wh/kg at 1.4 V) and scan rate dependence, which may be attributed to the fast charging properties of the composite materials. This composite material exhibits enhanced energy density performance compared to the metrics reported by other researchers for symmetric solid-state supercapacitors (Table A.2). The electrochemical characterizations of CQD added gel electrolyte confirm the results obtained from the structural characterizations which indicate the successful incorporation of CQD into gel electrolyte.

Further, ionic conductivity can be calculated as in

$$\sigma = \frac{T}{RA}, \tag{6.1}$$

where T is the thickness of the film (cm), R is the bulk resistance (Ω) obtained from the first intercept on the x-axis of the impedance data in the complex plane, and A is the contact area (cm^2). The thickness of the as-prepared gel film is measured to be 64 μm, while that of the CQD-incorporated gel film is 128 μm. With a contact area of 1 cm^2, the resistance is determined from impedance results (Figure A.9). Using this information, the ionic conductivity of the as-prepared gel film is calculated as 0.40 mS cm^{-1}, compared to 1.94 mS cm^{-1} for the CQD-incorporated gel film. The incorporation of carbon quantum dots (CQDs) significantly enhances the ionic conductivity of the gel electrolyte, likely due to the improved charge carrier mobility provided by the CQDs, which facilitates more efficient ion transport within the gel matrix.

One of the primary benefits of incorporating CQDs into gel electrolytes is the improvement in electrical conductivity. CQDs have an inherent ability to facilitate electron transport due to their excellent electrical conductivity, which is comparable to that of graphene and other carbon nanomaterials. When CQDs are added to the gel electrolyte, they can create conductive pathways throughout the electrolyte, enhanc-

ing the overall ion transport and charge/discharge efficiency. CQDs, due to their high surface area and the presence of sp^2 hybridized carbon bonds, can significantly reduce the internal resistance of the electrolyte. This leads to faster electron transfer between the electrode and the electrolyte, improving the overall efficiency of the supercapacitor. In gel electrolytes, the presence of CQDs can also improve ion transport by creating a more uniform distribution of ions. This is important because efficient ion movement in the electrolyte is crucial for high-capacitance supercapacitors that can operate at high rates. The conductive network provided by CQDs in the gel electrolyte can reduce the resistance to ion diffusion. This allows ions to move more efficiently within the electrolyte, improving the charge/discharge rate and leading to better performance at high power densities. The enhanced conductivity of the gel electrolyte with CQDs reduces the overall internal resistance of the supercapacitor, leading to a faster charge/discharge process. This results in better rate performance and makes the supercapacitor more efficient for high-power applications. Gel electrolytes, particularly those that are water-based or contain organic solvents, can undergo chemical degradation over time due to electrochemical reactions at the electrode-electrolyte interface. The presence of CQDs can help stabilize the electrolyte, reducing the rate of degradation and extending the cycle life of the supercapacitor. CQDs have excellent mechanical properties, which can help reinforce the gel electrolyte and prevent cracking or breakdown of the electrolyte matrix. This improves the mechanical stability of the electrolyte, ensuring long-term performance in flexible or wearable supercapacitor designs.

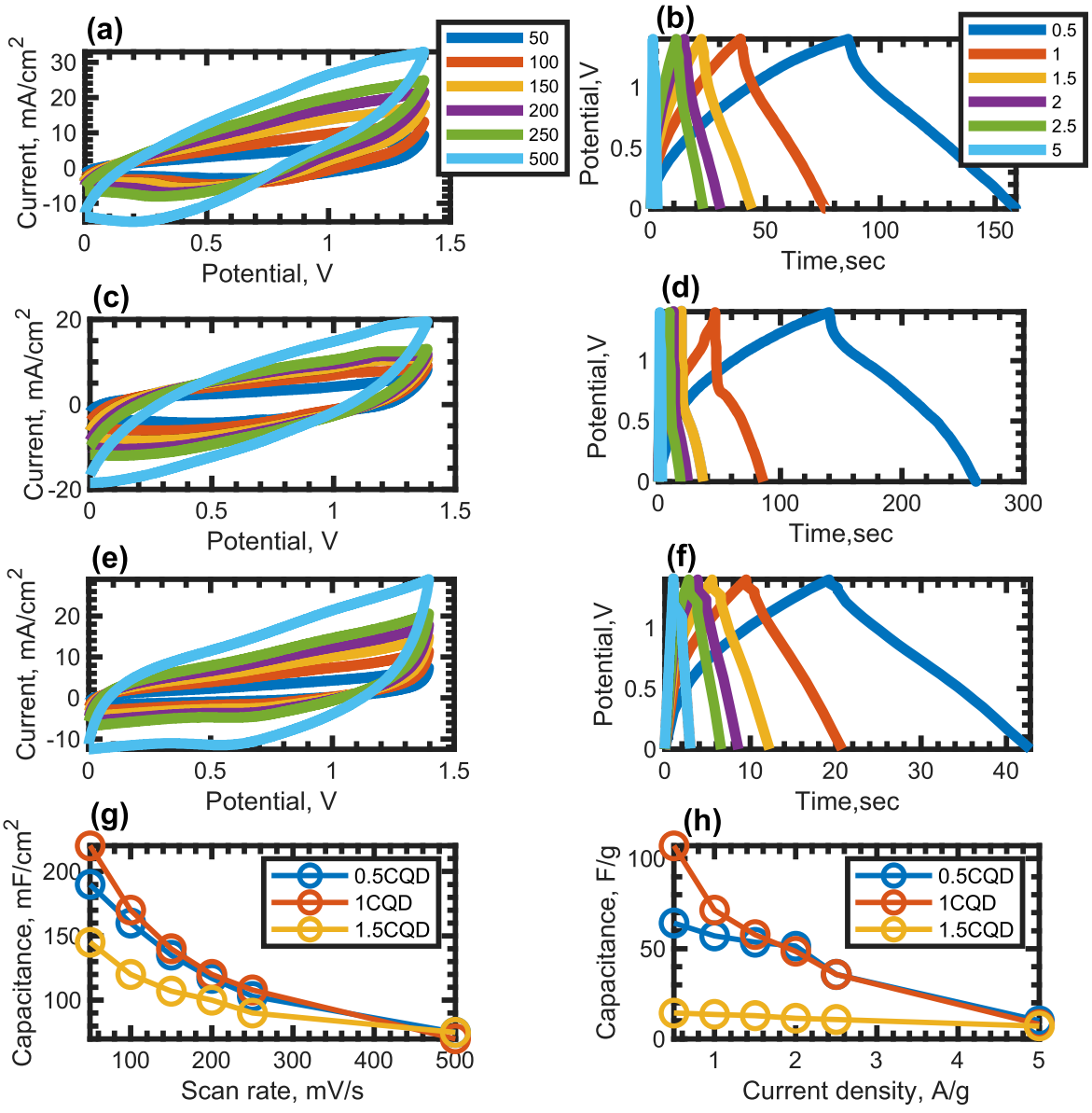

Figure 6.5. Electrochemical characterizations of 0.5 wt.%, 1 wt.%, 1.5 wt.% CQD a. CV of 0.5CQD, b. GCD of 0.5CQD, c. CV of 1CQD, d. GCD of 1CQD, e. CV of 1.5CQD, f. GCD of 1.5CQD, g. Areal capacitance vs. scan rate, h. Capacitance vs. current density, i. Energy densities and j. Comparison of energy densities.

7. CONCLUSION AND RECOMMENDATIONS

This dissertation has explored the development of biomass-derived activated carbon electrodes and their integration with nanomaterials to enhance the performance of supercapacitors. The primary objective was to improve capacitance, energy density, cycling stability, and mechanical flexibility, with a focus on sustainable and scalable materials. The research demonstrated that activated carbon synthesized from cabbage leaves exhibited a high surface area and hierarchical pore structure, leading to excellent electrochemical performance. The incorporation of RGO and CQDs into the electrode materials significantly enhanced their conductivity and stability. The optimized AC-15 % RGO-10 % CQD composite showed a remarkable increase in capacitance while also improving cycling stability. Furthermore, the integration of boron-doped RGO (BRGO) into the activated carbon structure enhanced charge transfer kinetics, resulting in higher capacitance and energy density. The development of a novel CQD-incorporated gel electrolyte improved ion mobility and device stability, demonstrating its potential for next-generation flexible energy storage applications. A thorough structural and electrochemical characterization validated the successful synthesis and integration of these materials, confirming their viability for supercapacitor applications.

The dissertation provided a comprehensive statistical analysis of the existing literature on supercapacitors, systematically evaluating over 1,700 data points from published research. This analysis helped establish key correlations between material properties and electrochemical performance, serving as a foundational reference for the experimental studies that followed. Experimental validation further confirmed that the activation and synthesis methods used in this study resulted in superior electrode properties compared to conventional methods.

This dissertation also investigated the role of hybrid electrode compositions, particularly the integration of RGO and CQDs into biomass-derived activated carbon. The experimental findings demonstrated that these nanomaterials significantly enhanced

capacitance, improved charge retention, and contributed to the mechanical flexibility of the supercapacitors. The incorporation of these functional materials enabled the development of a high-performance, flexible solid-state supercapacitor capable of maintaining stability under bending and deformation, which is critical for applications in wearable electronics.

This work also explored the impact of boron doping in graphene-based electrodes and the development of CQD-incorporated gel electrolytes. The findings revealed that boron doping improved charge transfer efficiency and electrochemical stability, leading to higher energy storage capacity. Additionally, the novel gel electrolyte composition significantly enhanced ion mobility and device stability, addressing common limitations associated with traditional liquid electrolytes. These advancements demonstrated that the combination of surface modifications and innovative electrolyte formulations could lead to next-generation energy storage devices with superior performance.

Beyond material synthesis, this dissertation also provided insights into the underlying charge storage mechanisms that govern performance in these novel electrode-electrolyte systems. The electrochemical analysis, including cyclic voltammetry, galvanostatic charge-discharge, and electrochemical impedance spectroscopy, revealed significant improvements in charge transport, diffusion efficiency, and electrochemical stability. These findings contribute to the broader understanding of how surface chemistry modifications and pore structure optimization impact supercapacitor performance. Additionally, the study highlighted the advantages of biowaste-derived materials in energy storage applications, offering a sustainable alternative to conventional electrode materials. The successful integration of advanced nanomaterials further demonstrates that low-cost, naturally derived carbon sources can compete with commercial counterparts in electrochemical energy storage.

The results of this research not only confirm the feasibility of biomass-derived carbon electrodes for supercapacitor applications but also provide a strong foundation for future advancements in the field. By demonstrating that renewable biowaste

materials can be effectively used to develop high-performance supercapacitors, this dissertation contributes to the ongoing efforts toward sustainable and environmentally friendly energy storage solutions. The insights gained from this study have the potential to shape future research directions, particularly in the areas of material scalability, electrochemical optimization, and device integration.

While the findings of this dissertation represent a significant advancement, several areas warrant further investigation to refine the material properties and enhance the overall device performance. Further optimization of activation processes through different chemical treatments and activation techniques could fine-tune the pore structure and surface functionalities, leading to improved charge storage capabilities. Exploring additional dopants such as nitrogen and sulfur, as well as alternative nanomaterials like MXenes and metal-organic frameworks, could provide synergistic effects that further enhance capacitance and stability. The development of new gel electrolytes with higher ionic conductivity and wider electrochemical stability windows could contribute to improved energy density and efficiency. Additionally, a comprehensive life cycle assessment and cost analysis should be conducted to evaluate the commercial feasibility of biomass-derived electrodes for large-scale applications.

Future research should also focus on integrating these materials into prototype devices and testing them under real-world conditions to assess their long-term performance and durability. The application of machine learning techniques could accelerate the optimization process by predicting the best electrode and electrolyte compositions for enhanced performance. Furthermore, investigating the integration of these supercapacitors into hybrid energy storage systems, particularly in combination with batteries, could expand their applicability to renewable energy grids and wearable electronic devices. Addressing these challenges will contribute to the advancement of energy storage technologies.

REFERENCES

1. González, A., E. Goikolea, J. A. Barrena and R. Mysyk, "Review on Supercapacitors: Technologies and Materials", *Renewable and Sustainable Energy Reviews*, Vol. 58, pp. 1189–1206, 2016.

2. Forouzandeh, P., V. Kumaravel and S. C. Pillai, "Electrode Materials for Supercapacitors: A Review of Recent Advances", *Catalysts*, Vol. 10, No. 9, p. 969, 2020.

3. Wu, Q., T. He, Y. Zhang, J. Zhang, Z. Wang, Y. Liu, L. Zhao, Y. Wu and F. Ran, "Cyclic Stability of Supercapacitors: Materials, Energy Storage Mechanism, Test Methods, and Device", *Journal of Materials Chemistry A*, Vol. 9, No. 43, pp. 24094–24147, 2021.

4. Sharma, S. and P. Chand, "Supercapacitor and Electrochemical Techniques: A Brief Review", *Results in Chemistry*, Vol. 5, p. 100885, 2023.

5. Tong, Y., J. Yang, J. Li, Z. Cong, L. Wei, M. Liu, S. Zhai, K. Wang and Q. An, "Lignin-derived Electrode Materials for Supercapacitor Applications: Progress and Perspectives", *Journal of Materials Chemistry A*, Vol. 11, pp. 1061–1082, 2023.

6. Yang, Z., J. Zhang, M. C. Kintner-Meyer, X. Lu, D. Choi, J. P. Lemmon and J. Liu, "Electrochemical Energy Storage for Green Grid", *Chemical reviews*, Vol. 111, No. 5, pp. 3577–3613, 2011.

7. Yan, J., Q. Wang, T. Wei and Z. Fan, "Recent Advances in Design and Fabrication of Electrochemical Supercapacitors with High Energy Densities", *Advanced Energy Materials*, Vol. 4, No. 4, p. 1300816, 2014.

8. Saadetnejad, D. and R. Yıldırım, "Photocatalytic Hydrogen Production by Water

Splitting over Au/Al-SrTiO3", *international journal of hydrogen energy*, Vol. 43, No. 2, pp. 1116–1122, 2018.

9. Zhang, L. L. and X. S. Zhao, "Carbon-based Materials as Supercapacitor Electrodes", *Chem. Soc. Rev.*, Vol. 38, pp. 2520–2531, 2009.

10. Mandal, S., J. Hu and S. Q. Shi, "A Comprehensive Review of Hybrid Supercapacitor from Transition Metal and Industrial Crop-based Activated Carbon for Energy Storage Applications", *Materials Today Communications*, Vol. 34, p. 105207, 2023.

11. Sun, J., B. Luo and H. Li, "A Review on the Conventional Capacitors, Supercapacitors, and Emerging Hybrid Ion Capacitors: Past, Present, and Future", *Advanced Energy and Sustainability Research*, Vol. 3, No. 6, p. 2100191, 2022.

12. Dubal, D. P., N. R. Chodankar, D.-H. Kim and P. Gomez-Romero, "Towards Flexible Solid-state Supercapacitors for Smart and Wearable Electronics", *Chemical Society Reviews*, Vol. 47, No. 6, pp. 2065–2129, 2018.

13. Wang, Y., L. Zhang, H. Hou, W. Xu, G. Duan, S. He, K. Liu and S. Jiang, "RecentPprogress in Carbon-based Materials for Supercapacitor Electrodes: A Review", *Journal of Materials Science*, Vol. 56, pp. 173–200, 2021.

14. Zeng, M.-J., X. Li, W. Li, T. Zhao, J. Wu, S.-M. Hao and Z.-Z. Yu, "Self-supported and Hierarchically Porous Activated Carbon Nanotube/Carbonized Wood Electrodes for High-performance Solid-state Supercapacitors", *Applied Surface Science*, Vol. 598, p. 153765, 2022.

15. Pandolfo, T., V. Ruiz, S. Sivakkumar and J. Nerkar, "General Properties of Electrochemical Capacitors", *Supercapacitors: Materials, systems, and applications*, Vol. 1, pp. 69–109, 2013.

16. Chatterjee, D. P. and A. K. Nandi, "A Review on the Recent Advances in Hybrid

Supercapacitors", *Journal of Materials Chemistry A*, Vol. 9, No. 29, pp. 15880–15918, 2021.

17. Zhai, Z., L. Zhang, T. Du, B. Ren, Y. Xu, S. Wang, J. Miao and Z. Liu, "A Review of Carbon Materials for Supercapacitors", *Materials & Design*, Vol. 221, p. 111017, 2022.

18. Şahin, M. E., F. Blaabjerg and A. Sangwongwanich, "A Comprehensive Review on Supercapacitor Applications and Developments", *Energies*, Vol. 15, No. 3, p. 674, 2022.

19. Sinha, P. and K. K. Kar, "Introduction to Supercapacitors", *Handbook of nanocomposite supercapacitor materials II: Performance*, Springer, Switzerland, 2020.

20. Shao, Y., M. F. El-Kady, J. Sun, Y. Li, Q. Zhang, M. Zhu, H. Wang, B. Dunn and R. B. Kaner, "Design and Mechanisms of Asymmetric Supercapacitors", *Chemical reviews*, Vol. 118, No. 18, pp. 9233–9280, 2018.

21. Shi, J., B. Xu, Y. Shen and J. Wu, "Energy Management Strategy for Battery/Supercapacitor Hybrid Electric City Bus-based on Driving Pattern Recognition", *Energy*, Vol. 243, p. 122752, 2022.

22. Frackowiak, E., "Carbon Materials for Supercapacitor Application", *Physical chemistry chemical physics*, Vol. 9, No. 15, pp. 1774–1785, 2007.

23. Oyedotun, K. O., J. O. Ighalo, J. F. Amaku, C. Olisah, A. O. Adeola, K. O. Iwuozor, K. G. Akpomie, J. Conradie and K. A. Adegoke, "Advances in Supercapacitor Development: Materials, Processes, and Applications", *Journal of Electronic Materials*, Vol. 52, No. 1, pp. 96–129, 2023.

24. Dhanda, M., R. Arora, S. Ahlawat, S. Nehra and S. Lata, "Electrolyte as a Panacea to Contemporary Scientific World of Super-capacitive Energy: A Con-

dense Report", *Journal of Energy Storage*, Vol. 52, p. 104740, 2022.

25. Raza, W., F. Ali, N. Raza, Y. Luo, K.-H. Kim, J. Yang, S. Kumar, A. Mehmood and E. E. Kwon, "Recent Advancements in Supercapacitor Technology", *Nano Energy*, Vol. 52, pp. 441–473, 2018.

26. Burke, A., "Ultracapacitors: Why, How, and Where is the Technology", *Journal of power sources*, Vol. 91, No. 1, pp. 37–50, 2000.

27. Zhao, X., B. M. Sánchez, P. J. Dobson and P. S. Grant, "The Role of Nanomaterials in Redox-based Supercapacitors for Next Generation Energy Storage Devices", *Nanoscale*, Vol. 3, pp. 839–855, 2011.

28. Jiya, I. N., N. Gurusinghe and R. Gouws, "Electrical Circuit Modelling of Double Layer Capacitors for Power Electronics and Energy Storage Applications: A Review", *Electronics*, Vol. 7, No. 11, p. 268, 2018.

29. Peng, X., H. Liu, Q. Yin, J. Wu, P. Chen, G. Zhang, G. Liu, C. Wu and Y. Xie, "A Zwitterionic Gel Electrolyte for Efficient Solid-state Supercapacitors", *Nature communications*, Vol. 7, No. 1, p. 11782, 2016.

30. Cheng, X., J. Pan, Y. Zhao, M. Liao and H. Peng, "Gel Polymer Electrolytes for Electrochemical Energy Storage", *Advanced Energy Materials*, Vol. 8, No. 7, p. 1702184, 2018.

31. Alipoori, S., S. Mazinani, S. H. Aboutalebi and F. Sharif, "Review of PVA-based Gel Polymer Electrolytes in Flexible Solid-state Supercapacitors: Opportunities and Challenges", *Journal of energy storage*, Vol. 27, p. 101072, 2020.

32. Ponce, M. F., A. Mamani, F. Jerez, J. Castilla, P. B. Ramos, G. G. Acosta, M. F. Sardella and M. A. Bavio, "Activated Carbon From Olive Tree Pruning Residue for Symmetric Solid-state Supercapacitor", *Energy*, Vol. 260, p. 125092, 2022.

33. Lakshmi, K. C. S. and B. Vedhanarayanan, "High-Performance Supercapacitors: A Comprehensive Review on Paradigm Shift of Conventional Energy Storage Devices", *Batteries*, Vol. 9, No. 4, p. 202, 2023.

34. Chen, W., H. Xiao, X. Zhou, X. Xu, S. Jiang, Z. Qin, S. Ding, C. Bian and Z. Liu, "Highly Deformable Graphene/Poly(3,4-ethylenedioxythiophene):Poly(styrene Sulfonate) Hydrogel Composite Film for Stretchable Supercapacitors", *ACS Applied Energy Materials*, Vol. 5, No. 6, pp. 7277–7286, 2022.

35. Lu, X., M. Yu, G. Wang, Y. Tong and Y. Li, "Flexible Solid-state Supercapacitors: Design, Fabrication and Applications", *Energy Environ. Sci.*, Vol. 7, pp. 2160–2181, 2014.

36. Hassan, M., M. A. Gondal, E. Cevik and A. Bozkurt, "Synthesis of a Molybdate-Chelated Biodegradable Gel Electrolyte for High Energy Density Supercapacitors", *ACS Applied Energy Materials*, Vol. 5, No. 6, pp. 6833–6846, 2022.

37. Yu, Z., L. Tetard, L. Zhai and J. Thomas, "Supercapacitor Electrode Materials: Nanostructures from 0 to 3 Dimensions", *Energy & Environmental Science*, Vol. 8, No. 3, pp. 702–730, 2015.

38. Lakshmi, K. S. and B. Vedhanarayanan, "High-Performance Supercapacitors: A Comprehensive Review on Paradigm Shift of Conventional Energy Storage Devices", *Batteries*, Vol. 9, No. 4, p. 202, 2023.

39. Saikia, B. K., S. M. Benoy, M. Bora, J. Tamuly, M. Pandey and D. Bhattacharya, "A Brief Review on Supercapacitor Energy Storage Devices and Utilization of Natural Carbon Resources as Their Electrode Materials", *Fuel*, Vol. 282, p. 118796, 2020.

40. Samantaray, S., D. Mohanty, I.-M. Hung, M. Moniruzzaman and S. K. Satpathy, "Unleashing Recent Electrolyte Materials for Next-generation Supercapaci-

tor Applications: A Comprehensive Review", *Journal of Energy Storage*, Vol. 72, p. 108352, 2023.

41. Shah, S. S., F. Niaz, M. A. Ehsan, H. T. Das, M. Younas, A. S. Khan, H. U. Rahman, S. A. Nayem, M. Oyama and M. A. Aziz, "Advanced Strategies in Electrode Engineering and Nanomaterial Modifications for Supercapacitor Performance Enhancement: A Comprehensive Review", *Journal of Energy Storage*, Vol. 79, p. 110152, 2024.

42. Ahankari, S., D. Lasrado and R. Subramaniam, "Advances in Materials and Fabrication of Separators in Supercapacitors", *Materials Advances*, Vol. 3, No. 3, pp. 1472–1496, 2022.

43. Momodu, D. Y., *Investigation of Metal Hydroxides Graphene Composites as Electrode Materials for Supercapacitor Applications*, Ph.D. Thesis, University of Pretoria, South Africa, 2015.

44. Iqbal, M. and U. Aziz, "Supercapattery: Merging of Battery-Supercapacitor Electrodes for Hybrid Energy Storage Devices", *The Journal of Energy Storage*, Vol. 46, p. 103823, 2022.

45. Oyedotun, K., *Synthesis and Characterization of Carbon-based Nanostructured Material Electrodes for Designing Novel Hybrid Supercapacitors*, Ph.D. Thesis, University of Pretoria, South Africa, 2018.

46. Nagarajarao, S. H., A. Nandagudi, R. Viswanatha, B. M. Basavaraja, M. S. Santosh, B. M. Praveen and A. Pandith, "Recent Developments in Supercapacitor Electrodes: A Mini Review", *ChemEngineering*, Vol. 6, No. 1, p. 5, 2022.

47. Zhou, M., X. Li, H. Zhao, J. Wang, Y. Zhao, F. Ge and Z. Cai, "Combined Effect of Nitrogen and Oxygen Heteroatoms and Micropores of Porous Carbon Frameworks from Schiff-Base Networks on Its High Supercapacitance", *Journal*

of Materials Chemistry A, Vol. 6, pp. 1621–1629, 2017.

48. Espinoza, E. M., J. A. Clark, J. Soliman, J. B. Derr, M. Morales and V. I. Vullev, "Practical Aspects of Cyclic Voltammetry: How to Estimate Reduction Potentials When Irreversibility Prevails", *Journal of The Electrochemical Society*, Vol. 166, No. 5, pp. H3175–H3187, 2019.

49. Mathis, T. S., N. Kurra, X. Wang, D. Pinto, P. Simon and Y. Gogotsi, "Energy Storage Data Reporting in Perspective—Guidelines for Interpreting the Performance of Electrochemical Energy Storage Systems", *Advanced Energy Materials*, Vol. 9, No. 39, p. 1902007, 2019.

50. Jayalakshmi, M. and K. Balasubramanian, "Simple Capacitors to Supercapacitors-An Overview", *International Journal of Electrochemical Science*, Vol. 3, No. 11, pp. 1196–1217, 2008.

51. Libich, J., J. Máca, J. Vondrák, O. Čech and M. Sedlaříková, "Supercapacitors: Properties and Applications", *Journal of energy storage*, Vol. 17, pp. 224–227, 2018.

52. Simon, P. and Y. Gogotsi, "Materials for Electrochemical Capacitors", *Nature materials*, Vol. 7, No. 11, pp. 845–854, 2008.

53. Shao, H., Y.-C. Wu, Z. Lin, P.-L. Taberna and P. Simon, "Nanoporous Carbon for Electrochemical Capacitive Energy Storage", *Chemical Society Reviews*, Vol. 49, No. 10, pp. 3005–3039, 2020.

54. Tiruye, G. A., *Application of Ionic Liquids, Innovative Polymer Electrolytes and Novel Carbonaceous Materials in Supercapacitors*, Ph.D. Thesis, Universidad Autónoma de Madrid, Spain, 2016.

55. Cao, Z., J. Zhang, Y. Ding, Y. Li, M. Shi, H. Yue, Y. Qiao, Y. Yin and S. Yang, "In-situ Synthesis of Flexible Elastic N-doped Carbon Foam as a Carbon Current

Collector and Interlayer for High-performance Lithium-sulfur Batteries", *Journal of Materials Chemistry A*, Vol. 4, No. 22, pp. 8636–8644, 2016.

56. Sharma, K., A. Arora and S. K. Tripathi, "Review of Supercapacitors: Materials and Devices", *Journal of Energy Storage*, Vol. 21, pp. 801–825, 2019.

57. Bozym II, D. J., *The Functionalized Graphene-Ionic Liquid Interface for Electrochemical Double-Layer Capacitors*, Ph.D. Thesis, Princeton University, USA, 2015.

58. Uralcan, B., *Computer-Aided Understanding of Perturbations in Soft Matter Systems*, Ph.D. Thesis, Princeton University, USA, 2019.

59. Bokhari, S. W., A. H. Siddique, P. C. Sherrell, X. Yue, K. M. Karumbaiah, S. Wei, A. V. Ellis and W. Gao, "Advances in Graphene-based Supercapacitor Electrodes", *Energy Reports*, Vol. 6, pp. 2768–2784, 2020.

60. Salanne, M., B. Rotenberg, K. Naoi, K. Kaneko, P.-L. Taberna, C. P. Grey, B. Dunn and P. Simon, "Efficient Storage Mechanisms for Building Better Supercapacitors", *Nature Energy*, Vol. 1, No. 6, pp. 1–10, 2016.

61. Kumar, N., S.-B. Kim, S.-Y. Lee and S.-J. Park, "Recent Advanced Supercapacitor: A Review of Storage Mechanisms, Electrode Materials, Modification, and Perspectives", *Nanomaterials*, Vol. 12, No. 20, p. 3708, 2022.

62. Kumar, S., M. Goswami, N. Singh, N. Sathish, M. Reddy and S. Kumar, "Exploring Carbon Quantum Dots as an Aqueous Electrolyte for Energy Storage Devices", *Journal of Energy Storage*, Vol. 55, p. 105522, 2022.

63. Lemine, A. S., M. M. Zagho, T. Altahtamouni and N. Bensalah, "Graphene a Promising Electrode Material for Supercapacitors—A review", *International Journal of energy research*, Vol. 42, No. 14, pp. 4284–4300, 2018.

64. Iijima, S., "Helical Microtubules of Graphitic Carbon", *ature*, Vol. 354, No. 6348, pp. 56–58, 1991.

65. Wang, Q., Z. Wen and J. Li, "A Hybrid Supercapacitor-fabricated with a Carbon Nanotube Cathode and a TiO2–B Nanowire Anode", *Advanced Functional Materials*, Vol. 16, No. 16, pp. 2141–2146, 2006.

66. Ye, J.-S., H. F. Cui, X. Liu, T. M. Lim, W.-D. Zhang and F.-S. Sheu, "Preparation and Characterization of Aligned Carbon Nanotube–Ruthenium Oxide Nanocomposites for Supercapacitors", *Small*, Vol. 1, No. 5, pp. 560–565, 2005.

67. Bhatnagar, A., W. Hogland, M. Marques and M. Sillanpää, "An Overview of the Modification Methods of Activated Carbon for Its Water Treatment Applications", *Chemical Engineering Journal*, Vol. 219, pp. 499–511, 2013.

68. Guo, R., L. Li, B. Wang, Y. Xiang, G. Zou, Y. Zhu, H. Hou and X. Ji, "Functionalized Carbon Dots for Advanced Batteries", *Energy Storage Materials*, Vol. 37, pp. 8–39, 2021.

69. Kumar, V. B., A. Borenstein, B. Markovsky, D. Aurbach, A. Gedanken, M. Talianker and Z. Porat, "Activated Carbon Modified with Carbon Nanodots as Novel Electrode Material for Supercapacitors", *The Journal of Physical Chemistry C*, Vol. 120, No. 25, pp. 13406–13413, 2016.

70. Li, J., X. Yun, Z. Hu, L. Xi, N. Li, H. Tang, P. Lu and Y. Zhu, "Three-dimensional Nitrogen and Phosphorus Co-doped Carbon Quantum Dots/Reduced Graphene Oxide Composite Aerogels with a Hierarchical Porous Structure as Superior Electrode Materials for Supercapacitors", *Journal of Materials Chemistry A*, Vol. 7, No. 46, pp. 26311–26325, 2019.

71. Lv, H., Y. Yuan, Q. Xu, H. Liu, Y.-G. Wang and Y. Xia, "Carbon Quantum Dots Anchoring MnO2/Graphene Aerogel Exhibits Excellent Performance as Electrode

Materials for Supercapacitor", *Journal of Power Sources*, Vol. 398, pp. 167–174, 2018.

72. Prasath, A., M. Athika, E. Duraisamy, A. Selva Sharma, V. Sankar Devi and P. Elumalai, "Carbon Quantum Dot-anchored Bismuth Oxide Composites as Potential Electrode for Lithium-ion Battery and Supercapacitor Applications", *ACS omega*, Vol. 4, No. 3, pp. 4943–4954, 2019.

73. Yushin, G., A. Nikitin and Y. Gogotsi, "Carbide-derived Carbon", *Carbon Nanomater*, Vol. 1, pp. 211–54, 2006.

74. Presser, V., M. Heon and Y. Gogotsi, "Carbide-derived Carbons–from Porous Networks to Nanotubes and Graphene", *Advanced Functional Materials*, Vol. 21, No. 5, pp. 810–833, 2011.

75. Zhang, P., Z.-A. Qiao and S. Dai, "Recent Advances in Carbon Nanospheres: Synthetic Routes and Applications", *Chemical Communications*, Vol. 51, No. 45, pp. 9246–9256, 2015.

76. Nieto-Márquez, A., R. Romero, A. Romero and J. L. Valverde, "Carbon Nanospheres: Synthesis, Physicochemical Properties and Applications", *Journal of Materials chemistry*, Vol. 21, No. 6, pp. 1664–1672, 2011.

77. Caturla, F., M. Molina-Sabio and F. Rodriguez-Reinoso, "Preparation of Activated Carbon by Chemical Activation with ZnCl2", *Carbon*, Vol. 29, No. 7, pp. 999–1007, 1991.

78. Heidarinejad, Z., M. H. Dehghani, M. Heidari, G. Javedan, I. Ali and M. Sillanpää, "Methods for Preparation and Activation of Activated Carbon: A Review", *Environmental Chemistry Letters*, Vol. 18, pp. 393–415, 2020.

79. Yakout, S. and G. S. El-Deen, "Characterization of Activated Carbon Prepared by Phosphoric Acid Activation of Olive Stones", *Arabian journal of chemistry*,

Vol. 9, pp. S1155–S1162, 2016.

80. Kumar, V. K. and N. Panwar, "A Review on Porous Carbon Synthesis Processes and Its Application as Energy Storage Supercapacitor", *Journal of the Indian Chemical Society*, Vol. 1, p. 101231, 2024.

81. Wang, D., S. Liu, G. Fang, G. Geng and J. Ma, "From Trash to Treasure: Direct Transformation of Onion Husks into Three-Dimensional Interconnected Porous Carbon Frameworks for High-performance Supercapacitors in Organic Electrolyte", *Electrochimica Acta*, Vol. 216, pp. 405–411, 2016.

82. Misnon, I. I., N. K. M. Zain, R. Abd Aziz, B. Vidyadharan and R. Jose, "Electrochemical Properties of Carbon from Oil Palm Kernel Shell for High Performance Supercapacitors", *Electrochimica Acta*, Vol. 174, pp. 78–86, 2015.

83. Mo, R.-J., Y. Zhao, M. Wu, H.-M. Xiao, S. Kuga, Y. Huang, J.-P. Li and S.-Y. Fu, "Activated Carbon from Nitrogen Rich Watermelon Rind for High-performance Supercapacitors", *RSC advances*, Vol. 6, No. 64, pp. 59333–59342, 2016.

84. Xiao, Z., W. Chen, K. Liu, P. Cui and D. Zhan, "Porous Biomass Carbon-derived from Peanut Shells as Electrode Materials with Enhanced Electrochemical Performance for Supercapacitors", *International Journal of Electrochemical Science*, Vol. 13, No. 6, pp. 5370–5381, 2018.

85. Khan, A., R. Arumugam Senthil, J. Pan, Y. Sun and X. Liu, "Hierarchically Porous Biomass Carbon-derived from Natural Withered Rose Flowers as High-performance Material for Advanced Supercapacitors", *Batteries & supercaps*, Vol. 3, No. 8, pp. 731–737, 2020.

86. Yang, V., R. A. Senthil, J. Pan, T. R. Kumar, Y. Sun and X. Liu, "Hierarchical Porous Carbon-derived from Jujube Fruits as Sustainable and Ultrahigh Capacitance Material for Advanced Supercapacitors", *Journal of Colloid and Interface*

Science, Vol. 579, pp. 347–356, 2020.

87. Khan, A., R. A. Senthil, J. Pan, S. Osman, Y. Sun and X. Shu, "A New Biomass-derived Rod-like Porous Carbon from Tea Waste as Inexpensive and Sustainable Energy Material for Advanced Supercapacitor Application", *Electrochimica acta*, Vol. 335, p. 135588, 2020.

88. Li, J. and Q. Wu, "Water Bamboo-derived Porous Carbons as Electrode Materials for Supercapacitors", *New Journal of Chemistry*, Vol. 39, No. 5, pp. 3859–3864, 2015.

89. Wu, F.-C., R.-L. Tseng, C.-C. Hu and C.-C. Wang, "Physical and Electrochemical Characterization of Activated Carbons Prepared from Firwoods for Supercapacitors", *Journal of Power Sources*, Vol. 138, No. 1-2, pp. 351–359, 2004.

90. Subramanian, V., C. Luo, A. M. Stephan, K. Nahm, S. Thomas and B. Wei, "Supercapacitors from Activated Carbon-derived from Banana Fibers", *The Journal of Physical Chemistry C*, Vol. 111, No. 20, pp. 7527–7531, 2007.

91. Balathanigaimani, M., W.-G. Shim, M.-J. Lee, C. Kim, J.-W. Lee and H. Moon, "Highly Porous Electrodes from Novel Corn Grains-based Activated Carbons for Electrical Double Layer Capacitors", *Electrochemistry Communications*, Vol. 10, No. 6, pp. 868–871, 2008.

92. Rufford, T. E., D. Hulicova-Jurcakova, Z. Zhu and G. Q. Lu, "Nanoporous Carbon Electrode from Waste Coffee Beans for High Performance Supercapacitors", *Electrochemistry Communications*, Vol. 10, No. 10, pp. 1594–1597, 2008.

93. Jisha, M., Y. J. Hwang, J. S. Shin, K. S. Nahm, T. P. Kumar, K. Karthikeyan, N. Dhanikaivelu, D. Kalpana, N. Renganathan and A. M. Stephan, "Electrochemical Characterization of Supercapacitors Based on Carbons-derived from Coffee Shells", *Materials Chemistry and Physics*, Vol. 115, No. 1, pp. 33–39, 2009.

94. Kalpana, D., S. Cho, S. Lee, Y. Lee, R. Misra and N. Renganathan, "Recycled Waste Paper—A New Source of Raw Material for Electric Double Layer Capacitors", *Journal of Power Sources*, Vol. 190, No. 2, pp. 587–591, 2009.

95. Olivares-Marín, M., J. A. Fernández, M. J. Lázaro, C. Fernández-González, A. Macías-García, V. Gómez-Serrano, F. Stoeckli and T. Centeno, "Cherry Stones as Precursor of Activated Carbons for Supercapacitors", *Materials Chemistry and Physics*, Vol. 114, No. 1, pp. 323–327, 2009.

96. Zhao, S., C.-Y. Wang, M.-M. Chen, J. Wang and Z.-Q. Shi, "Potato Starch-based Activated Carbon Spheres as Electrode Material for Electrochemical Capacitor", *Journal of physics and chemistry of solids*, Vol. 70, No. 9, pp. 1256–1260, 2009.

97. Ismanto, A. E., S. Wang, F. E. Soetaredjo and S. Ismadji, "Preparation of Capacitor's Electrode from Cassava Peel Waste", *Bioresource Technology*, Vol. 101, No. 10, pp. 3534–3540, 2010.

98. Taer, E., M. Deraman, I. A. Talib, A. A. Umar, M. Oyama and R. M. Yunus, "Physical, Electrochemical and Supercapacitive Properties of Activated Carbon Pellets from Pre-carbonized Rubber Wood Sawdust by CO2 Activation", *Current Applied Physics*, Vol. 10, No. 4, pp. 1071–1075, 2010.

99. Li, X., C. Han, X. Chen and C. Shi, "Preparation and Performance of Straw-based Activated Carbon for Supercapacitor in Non-aqueous Electrolytes", *Microporous and Mesoporous Materials*, Vol. 131, No. 1-3, pp. 303–309, 2010.

100. Li, X., W. Xing, S. Zhuo, J. Zhou, F. Li, S.-Z. Qiao and G.-Q. Lu, "Preparation of Capacitor's Electrode from Sunflower Seed Shell", *Bioresource technology*, Vol. 102, No. 2, pp. 1118–1123, 2011.

101. Zhu, H., X. Wang, F. Yang and X. Yang, "Promising Carbons for Supercapacitors-derived from Fungi", *Advanced materials*, Vol. 23, No. 24, pp. 2745–2748, 2011.

102. Li, Z., L. Zhang, B. S. Amirkhiz, X. Tan, Z. Xu, H. Wang, B. C. Olsen, C. M. Holt and D. Mitlin, "Carbonized Chicken Eggshell Membranes with 3D Architectures as High-performance Electrode Materials for Supercapacitors", *Advanced Energy Materials*, Vol. 2, No. 4, pp. 431–437, 2012.

103. Wang, R., P. Wang, X. Yan, J. Lang, C. Peng and Q. Xue, "Promising Porous Carbon-derived from Celtuce Leaves with Outstanding Supercapacitance and CO2 Capture Performance", *ACS applied materials & interfaces*, Vol. 4, No. 11, pp. 5800–5806, 2012.

104. Mi, J., X.-R. Wang, R.-J. Fan, W.-H. Qu and W.-C. Li, "Coconut-shell-based Porous Carbons with a Tunable Micro/Mesopore Ratio for High-Performance Supercapacitors", *Energy & Fuels*, Vol. 26, p. 5321–5329, 2012.

105. Chen, M., X. Kang, T. Wumaier, J. Dou, B. Gao, Y. Han, G. Xu, Z. Liu and L. Zhang, "Preparation of Activated Carbon from Cotton Stalk and Its Application in Supercapacitor", *Journal of Solid State Electrochemistry*, Vol. 17, pp. 1005–1012, 2012.

106. Jiang, L., J. Yan, l. Hao, R. Xue, G. Sun and B. Yi, "High Rate Performance Activated Carbons Prepared from Ginkgo Shells for Electrochemical Supercapacitors", *Carbon*, Vol. 56, p. 146–154, 2013.

107. Wang, H., Z. Xu, A. Kohandehghan, Z. Li, K. Cui, X. Tan, T. Stephenson, C. King'ondu, C. Holt, B. Olsen, J. Tak, D. Harfield, A. Anyia and D. Mitlin, "Interconnected Carbon Nanosheets-derived from Hemp for Ultrafast Supercapacitors with High Energy", *ACS nano*, Vol. 7, pp. 5131–5141, 2013.

108. Li, Y. and X. Liu, "Activated Carbon/ZnO Composites Prepared Using Hydrochars as Intermediate and Their Electrochemical Performance in Supercapacitor", *Materials Chemistry and Physics*, Vol. 148, No. 1-2, pp. 380–386, 2014.

109. Peng, C., X. Yan, R. Wang, J.-w. Lang, Y.-j. Ou and Q.-j. Xue, "Promising Activated Carbons-derived from Waste Tea Leaves and Their Application in High Performance Supercapacitors Electrodes", *Electrochimica Acta*, Vol. 87, p. 401–408, 2013.

110. Liang, Q., L. Ye, Z.-H. Huang, Q. Xu, Y. Bai, F. Kang and Q.-H. Yang, "A Honeycomb-like Porous Carbon Derived from Pomelo Peel for Use in High-performance Supercapacitors", *Nanoscale*, Vol. 6, pp. 13831–13837, 2014.

111. Qian, W., F. Sun, Y. Xu, L. Qiu, C. Liu, S. Wang and F. Yan, "Human Hair-derived Carbon Akes for Electrochemical Supercapacitors", *Energy & Environmental Science*, Vol. 7, p. 379, 2014.

112. Gurumurthy, H., A. M. S. Aruni, K. Anuj, A. G. AM, C. K. Feng, N. Zainab and K. Sharma, "Biowaste Sago Bark Based Catalyst Free Carbon Nanospheres: Waste to Wealth Approach", *ACS Sustainable Chemistry & Engineering*, Vol. 3, No. 9, pp. 2247–2253, 2015.

113. Chang, J., Z. Gao, X. Wang, D. Wu, F. Xu, X. Wang, Y. Guo and K. Jiang, "Activated Porous Carbon Prepared from Paulownia Flower for High Performance Supercapacitor Electrodes", *Electrochimica Acta*, Vol. 157, pp. 290–298, 2015.

114. Long, C., L. Jiang, X. Wu, Y. Jiang, D. Yang, C. Wang, T. Wei and Z. Fan, "Facile Synthesis of Functionalized Porous Carbon with Three-Dimensional Interconnected Pore Structure for High Volumetric Performance Supercapacitors", *Carbon*, Vol. 93, pp. 412–420, 2015.

115. Wang, K., N. Zhao, S. Lei, R. Yan, X. Tian, J. Wang, Y. Song, D. Xu, Q. Guo and L. Liu, "Promising Biomass-based Activated Carbons Derived from Willow Catkins for High Performance Supercapacitors", *Electrochimica Acta*, Vol. 166, pp. 1–11, 2015.

116. Cheng, P., S. Gao, P. Zang, X. Yang, Y. Bai, H. Xu, Z. Liu and Z. Lei, "Hierarchically Porous Carbon by Activation of Shiitake Mushroom for Capacitive Energy Storage", *Carbon*, Vol. 93, pp. 315–324, 2015.

117. Li, Y.-T., Y.-T. Pi, L.-M. Lu, S.-H. Xu and T.-Z. Ren, "Hierarchical Porous Active Carbon from Fallen Leaves by Synergy of K2CO3 and Their Supercapacitor Performance", *Journal of Power Sources*, Vol. 299, pp. 519–528, 2015.

118. Yuan, C., L. Zhou, S. Zhu, H. Cao and L. Hou, "Albumen-derived Hierarchical Porous N-and O-enriched Carbon towards High-performance Electrochemical Capacitors", *Journal of The Electrochemical Society*, Vol. 162, No. 4, p. A781, 2015.

119. Qu, W.-H., Y.-Y. Xu, A.-H. Lu, X.-Q. Zhang and W.-C. Li, "Converting Biowaste Corncob Residue into High Value Added Porous Carbon for Supercapacitor Electrodes", *Bioresource technology*, Vol. 189, pp. 285–291, 2015.

120. Teo, E. Y. L., L. Muniandy, E.-P. Ng, F. Adam, A. R. Mohamed, R. Jose and K. F. Chong, "High Surface Area Activated Carbon from Rice Husk as a High-performance Supercapacitor Electrode", *Electrochimica Acta*, Vol. 192, pp. 110–119, 2016.

121. Gong, C., X. Wang, D. Ma, H. Chen, S. Zhang and Z. Liao, "Microporous Carbon from a Biological Waste-stiff Silkworm for Capacitive Energy Storage", *Electrochimica acta*, Vol. 220, pp. 331–339, 2016.

122. Sahu, V., R. B. Marichi, G. Singh and R. K. Sharma, "Hierarchical Polyaniline Spikes over Vegetable Oil-derived Carbon Aerogel for Solid-state Symmetric/Asymmetric Supercapacitor", *Electrochimica Acta*, Vol. 240, pp. 146–154, 2017.

123. Boyjoo, Y., Y. Cheng, H. Zhong, H. Tian, J. Pan, V. K. Pareek, J.-F. Lamonier,

M. Jaroniec and J. Liu, "From Waste Coca Cola® to Activated Carbons with Impressive Capabilities for CO2 Adsorption and Supercapacitors", *Carbon*, Vol. 116, pp. 490–499, 2017.

124. Zhong, C., Y. Deng, W. Hu, J. Qiao, L. Zhang and J. Zhang, "A Review of Electrolyte Materials and Compositions for Electrochemical Supercapacitors", *Chemical Society Reviews*, Vol. 44, No. 21, pp. 7484–7539, 2015.

125. Mendhe, A. and H. Panda, "A Review on Electrolytes for Supercapacitor Device", *Discover Materials*, Vol. 3, No. 1, p. 29, 2023.

126. Lewandowski, A., A. Olejniczak, M. Galinski and I. Stepniak, "Performance of Carbon–carbon Supercapacitors Based on Organic, Aqueous and Ionic Liquid Electrolytes", *Journal of Power Sources*, Vol. 195, No. 17, pp. 5814–5819, 2010.

127. Xia, L., L. Yu, D. Hu and G. Z. Chen, "Electrolytes for Electrochemical Energy Storage", *Materials Chemistry Frontiers*, Vol. 1, No. 4, pp. 584–618, 2017.

128. Haque, M., Q. Li, A. D. Smith, V. Kuzmenko, E. Köhler, P. Lundgren and P. Enoksson, "Thermal Influence on the Electrochemical Behavior of a Supercapacitor Containing an Ionic Liquid Electrolyte", *Electrochimica Acta*, Vol. 263, pp. 249–260, 2018.

129. Dai, H., G. Zhang, D. Rawach, C. Fu, C. Wang, X. Liu, M. Dubois, C. Lai and S. Sun, "Polymer Gel Electrolytes for Flexible Supercapacitors: Recent Progress, Challenges, and Perspectives", *Energy Storage Materials*, Vol. 34, pp. 320–355, 2021.

130. Baskoro, F., H. Q. Wong and H.-J. Yen, "Strategic Structural Design of a Gel Polymer Electrolyte toward a High Efficiency Lithium-ion Battery", *ACS Applied Energy Materials*, Vol. 2, No. 6, pp. 3937–3971, 2019.

131. Arya, A. and A. Sharma, "Polymer Electrolytes for Lithium-ion Batteries: A

Critical Study", *Ionics*, Vol. 23, No. 3, pp. 497–540, 2017.

132. Xu, K., "Nonaqueous Liquid Electrolytes for Lithium-Based Rechargeable Batteries", *Chemical reviews*, Vol. 104, No. 10, pp. 4303–4418, 2004.

133. Yeganeh Ghotbi, M., "Solid State Electrolytes for Electrochemical Energy Devices", *Journal of Materials Science: Materials in Electronics*, Vol. 30, No. 15, pp. 13835–13854, 2019.

134. Xu, Y., Z. Lin, X. Huang, Y. Liu, Y. Huang and X. Duan, "Flexible Solid-state Supercapacitors Based on Three-Dimensional Graphene Hydrogel Films", *ACS nano*, Vol. 7, No. 5, pp. 4042–4049, 2013.

135. Chodankar, N. R., D. P. Dubal, G. S. Gund and C. D. Lokhande, "Bendable All-solid-state Asymmetric Supercapacitors Based on MnO2 and Fe2O3 Thin Films", *Energy Technology*, Vol. 3, No. 6, pp. 625–631, 2015.

136. Jinisha, B., K. Anilkumar, M. Manoj, C. M. Ashraf, V. Pradeep and S. Jayalekshmi, "Solid-state Supercapacitor with Impressive Performance Characteristics, Assembled Using Redox-mediated Gel Polymer Electrolyte", *Journal of Solid State Electrochemistry*, Vol. 23, pp. 3343–3353, 2019.

137. Yu, H., J. Wu, L. Fan, K. Xu, X. Zhong, Y. Lin and J. Lin, "Improvement of the Performance for Quasi-Solid-state Supercapacitor by Using PVA–KOH–KI Polymer Gel Electrolyte", *Electrochimica Acta*, Vol. 56, No. 20, pp. 6881–6886, 2011.

138. Jia, M., S. Geng, Q. Jiang, C. Xu, Y. Zhang, G. Yin, F. Jia, X. Wang, T. Zhou and B. Liu, "A Strategy to Prepare Activated Carbon Fiber Membranes for Flexible Solid-state Supercapacitor Applications", *Journal of Materials Science*, Vol. 56, pp. 3911–3924, 2021.

139. Yang, C.-C., S.-T. Hsu and W.-C. Chien, "All Solid-state Electric Double-layer

Capacitors based on Alkaline Polyvinyl Alcohol Polymer Electrolytes", *Journal of power sources*, Vol. 152, pp. 303–310, 2005.

140. Abdisattar, A., M. Yeleuov, C. Daulbayev, K. Askaruly, A. Tolynbekov, A. Taurbekov and N. Prikhodko, "Recent Advances and Challenges of Current Collectors for Supercapacitors", *Electrochemistry Communications*, Vol. 1, p. 107373, 2022.

141. Zhang, Y.-Z., Y. Wang, T. Cheng, W.-Y. Lai, H. Pang and W. Huang, "Flexible Supercapacitors Based on Paper Substrates: A New Paradigm for Low-cost Energy Storage", *Chemical Society Reviews*, Vol. 44, No. 15, pp. 5181–5199, 2015.

142. Luo, P. and L. Huang, "Carbon Paper as Current Collectors in Graphene Gydrogel Electrodes for High-Performance Supercapacitors", *Nanomaterials*, Vol. 10, No. 4, p. 746, 2020.

143. Wang, X., Y. Chen, O. G. Schmidt and C. Yan, "Engineered Nanomembranes for Smart Energy Storage Devices", *Chemical Society Reviews*, Vol. 45, No. 5, pp. 1308–1330, 2016.

144. Li, J., H. Jia, S. Ma, L. Xie, X.-X. Wei, L. Dai, H. Wang, F. Su and C.-M. Chen, "Separator Design for High-Performance Supercapacitors: Requirements, Challenges, Strategies, and Prospects", *ACS Energy Letters*, Vol. 8, No. 1, pp. 56–78, 2022.

145. Bon, C. Y., L. Mohammed, S. Kim, M. Manasi, P. Isheunesu, K. S. Lee and J. M. Ko, "Flexible Poly (vinyl alcohol)-Ceramic Composite Separators for Supercapacitor Applications", *Journal of Industrial and Engineering Chemistry*, Vol. 68, pp. 173–179, 2018.

146. Phung, J., X. Zhang, W. Deng and G. Li, "An Overview of MOF-based Separators for Lithium-sulfur Batteries", *Sustainable Materials and Technologies*, Vol. 31, p. e00374, 2022.

147. Kim, J.-H., J.-H. Kim, E.-S. Choi, J. H. Kim and S.-Y. Lee, "Nanoporous Polymer Scaffold-embedded Nonwoven Composite Separator Membranes for High-rate Lithium-ion Batteries", *Rsc Advances*, Vol. 4, No. 97, pp. 54312–54321, 2014.

148. Bello, A., K. Makgopa, M. Fabiane, D. Dodoo-Ahrin, K. I. Ozoemena and N. Manyala, "Chemical Adsorption of NiO Nanostructures on Nickel Foam-Graphene for Supercapacitor Applications", *Journal of materials science*, Vol. 48, pp. 6707–6712, 2013.

149. Weingarth, D., A. Foelske-Schmitz, A. Wokaun and R. Kötz, "PTFE-bound Activated Carbon-a Quasi Reference Electrode for Ionic Liquids and Its application", *ECS Transactions*, Vol. 50, No. 11, p. 111, 2013.

150. Stoller, M. D. and R. S. Ruoff, "Best Practice Methods for Determining an Electrode Material's Performance for Ultracapacitors", *Energy & Environmental Science*, Vol. 3, No. 9, pp. 1294–1301, 2010.

151. Zhang, R., Y. Xu, D. Harrison, J. Fyson, D. Southee and A. Tanwilaisiri, "Fabrication and Characterisation of Energy Storage Fibres", *20th International Conference on Automation and Computing*, Vol. 1, pp. 228–230, 2014.

152. Zhao, Q., J. Chen, F. Luo, L. Shen, Y. Wang, K. Wu and M. Lu, "Vertically Oriented Polyaniline-Graphene Nanocomposite Based on Functionalized Graphene for Supercapacitor Electrode", *Journal of applied polymer science*, Vol. 134, p. 19, 2017.

153. Kuila, B. K., B. Nandan, M. Böhme, A. Janke and M. Stamm, "Vertically Oriented Arrays of Polyaniline Nanorods and Their Super Electrochemical Properties", *Chemical Communications*, Vol. 38, No. 38, pp. 5749–5751, 2009.

154. Kim, B. K., V. Chabot and A. Yu, "Carbon Nanomaterials Supported Ni (OH) 2/NiO Hybrid Flower Structure for Supercapacitor", *Electrochimica Acta*, Vol.

109, pp. 370–380, 2013.

155. Vicentini, R., J. P. Aguiar, R. Beraldo, R. Venâncio, F. Rufino, L. M. Da Silva and H. Zanin, "Ragone Plots for Electrochemical Double Layer Capacitors", *Batteries & Supercaps*, Vol. 4, No. 8, pp. 1291–1303, 2021.

156. Su, X.-L., J.-R. Chen, G.-P. Zheng, J.-H. Yang, X.-X. Guan, P. Liu and X.-C. Zheng, "Three-Dimensional Porous Activated Carbon-derived from Loofah Sponge Biomass for Supercapacitor Applications", *Applied Surface Science*, Vol. 436, pp. 327–336, 2018.

157. Yan, Y., L. Xia and L. Ma, "Solvent-controlled Synthesis of Multicolor Photoluminescent Carbon Dots for Bioimaging", *RSC Adv.*, Vol. 9, pp. 24057–24065, 2019.

158. Kaya, D., D. Koroglu, E. Aydın and B. Uralcan, "Optimization of Capacitance in Supercapacitors by Constructing an Experimentally Validated Hybrid Artificial Neural Networks-Genetic Algorithm Framework", *Journal of Power Sources*, Vol. 568, p. 232987, 2023.

159. Feng, G. and P. T. Cummings, "Supercapacitor Capacitance Exhibits Oscillatory Behavior as a Function of Nanopore Size", *The Journal of Physical Chemistry Letters*, Vol. 2, No. 22, pp. 2859–2864, 2011.

160. Lota, G., T. Centeno, E. Frackowiak and F. Stoeckli, "Improvement of the Structural and Chemical Properties of a Commercial Activated Carbon for Its Application in Electrochemical Capacitors", *Electrochimica Acta*, Vol. 53, No. 5, pp. 2210–2216, 2008.

161. Chmiola, J., C. Largeot, P.-L. Taberna, P. Simon and Y. Gogotsi, "Desolvation of Ions in Subnanometer Pores and Its Effect on Capacitance and Double-Layer Theory", *Angewandte Chemie (International ed. in English)*, Vol. 47, pp. 3392–5,

2008.

162. Raymundo-Piñero, E., K. Kierzek, J. Machnikowski and F. Béguin, "Relationship between the Nanoporous Texture of Activated Carbons and Their Capacitance Properties in Different Electrolytes", *Carbon*, Vol. 44, No. 12, pp. 2498–2507, 2006, carbon for Energy Storage and Environment Protection.

163. Chmiola, J., G. Yushin, Y. Gogotsi, C. Portet, P. Simon and P. Taberna, "Anomalous Increase in Carbon Capacitance at Pore Sizes Less Than 1 Nanometer", *Science (New York, N.Y.)*, Vol. 313, pp. 1760–3, 2006.

164. Lockett, V., R. Sedev, J. Ralston, M. Horne and T. Rodopoulos, "Differential Capacitance of the Electrical Double Layer in Imidazolium-based Ionic Liquids: Influence of Potential, Cation Size, and Temperature", *The Journal of Physical Chemistry C*, Vol. 112, No. 19, pp. 7486–7495, 2008.

165. Burt, R., K. Breitsprecher, B. Daffos, P.-L. Taberna, P. Simon, G. Birkett, X. S. Zhao, C. Holm and M. Salanne, "Capacitance of Nanoporous Carbon-based Supercapacitors Is a Trade-off between the Concentration and the Separability of the Ions", *The Journal of Physical Chemistry Letters*, Vol. 7, No. 19, pp. 4015–4021, 2016.

166. Korkut, A. S. and B. Uralcan, "Reduced Graphene Oxide/Ionic Liquid Composites with Tunable Interlayer Spacing for Improved Charge/Discharge Kinetics in Supercapacitors", *Nanotechnology*, Vol. 34, No. 23, p. 235402, 2023.

167. Uralcan, B., I. A. Aksay, P. G. Debenedetti and D. T. Limmer, "Concentration Fluctuations and Capacitive Response in Dense Ionic Solutions", *The Journal of Physical Chemistry Letters*, Vol. 7, No. 13, pp. 2333–2338, 2016.

168. Uralcan, B. and I. B. Uralcan, "Origin of Enhanced Performance in Nanoporous Electrical Double Layer Capacitors: Insights on Micropore Structure and Elec-

trolyte Composition from Molecular Simulations", *ACS Applied Materials & Interfaces*, Vol. 14, No. 14, pp. 16800–16808, 2022.

169. Donohue, M. and G. Aranovich, "Classification of Gibbs Adsorption Isotherms", *Advances in Colloid and Interface Science*, Vol. 76-77, pp. 137–152, 1998.

170. Yang, G., H. Zhang, X. Fan and W. Zheng, "Density Functional Theory Calculations for the Quantum Capacitance Performance of Graphene-based Electrode Material", *The Journal of Physical Chemistry C*, Vol. 119, No. 12, pp. 6464–6470, 2015.

171. Aziz, A., W. Yu, R. Tang, R. Crespo-Otero, D. Di Tommaso and H. Nishihara, "Theoretical Insights into the Role of Defects in the Optimization of the Electrochemical Capacitance of Graphene", *Energy Materials and Devices*, Vol. 3, p. 2, 2024.

172. Zhang, S. S., "Effect of Surface Oxygen Functionalities on Capacitance of Activated Carbon in Non-aqueous Electrolyte", *Journal of Solid State Electrochemistry*, Vol. 21, No. 7, pp. 2029–2036, 2017.

173. Qiu, C., L. Jiang, Y. Gao and L. Sheng, "Effects of Oxygen-containing Functional Groups on Carbon Materials in Supercapacitors: A Review", *Materials & Design*, Vol. 230, p. 111952, 2023.

174. Ferrari, A. C. and J. Robertson, "Interpretation of Raman Spectra of Disordered and Amorphous Carbon", *Physical review B*, Vol. 61, No. 20, p. 14095, 2000.

175. Verma, K. D., P. Sinha, M. K. Ghorai and K. K. Kar, "Mesoporous Electrode from Human Hair and Bio-based Gel Polymer Electrolyte for High-performance Supercapacitor", *Diamond and Related Materials*, Vol. 123, p. 108879, 2022.

176. Stankovich, S., D. A. Dikin, R. D. Piner, K. A. Kohlhaas, A. Kleinhammes, Y. Jia, Y. Wu, S. T. Nguyen and R. S. Ruoff, "Synthesis of Graphene-based Nanosheets

via Chemical Reduction of Exfoliated Graphite Oxide", *Carbon*, Vol. 45, No. 7, pp. 1558–1565, 2007.

177. Dwivedi, N., S. Kumar, H. Malik, G. Gupta, C. M. Rauthan and O. Panwar, "Correlation of sp3 and sp2 Fraction of Carbon with Electrical, Optical and Nanomechanical Properties of Argon-diluted Diamond-like Carbon Films", *Applied Surface Science*, Vol. 257, pp. 6804–6810, 2011.

178. Lv, L., Y. Fan, Q. Chen, Y. Zhao, Y. Hu, Z. Zhang, N. Chen and L. Qu, "Three-dimensional Multichannel Aerogel of Carbon Quantum Dots for High-Performance Supercapacitors", *Nanotechnology*, Vol. 25, No. 23, p. 235401, 2014.

179. Pan, Y., S. Yan, Y. Liu, Z. Tian, D. Li, Y. Chen, L. Guo and Y. Wang, "Significantly Enhanced Electrochemical Performance of 2D Ni-MOF by Carbon Quantum Dot for High-performance Supercapacitors", *Electrochimica Acta*, Vol. 422, p. 140560, 2022.

180. Cheng, R., Y. Xiang, R. Guo, L. Li, G. Zou, C. Fu, H. Hou and X. Ji, "Structure and Interface Modification of Carbon Dots for Electrochemical Energy Application", *Small*, Vol. 17, p. 2102091, 2021.

181. Santos, F., J. P. Tafur, J. Abad and A. J. Fernández Romero, "Structural Modifications and Ionic Transport of PVA-KOH Hydrogels Applied in Zn/Air batteries", *Journal of Electroanalytical Chemistry*, Vol. 850, p. 113380, 2019.

182. Jiang, M., J. Zhu, C. Chen, Y. Lu, Y. Ge and X. Zhang, "Poly(vinyl Alcohol) Borate Gel Polymer Electrolytes Prepared by Electrodeposition and Their Application in Electrochemical Supercapacitors", *ACS Applied Materials & Interfaces*, Vol. 8, No. 5, pp. 3473–3481, 2016.

183. Yang, C.-C., "Chemical Composition and XRD Analyses for Alkaline Composite PVA Polymer Electrolyte", *Materials Letters*, Vol. 58, No. 1, pp. 33–38, 2004.

184. Qi, B., K. Ren, Y. Lin, S. Zhang, T. Wei and Z. Fan, "Design of Layered-stacking Graphene Assemblies as Advanced Electrodes for Supercapacitors", *Particuology*, Vol. 60, pp. 1–13, 2022.

185. Zhong, H., F. Xu, Z. Li, R. Fu and D. Wu, "High-energy Supercapacitors Based on Hierarchical Porous Carbon with an Ultrahigh Ion-accessible Surface Area in Ionic Liquid Electrolytes", *Nanoscale*, Vol. 5, pp. 4678–4682, 2013.

186. ran Li, X., Y. hui Jiang, P. zhi Wang, Y. Mo, W. de Lai, Z. jiong Li, R. ji Yu, Y. ting Du, X. ren Zhang and Y. Chen, "Effect of the Oxygen Functional Groups of Activated Carbon on Its Electrochemical Performance for Supercapacitors", *New Carbon Materials*, Vol. 35, No. 3, pp. 232–243, 2020.

187. Yang, C.-C., S.-T. Hsu and W.-C. Chien, "All Solid-state Electric Double Layer Capacitors Based on Alkaline Polyvinyl Alcohol Polymer Electrolytes", *Journal of power sources*, Vol. 152, pp. 303–310, 2005.

188. Yu, H., J. Wu, L. Fan, K. Xu, X. Zhong, Y. Lin and J. Lin, "Improvement of the Performance for Quasi-solid-state Supercapacitor by Using PVA–KOH–KI Polymer Gel Electrolyte", *Electrochimica Acta*, Vol. 56, No. 20, pp. 6881–6886, 2011.

189. Ma, W., S. Chen, S. Yang, W. Chen, W. Weng and M. Zhu, "Bottom-up Fabrication of Activated Carbon Fiber for All-solid-state Supercapacitor with Excellent Electrochemical Performance", *ACS applied materials & interfaces*, Vol. 8, No. 23, pp. 14622–14627, 2016.

190. Xu, X., J. Gao, Q. Tian, X. Zhai and Y. Liu, "Walnut Shell-derived Porous Carbon for a Symmetric All-solid-state Supercapacitor", *Applied Surface Science*, Vol. 411, pp. 170–176, 2017.

191. Jinisha, B., K. Anilkumar, M. Manoj, C. M. Ashraf, V. Pradeep and S. Jay-

alekshmi, "Solid-state Supercapacitor with Impressive Performance Characteristics, Assembled Using Redox-mediated Gel Polymer Electrolyte", *Journal of Solid State Electrochemistry*, Vol. 23, pp. 3343–3353, 2019.

192. Liu, Y. and Z.-M. Liu, "Promoted Activity of Nitrogen-doped Activated Carbon as a Highly Efficient Oxygen Reduction Catalyst in Microbial Fuel Cells", *Journal of Applied Electrochemistry*, Vol. 49, pp. 119–133, 2019.

193. Jia, M., S. Geng, Q. Jiang, C. Xu, Y. Zhang, G. Yin, F. Jia, X. Wang, T. Zhou and B. Liu, "A Strategy to Prepare Activated Carbon Fiber Membranes for Flexible Solid-state Supercapacitor Applications", *Journal of Materials Science*, Vol. 56, pp. 3911–3924, 2021.

194. Tian, J., T. Zhang, D. Talifu, A. Abulizi and Y. Ji, "Porous Carbon Materials-derived from Waste Cotton Stalk with Ultra-high Surface Area for High Performance Supercapacitors", *Materials Research Bulletin*, Vol. 143, p. 111457, 2021.

195. Lee, K. S., Y. J. Seo and H. T. Jeong, "Capacitive Behavior of Functionalized Activated Carbon-based All-solid-state Supercapacitor", *Carbon Letters*, Vol. 31, No. 5, pp. 1041–1049, 2021.

196. Lee, K. S. and H. T. Jeong, "Development and Optimization of Ionic Liquid Based Gel Polymer Electrolyte for All-solid-state Supercapacitor", *Journal of Energy Storage*, Vol. 42, p. 103001, 2021.

197. Sundriyal, S., V. Shrivastav, A. Kaur, P. Dubey, S. Mishra, A. Deep and S. R. Dhakate, "Waste Office Papers as a Cellulosic Material Reservoir to Derive Highly Porous Activated Carbon for Solid-state Electrochemical Capacitor", *Transactions on Nanotechnology*, Vol. 20, pp. 481–488, 2021.

198. Anand, S., M. W. Ahmad, A. Syed, A. H. Bahkali, M. Verma, B. H. Kim and A. Choudhury, "Walnut Shell-derived N, S Co-doped Activated Carbon for Solid-

state Symmetry Supercapacitor Device", *Journal of Industrial and Engineering Chemistry*, Vol. 129, pp. 309–320, 2024.

199. Yoo, J. J., K. Balakrishnan, J. Huang, V. Meunier, B. G. Sumpter, A. Srivastava, M. Conway, A. L. Mohana Reddy, J. Yu and R. Vajtai, "Ultrathin Planar Graphene Supercapacitors", *Nano letters*, Vol. 11, No. 4, pp. 1423–1427, 2011.

200. Weng, Z., Y. Su, D.-W. Wang, F. Li, J. Du and H.-M. Cheng, "Graphene–Cellulose Paper Flexible Supercapacitors", *Advanced Energy Materials*, Vol. 1, No. 5, pp. 917–922, 2011.

201. El-Kady, M. and R. Kaner, "Scalable Fabrication of High-power Graphene Micro-supercapacitors for Flexible and On-chip Energy Storage. Nat. Commun. 4, 1475 (2013)", *Trans. Semicond. Manuf*, Vol. 24, No. 1, pp. 93–103, 2011.

202. Xu, Y., Z. Lin, X. Huang, Y. Liu, Y. Huang and X. Duan, "Flexible Solid-state Supercapacitors Based on Three-Dimensional Graphene Hydrogel Films", *ACS Nano*, Vol. 7, No. 5, pp. 4042–4049, 2013.

203. Gao, K., Z. Shao, X. Wu, X. Wang, J. Li, Y. Zhang, W. Wang and F. Wang, "Cellulose Nanofibers/Reduced Graphene Oxide Flexible Transparent Conductive Paper", *Carbohydrate polymers*, Vol. 97, No. 1, pp. 243–251, 2013.

204. Wang, Y., J. Chen, J. Cao, Y. Liu, Y. Zhou, J.-H. Ouyang and D. Jia, "Graphene/Carbon Black Hybrid Film for Flexible and High Rate Performance Supercapacitor", *Journal of Power Sources*, Vol. 271, pp. 269–277, 2014.

205. Ma, Y., C. Ma, J. Sheng, H. Zhang, R. Wang, Z. Xie and J. Shi, "Nitrogen-doped Hierarchical Porous Carbon with High Surface Area-derived from Graphene Oxide/Pitch Oxide Composite for Supercapacitors", *Journal of colloid and interface science*, Vol. 461, pp. 96–103, 2016.

206. Shao, Y., M. F. El-Kady, C.-W. Lin, G. Zhu, K. L. Marsh, J. Y. Hwang, Q. Zhang,

Y. Li, H. Wang and R. B. Kaner, "3D Freeze-casting of Cellular Graphene Films for Ultrahigh-power-density Supercapacitors", *Advanced Materials*, Vol. 28, No. 31, pp. 6719–6726, 2016.

207. Liu, Y., C. Zhao, S. Seyedin, J. Razal and J. Chen, "Flexible All-solid-state Supercapacitors and Micro-pattern Supercapacitors", *Flexible Energy Conversion and Storage Devices*, Vol. 1, pp. 1–36, 2018.

208. Barzegar, F., *Synthesis and Characterization of Activated Carbon Materials for Supercapacitor Applications*, Ph.D. Thesis, University of Pretoria, South Africa, 2015.

209. Liu, Y., X. Qiu, X. Liu, Y. Liu and L.-Z. Fan, "3D Porous Binary-heteroatom Doped Carbon Nanosheet/Electrochemically Exfoliated Graphene Hybrids for High Performance Flexible Solid-state Supercapacitors", *Journal of Materials Chemistry A*, Vol. 6, No. 18, pp. 8750–8756, 2018.

210. Singh, R. K., R. Kumar and D. P. Singh, "Graphene Oxide: Strategies for Synthesis, Reduction and Frontier Applications", *Rsc Advances*, Vol. 6, No. 69, pp. 64993–65011, 2016.

211. Xu, C. and D. Zhang, "Multifunctional Structural Supercapacitor Based on Cement/PVA-KOH Composite and Graphene", *Journal of Composite Materials*, Vol. 55, No. 10, pp. 1359–1369, 2021.

APPENDIX A: Additional Structural Characterizations

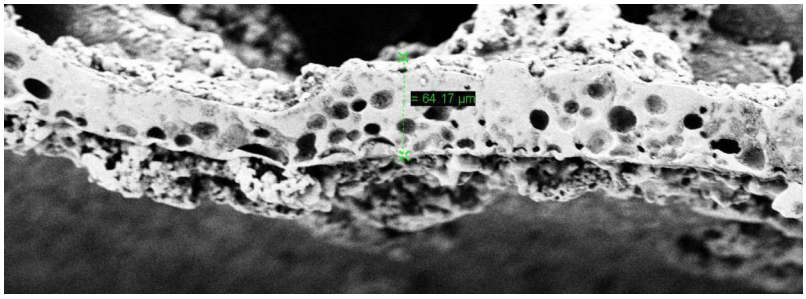

Figure A.1. Cross-section SEM image of PVA based gel film.

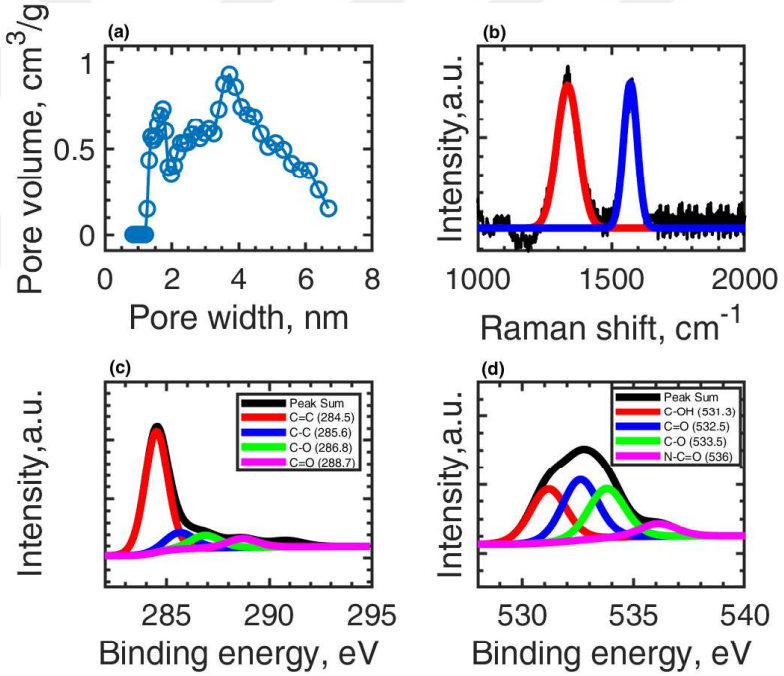

Figure A.2. Commercial AC structural characterizations a. Pore size distribution, b. Raman spectra, fitting curves. Red line represents the Lorentzian fit to the D-peak and Blue line represents the BWF fit to the G-peak, c. The XPS Deconvolution of C1s spectra and d. The XPS Deconvolution of O1s spectra.

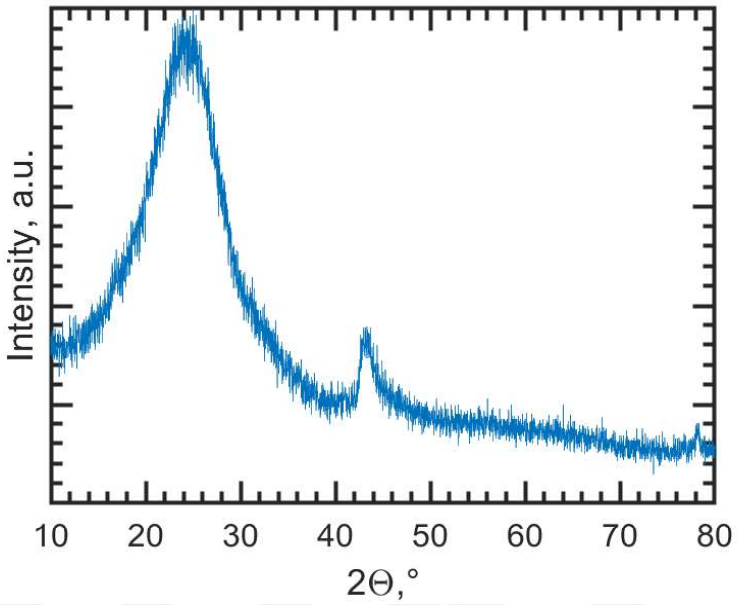

Figure A.3. XRD spectrum of RGO.

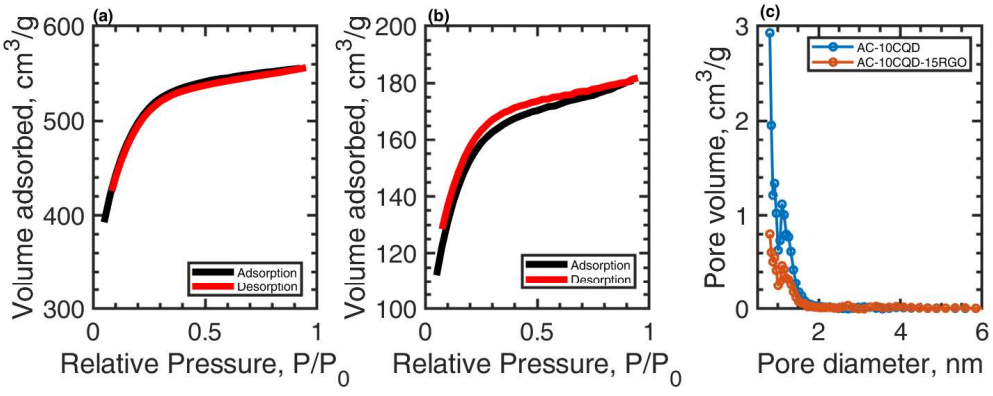

Figure A.4. Structural characterization of composite materials. N_2 adsorption/desorption isotherms of a. AC-10CQD, b. AC-10CQD-15RGO, and c. Pore size distribution of the materials.

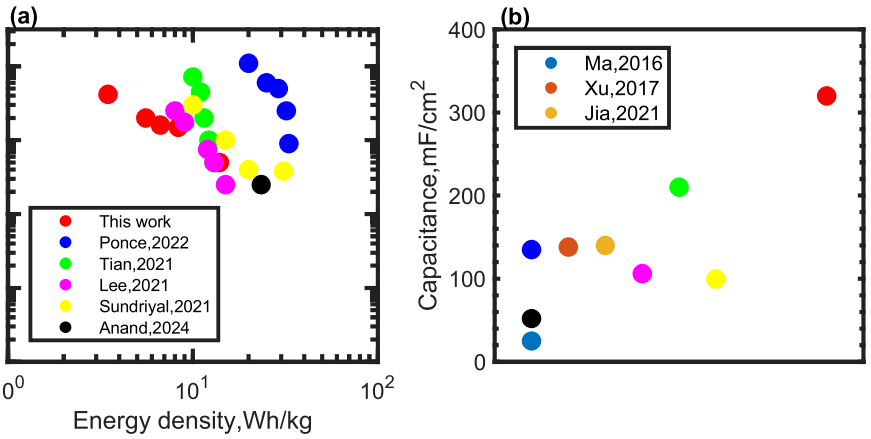

Figure A.5. Comparison with literature a. Ragone plots and b.Capacitance.

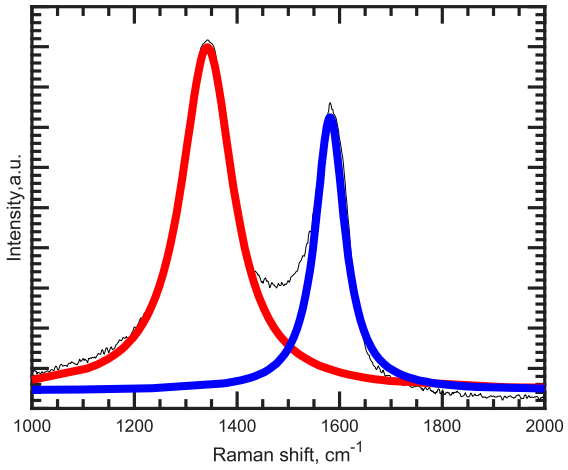

Figure A.6. Raman spectrum of BRGO.

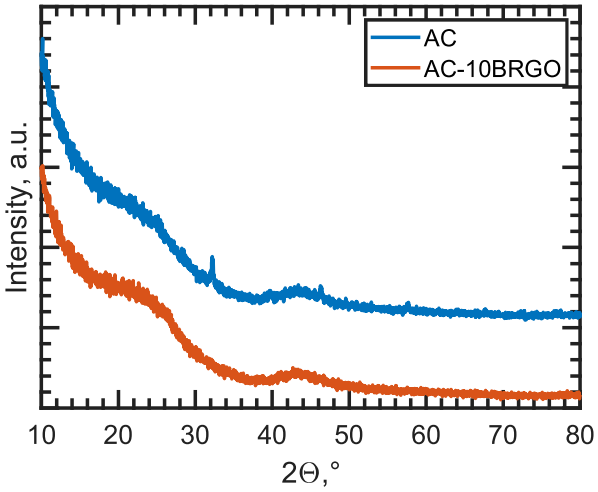

Figure A.7. XRD spectrum of AC and AC-10BRGO.

Table A.1. A comparison of carbon-based solid state supercapacitors.

Electrode	**Electrolyte**	**Cycle Life**	**Capacitance, mF/cm^2**	**Ref**
AC	PVA/KOH	87 % over 1000 cycles	140 (F/g) @ 5 mA/cm^2	[187]
AC	KI-PVA/KOH	96 % over 1000 cycles	250 (F/g) @ 0.8 A/g	[188]
AC cloth	PVA/H_2SO_4	95 % @ 1000 mV/s over 20000 cycles	25 @ 100 mV/s	[189]
AC from wallnut shell	PVA/KOH	96 % over 3000 cycles	138 @ 1 mA/cm^2	[190]
AC	HQ-PVA/KOH	84 % over 1000 cycles	326 (F/g) @ 0.8 A/g	[191]
N-doped AC	PVA/KOH	91.3 % @ 5 A/g over 1000 cycles	340 (F/g) @ 0.5 A/g	[192]
AC	PVA/KOH	93.3 % over 1000 cycles	140 (F/g) @ 0.5 A/g	[193]
AC from cotton stalk	PVA/KOH	98 % @ 0.2 A/g over 5000 cycles	210 (F/g) @ 0.5 A/g	[194]
AC	PVA/H_3PO_4	NA	106 (F/g) @ 0.5 mV/s	[195]
AC	IL-KI/PVA/EC	90 % over 3000 cycles	160 (F/g) @ 0.5 A/g	[196]
AC fiber	PVA/KOH	93 % @ 4 A/g over 3000 cycles	140 @ 0.5 A/g	[193]
AC from waste paper	PVA/H_2SO_4	95 % over 3000 cycles	99.5 @ 1 A/g	[197]
AC from olive tree pruning	PVA/KOH	80 % @ 2.3 A/g over 1000 cycles	135 @ 50 mV/s	[32]
AC doped with N,S	PVA/KOH	91 % @ 5 A/g over 10000 cycles	52 (F/g) @ 0.5 A/g	[198]
RGO	PVA/H_3PO_4	90 % over 1500 cycles	247 (F/g)	[199]
Graphene-cellulose paper	PVA/H_2SO_4	NA	46	[200]
Graphene	PVA/H_2SO_4	100 % over 10000 cycles	4.04	[201]
Functionalized graphene hydrogel	PVA/H_3PO_4	87 % over 10000 cycles	412 (F/g)	[202]
Graphene hydrogel	PVA/H_2SO_4	92 % @ 10 A/g over 10000 cycles	186 (F/g)	[202]
Graphene-cellulose nanofiber	PVA/H_2SO_4	99 % over 5000 cycles	203 (F/g)	[203]
Laser induced GO film	PVA/H_2SO_4	96 % over 10000 cycles	2.32 @ 16.8 mA/cm^3	[201]
RGO-carbon black	PVA/H_2SO_4	94 % over 3000 cycles	112 (F/g) @ 5mV/s	[204]
Graphene-activated carbon	PVA/H_2SO_4	90 % over 10000 cycles	43.8 (F/g)	[205]
Porous graphene	PVA/H_2SO_4	NA	34 @ 50 mV/s	[206]
RGO	PVA/H_3PO_4	86.2 % @ 5A/g over 10000 cycles	170 (F/g) @ 1 A/g	[207]
AC-RGO-CQD	PVA/KOH	90 % @ 100 mV/s over 1000 cycles	320 @ 50 mV/s	This work

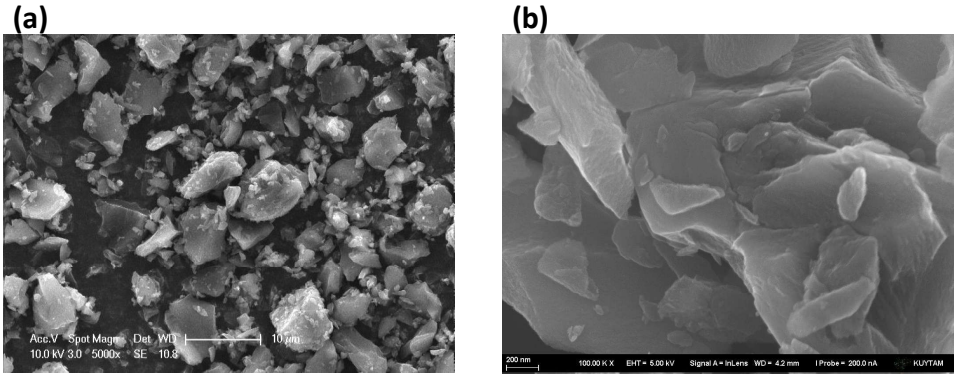

Figure A.8. SEM images of a. AC and b. AC-10BRGO.

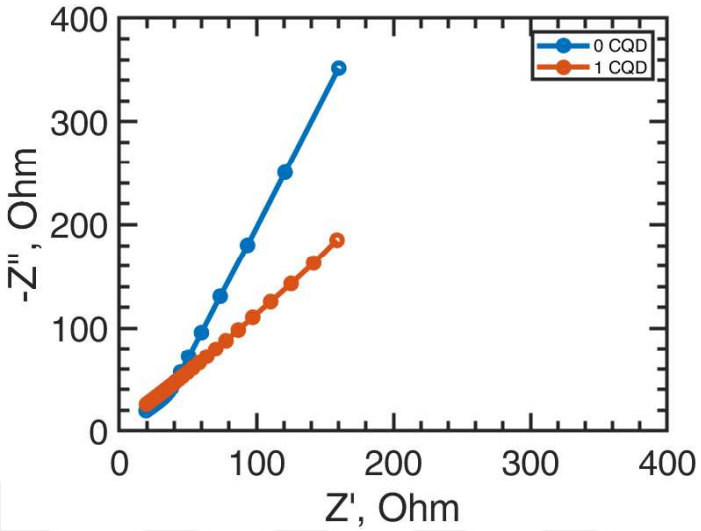

Figure A.9. Impedance spectroscopy of AC-10BRGO and AC-10BRGO/1CQD.

Table A.2. A comparison of solid state supercapacitors with PVA-based electrolytes.

Electrode	Electrolyte	Capacitance	Energy density, Wh/kg	Power density, W/kg	Cycling stability	Ref
AC	HQ-PVA/KOH	320 (F/g)	45	690	84.2 % over 1000 cycles	[136]
AC	KI-PVA/KOH	230 (F/g)	7.8	15000	96 % over 1000 cycles	[137]
AC	PVA/KOH	280 (F/g)	14.8	200	93 % over 3000 cycles	[138]
AC	PVA/KOH	190 (F/g)	4.8	10000	100 % over 1000 cycles	[208]
N,S doped CNS/Exfoliated graphene	PVA/KOH	200 (F/g)	6.3	2400	99 % over 10,000 cycles	[209]
N doped AC	PVA/KOH	270 (F/g)	7.9	250	90 % over 1000 cycles	[209]
AC	PVA/KOH	55 (F/g)	20	11000	80 % over 1000 cycles	[32]
Graphene	PVA/H2SO4	30 (μF/cm^2)	7	1200	NA	[210]
N doped AC	PVA/KOH	250 (F/g)	16	100	70 % over 5000 cycles	[143]
Graphene	Cement-PVA/KOH	10 (F/g)	1.5	2250	NA	[211]
AC-BRGO	CQD-PVA/KOH	107 (F/g)	29	875	90 % over 1000 cycles	This work